MULTI-LEVEL CONTINUOUS DATA ASSIMILATION AND UNCERTAINTY QUANTIFICATION OF RESERVOIR MODELS USING ENSEMBLE KALMAN FILTER AND TWO-STAGE MARKOV-CHAIN MONTE CARLO

A Dissertation

by

HISHAM HASSAN S. ALMOHAMMADI

Submitted to the Office of Graduate and Professional Studies of
Texas A&M University
in partial fulfillment of the requirements for the degree of

DOCTOR OF PHILOSOPHY

Chair of Committee,	Duane A. McVay
Committee Members,	Akhil Datta-Gupta
	Eduardo Gildin
	Jeffrey D. Hart
Head of Department,	Jeff Spath

December 2018

Major Subject: Petroleum Engineering

ABSTRACT

It is common practice to base decisions related to reservoir development and operations on reservoir models. Keeping these models updated and adequately quantifying subsurface uncertainty is critical for generating reliable forecasts, making optimal decisions and assessing risks. This dissertation presents an approach for continuous data assimilation and uncertainty quantification of reservoir models using a two-level update method: (1) data assimilation using Ensemble Kalman Filter (EnKF); and (2) two-stage Markov-Chain Monte Carlo (MCMC). In comparison with previous combined EnKF-MCMC work, in this approach the likelihood function is calculated exactly rather than approximately to ensure robust sampling of the posterior distribution. Additionally, a filtering stage is introduced at the MCMC level to reduce the computational cost while maintaining the necessary assumptions for accurate sampling. Further, reduced parameterization methods are utilized to improve covariance estimation and reduce computational overhead.

In the first level, an ensemble of model parameters and their associated dynamic variables is updated by frequently assimilating measured well data using EnKF. In the second level, at a lower frequency, MCMC is used to sample the posterior distribution of model parameters conditioned to all well measurements available from the beginning of the first assimilation cycle to the current time. The information obtained at the first level is utilized in two ways. First, the posterior covariance estimated from the EnKF update is used to propose new states (containing both parameters and dynamic variables) in the

MCMC chain. Second, the likelihood function is approximated at the first stage of MCMC using Peaceman equations and the proposed state. Only when a state is accepted at the first stage is reservoir simulation used to evaluate the likelihood function at the second stage of MCMC.

This approach was tested using two synthetic reservoir simulation experiments: a 1-D, single-phase heterogeneous case and a 2-D, two-phase channelized characterization case. The results demonstrate an improvement in posterior sampling (more samples with higher values of posterior density) over EnKF and standard MCMC random-walk perturbation methods. Additionally, efficiency of the sampling process is enhanced (smaller burn-in size and higher acceptance ratios) at a reduced computational cost. Finally, production forecast distributions generated using this approach show continuous improvement (narrow down and shift toward the true solutions) as more data are assimilated.

The approach outlined in the paper can be used by operators to quantify uncertainty in production forecasts. Additionally, the multi-level approach provides operational advantage in that short-term and long-term operational decisions can be made based on high-frequency assimilation cycles and lower-frequency updates, respectively.

DEDICATION

To my parents for their limitless love and endless support.

To my beloved wife, Nada, whose love and confidence is a constant source of inspiration and encouragement.

ACKNOWLEDGEMENTS

First and foremost, I am grateful to The Almighty God for establishing me to complete this dissertation.

I would like to express my sincere gratitude to my committee chair, Dr. Duane McVay, for his continuous guidance and support throughout my time here at Texas A&M University.

I would also like to thank my committee members, Dr. Akhil Datta-Gupta, Dr. Eduardo Gildin, and Dr. Jeffrey D. Hart, for providing valuable insight and help during the course of this research.

I also wish to thank Saudi Aramco for providing a scholarship and for allowing me to work on the problem described in this dissertation.

Thanks are also due to my colleagues and the faculty and staff at the Petroleum Engineering department for making my experience at Texas A&M University worthwhile.

Finally, I owe my deepest gratitude to my family and friends who have always stood by me.

CONTRIBUTERS AND FUNDING SOURCES

Contributors

This work was supervised by a dissertation committee consisting of Dr. Duane McVay of the Department of Petroleum Engineering, Dr. Akhil Datta-Gupta of the Department of Petroleum Engineering, Dr. Eduardo Gildin of the Department of Petroleum Engineering, and Dr. Jeffrey Hart of the Department of Statistics.

All work for the dissertation was completed independently by the student.

Funding Sources

There are no outside funding contributions to acknowledge related to the research and compilation of this dissertation.

TABLE OF CONTENTS

Page

LIST OF TABLES

Page

LIST OF FIGURES

1. INTRODUCTION*

In the petroleum industry, reservoir management is the discipline concerned with maximizing the value of a petroleum asset. The main function of reservoir management is to make a set of decisions that define an operation plan—such as drive mechanism, size and configuration of surface facilities, well placement, and choke settings—that aims to maximize a hierarchy of stated objectives—such as production schedule, rate plateaus, hydrocarbon recovery, and net present value (NPV) (Gringarten 1998; Almohammadi 2013). Reservoir engineers implement this operational strategy, run surveillance programs to monitor the performance of the field, and make necessary adjustments to the operational plan. The quality of reservoir management is often determined by how well these objectives are met. Often, reservoir simulation is used to investigate a set of possible alternatives for an operational plan and select the most optimal plan.

Nonetheless, model-based optimization of reservoir models is not trivial. It usually involves large-scale models, complex physical processes and a coupled model optimization and parameter estimation problem (i.e., inverse modeling). The optimization part of the problem involves a multitude of decision variables with many alternatives, such

* Part of this section (portions of pages 4-7) is reprinted from my master's thesis (Almohammadi, H.H.S. 2013. Continuous Model Updating and Forecasting for a Naturally Fractured Reservoir, Texas A&M University). Copyright [2013] by Hisham Hassan S. Almohammadi.

as choice of drive mechanism; number, location, orientation and configuration of infill wells; well choke settings; and surface facility configuration and settings. The optimization problem is also complicated by multiple objectives, such as meeting short-term production schedules, reducing water-cut, maintaining reservoir pressure, maximizing overall field recovery, and maximizing NPV. Furthermore, optimizations are performed over varying time-scales.

The parameter estimation problem involves parameterization of reservoir characterization and searching a huge, multi-dimensional parameter space for a set of reservoir models that reproduce the historical performance of the field, within an acceptable margin of error, constrained by some preconceptions of geological and reservoir engineering parameters.

Historically, the industry has implemented simplistic models to describe uncertainty in forecasting and optimizing reservoir performance, often ignoring uncertainty altogether. In most cases, the estimation problem is handled by manual tuning of reservoir parameters to approximately reproduce observed reservoir measurements. These efforts are often subjective, based on expert judgment of the reservoir engineer, and largely ignore uncertainty quantification. Then, “history-matched” models are used to select an optimal plan by investigating a limited number of alternatives put forth based on some preconceived engineering intuition. Again, limited attention is given to quantifying the impact of uncertainty on forecasted reservoir performance. This plan is then updated periodically or reactively in the same manner.

It has been demonstrated that ignoring or underestimating uncertainty can result in suboptimal decisions and huge disappointments (Brashear et al. 2001; McVay and Dossary 2012). Additionally, a significant body of research demonstrates that closed-loop reservoir-management (CLRM) is a better strategy than reactive or periodic reservoir management (Brouwer et al. 2004; Chen et al. 2011; Foss and Jensen 2011; Jansen et al. 2008; Jansen et al. 2009; Saputelli et al. 2005; Sarma et al. 2005; Wang et al. 2009). CLRM is a strategy in which reservoir models and uncertainties are continuously and systematically conditioned to newly measured data. Then, optimal configurations are selected using the recently updated models. Specifically, research verifies that implementing CLRM strategy yields better reservoir characterization estimates and higher objective-function values.

This research focuses on the continuous-model-updating and uncertainty-quantification parts of the CLRM process. Optimization of reservoir performance will not be addressed in this work. A major requirement for any practical implementation of CLRM in real applications is algorithms that are capable of delivering updated models that accurately characterize reservoir description uncertainties in a timely manner, consistent with the operational and decision cycles. The efficiency and accuracy of such algorithms are challenged by the size, complexity, and uncertainties associated with the description of reservoir models. The need for such algorithms is of vital importance to the development of CLRM. Continuous-model-updating and uncertainty quantification continue to be subjects of rapidly growing research.

1.1 Background and Motivation

This section provides a brief background of the evolution of reservoir management in the petroleum industry, and the emergence of the closed-loop paradigm. It also discusses the value of assessing uncertainty to the decision-making process in the petroleum industry. Finally, the motivation behind this research is highlighted.

1.1.1 Reservoir Management

Reservoir management is a process that involves the utilization of data, mathematical modeling, and expertise, in order to determine a set of decisions and operational controls that optimize reservoir profitability or some other stated objective. The process also includes the execution of the production plan and the monitoring of reservoir response (Gringarten 1998; Saputelli et al. 2005).

Historically, reservoir management has been associated with reservoir and production engineering. The need for integration between geoscience and engineering disciplines for improved reservoir management was recognized as early as the 1970s. In 1977, Halbouty stated "It is the duty and responsibility of industry managers to encourage full coordination of geologists, geophysicists, and petroleum engineers to advance petroleum exploration, development, and production" (Halbouty 1977). The concept of asset teams was introduced in the 1980s. Asset teams did not start to show success until the 1990s, when advancements in software and computing power allowed for some level of integration between team members. In the late 1990s formalized processes were developed to standardize asset teams' workflow and assure quality (Elrafie et al. 2007).

Recent technology advances have allowed for real-time remote monitoring and control of well and field production. Such capabilities enable continuous and automatic fine-tuning of production controls to optimize project economics and stated well or reservoir performance objectives. Remotely activated sub-surface valves on “smart wells” are becoming fairly common technology in the oil industry, as they are used to optimize the production and injection of fluids from different pay zones and remotely monitor multiphase flow meters and pressure gauges.

Smart field technology, with all its capabilities, gives rise to a new concept of reservoir management. CLRM or Real Time Asset Management (RTAM) is a reservoir management process that utilizes real-time monitoring capabilities, model updating algorithms, and model-based optimization algorithms in a closed loop, to continuously and systematically control production in order to optimize stated objectives such as NPV or hydrocarbon recovery. This breakthrough technology promises substantial benefits to the oil industry, such as higher amount of hydrocarbon recoveries, improved project life-cycle value, and better utilization of human resources. Although this approach is not practically feasible yet, it is receiving rapidly growing attention from both industry and academia.

1.1.2 Value of Assessing Uncertainty

Capen (1976) demonstrated more than thirty years ago that people tend to significantly underestimate uncertainty. He suggested that a better understanding of uncertainty would have a significant beneficial effect on risk assessment and profits. In their analysis of financial performance of the oil and gas industry, Brashear et al. (2001)

noted that during the 1980s and the 1990s the return on net assets by the largest U.S.-based companies in the exploration and production sector was seven percent on average for projects that were selected with a hurdle rate of 15 percent and financed with capital that costs 9 to 12 percent on average. They attributed this underperformance of the oil and gas industry, at least partially, to the use of deterministic methods to estimate project value. "When compared to the 'full' recognition of uncertainties, dependencies, and risk, ranking by deterministic estimates of project value—by far today's widely used approach—was found to overstate expected value by a factor greater than two, to ignore critical risks, and to select a portfolio of projects with a lower return and higher, uncompensated risk than were possible if full uncertainty had been recognized," the authors state.

Dossary and McVay (2012) performed a quantitative study to measure the value of assessing uncertainty. In this work, the authors performed portfolio optimization simulations, where estimates of NPV were calculated with inherent overconfidence (underestimation of uncertainty) and directional bias (optimism or pessimism). Next, they calculated expected disappointment, which is the difference between the value a company estimates and the actual realized value (where decisions are made based on biased estimates, but actual values are based on the true distribution assuming no overconfidence or bias). The results of their simulations show that expected disappointment ranges from about 30 percent for moderate amounts of overconfidence and bias to 100 percent for high degrees of bias and overconfidence.

Both references cited above hint to the fact that optimal decision-making in the oil and gas industry is not realized by the transition from conventional deterministic

approaches to simplified approximation of uncertainty, but rather by full assessment of uncertainty. Brashear et al. (2001) stated that such "short cut" approximations of uncertainty can result in significant overestimation of expected values and underestimation of risk, even with the simplest possible projects. It is clear that the task of performing full assessment of uncertainty in the oil and gas industry is not trivial. Even for a simple project, the number of uncertainties is substantial, ranging from subsurface uncertainties of reservoir description to uncertainties related to project execution (e.g., cost of material, delays, change of regulations), and even uncertainties related to the global market of energy as they impact demand, supply, and pricing. Clearly, quantifying uncertainty is a challenging problem that involves a wide range of disciplines, such as geology, geophysics, petroleum engineering, project management, statistics, and economics. This thesis will attempt to address only the impact of subsurface reservoir-description uncertainty on forecasted reservoir performance.

1.1.3 Motivation

This research is motivated by ideas from optimal control theory and estimation theory, in particular, their applications in CLRM. A significant amount of research demonstrates the advantage of closed-loop strategy of reservoir management in increasing hydrocarbon recoveries and maximizing NPVs, when compared to reactive or periodic strategies (Brouwer et al. 2004; Sarma et al., 2005; Chen et al., 2009; Jansen et al., 2009; Wang et al., 2009; Foss and Jensen, 2011).

It has also been highlighted that underestimating uncertainty in the decision-making process can lead to great disappointments and underperformance.

In addition, it can be argued that a continuous approach to model updating can lead to better estimates of reservoir parameters as time progresses. When compared to a one-time study approach, more time and computer power can be allocated to exploration of the parameter space. Moreover, in an environment where continuous production forecasts are provided, measures of bias and overestimation can be generated. Consequently, a mechanism to calibrate uncertainties could be developed to provide better estimates of future production forecasts (McVay et al. 2005).

This research focuses on the model updating and uncertainty quantification element of the CLRM process. Despite the great improvements it is hypothesized to deliver to reservoir management, research in CLRM is still in its infancy. Continuous model updating algorithms that are efficient enough to meet operational requirements, yet still provide reliable estimates and uncertainty characterization of reservoir parameters and forecasted output, remains to be a major area of research.

1.2 Status of the Problem

The first application of continuous model updating in reservoir engineering, to the best of my knowledge, was the work of Naevdal et al. (2002), in which an Ensemble Kalman Filter (EnKF) was used to update an ensemble of near-well models representing geological uncertainty through continuous data assimilation. Since then, EnKFs have been used rapidly in synthesized data assimilation experiments to improve some model parameter estimates, mainly permeability, and predict reservoir performance. The results of this work show continuously improving parameter-estimate and forecast quality, as

validated by a case of already known geology, i.e., “truth case” (Brouwer et al. 2004; Jansen et al. 2008; Jansen et al. 2009; Lorentzen et al. 2009; Naevdal et al. 2005; Wang et al. 2009).

The attractiveness of EnKF as a data assimilation tool arises from its simplicity of implementation, low computational cost, and data-management efficiency. However, there are many reservations about its application in reservoir model updating. Aanonsen et al. (2009) provided a comprehensive review of the literature on EnKF in which authors discuss several issues that might hinder the accuracy of its application in reservoir engineering, such as dependency on initial ensemble, deficiency in approximating the covariance matrix, weakness in handling non-Gaussian prior distributions, and strongly non-linear physical processes. Emerick and Reynolds (2011) summarized the requirements for EnKF to represent a correct posterior distribution as the following: (1) Gaussian prior model for the state vectors, (2) linear relation between predicted data and the state vector, (3) Gaussian measurement errors that are uncorrelated in time, (4) dynamic systems that represent a first-order Markov process, and (5) ensemble sizes that approach infinity. Clearly, these requirements either do not apply or are not feasible in the case of modeling fluid flow in porous media. Several suggestions to handle such limitations in EnKF are proposed in the literature. Examples are the use of parameterization (Chen et al. 2009; Gu and Oliver 2005; Jafarpour and McLaughlin 2009b; Metropolis et al. 1953) to handle non-Gaussian states, iterative EnKF (Gu and Oliver 2007; Li and Reynolds 2007; Lorentzen and Naevdal 2011; Metropolis et al. 1953; Reynolds et al. 2006) to handle non-linearity, the use of square-root filters to reduce

sampling errors (Evensen 2009), and covariance localization to reduce spurious correlations (Emerick and Reynolds 2011). The use of EnKF for reservoir model updating is still a subject of ongoing research.

A different approach to the problem is continuously (i.e., using the entire life-time of the field rather than a one-time study) solving the inverse problem using either stochastic optimization or Bayesian inversion methods. In both stochastic optimization and Bayesian inversion methods, all the available measurements are used to solve the inverse problem. The difference between the two methods (stochastic and Bayesian) is that, in the stochastic method, quantification of uncertainty is based on statistical analysis of a number of models with equal or similar objective function values, while in the Bayesian method quantification of uncertainty arises naturally because the solution to the inverse problem is a probability density function. One example of the application of stochastic methods in continuous model updating is the work of Holmes et al. (2007) in which Genetic Algorithms (GA) were used to continuously generate history-matched models over time, incorporating new well and production data as they become available. These models are then used to generate an evolving distribution of forecasted output—for example, cumulative oil production. The authors tested their approach on a live field by providing real-time probabilistic forecasts of production. Sarma et al. (2005) proposed a procedure in which two sub-processes are used every time data are assimilated: (1) model updating by means of gradient-based techniques, and (2) model approximation and uncertainty propagation. The authors argue that using approximate models generates reasonable results with substantial increase of process efficiency. It is not clear, though, if

decoupling model updating and uncertainty propagation would result in a reliable and representative quantification of uncertainty, especially when local optimization techniques are used for model updating. Additionally, it is not shown if using an approximate model for reservoir performance would continue to provide adequate results when larger and more complex models are used. An example of continuous MCMC inversion method is the work of Liu and McVay (2010). Results of this study show improvement in parameter estimation as more data are assimilated and a distribution of forecasted output that continuously narrows over time and with means approaching the "truth case."

Although more computationally intensive than EnKF, MCMC inversion methods produce correct sampling of the posterior as the limit of iterations approaches infinity. Additionally, because reservoir simulation models are used to calculate updated model states (compared to estimating updated model states using the EnKF update equation), and because reservoir description does not change recursively within one sampled realization, as in the case of EnKF, MCMC methods produce results that are physically consistent. It can be argued that when implemented in continuous operation, in contrast to one-time-study settings, the computational cost associated with such methods becomes less significant as the run requirement is spread over a long period of time.

MCMC, with the Metropolis-Hasting (M-H) algorithm, in particular, has been applied in reservoir engineering to condition reservoir description to production data. In its standard application, a Markov chain is generated by iteratively sampling new states from a "proposal distribution" and evaluating them using reservoir simulation. The M-H algorithm is then used to determine whether the new state should be accepted in the chain.

It can be shown theoretically that a stationary MCMC chain generates valid samples from the posterior distribution (i.e., distribution of reservoir parameters conditioned to dynamic data). The attractiveness of MCMC M-H arises from the fact that it does not require knowledge of the normalization constant of the posterior distribution. The main disadvantage is that it is highly computationally expensive, because it requires running the forward model (i.e., reservoir simulation) each time a new state is evaluated. Generally, the research concerning the use of MCMC in relation to the reservoir modeling inverse problem can be categorized in two groups: (1) methods that aim to improve proposal selection and, consequently, increase the acceptance rate—hence improve efficiency, and (2) methods that aim to approximate or reduce the cost of running the forward model. One approach to improve proposal selection is to use algorithms that use previously accepted states to "tune" the proposal distribution, such as Adaptive Proposal (AP), Adaptive Metropolis (AM), and Adaptive Genetic MCMC (Floris et al. 2001; Haario et al. 1999, 2001; Holden 1998). Another approach is the use of gradients or sensitivities in proposal selection (Ma et al. 2008; Oliver et al. 1997). The second group of methods usually involve an intermediate step where the full reservoir simulation is replaced by an up-scaled representation (i.e., flow up-scaling or spatial up-scaling) or approximated using gradient or sensitivity calculation (Efendiev et al. 2005; Ma et al. 2008).

Emerick and Reynolds (2011) suggested a combined EnKF-MCMC approach that aims to take advantage of the computational efficiency of the EnKF and robustness of MCMC. In this work, EnKF is performed first. Next, the final updated ensemble is re-run using the reservoir simulator from the initial time-step until the end time of the

assimilation experiment. Then, model parameters and time-dependent model states (i.e., grid-cell pressures and saturations) for all ensemble members are collected in one augmented matrix. Finally, several MCMC chains are generated using a proposal selection based on the augmented matrix (using a square-root filter). Since sampling the proposal density, in this case, produces realizations that contain both model parameters and model states, the measured well response can be directly calculated using Peaceman equations (Peaceman 1978). Hence, the likelihood function can be approximated without the need to run the simulation. Additionally, the authors retain only the last sample in each MCMC chain to reduce convergence issues and dependency on initial guess.

Although this combined EnKF-MCMC process significantly reduces computational requirements, when compared to those of the standard MCMC, it is not clear if the method used to approximate the likelihood results in valid sampling of the posterior. Using this approximation implicitly assumes that the relationship between model parameters and time-dependent model states is approximately linear and can be described by a joint Gaussian distribution. This is a strong assumption to maintain when dealing with reservoir simulation models.

Most of the research using Bayesian inversion methods in reservoir simulation ignores the continuous nature of data assimilation in petroleum reservoirs. As more measured data becomes available, the definition of the posterior density function changes with time. This makes statistical inference and uncertainty quantification more challenging because resulting samples are associated with different posteriors. Additionally, to be implemented as a part of CLRM strategy, a proposed method needs to

be compatible with the operational cycle in the field (i.e., should be capable of generating updated models and uncertainty quantification at a frequency that is suitable for decision-making).

In summary, the success of any continuous-model updating part of CLRM strategy depends on its ability to provide reasonably accurate parameter estimation and characterization of uncertainty, as well as adapt to the nature of decision-cycle frequency. While a combined EnKF-MCMC approach seems to be a promising starting point to pursue such a strategy, there is a need to extend previous work to ensure valid posterior sampling. Additionally, more effort should be exerted to make the process more computationally efficient and accommodating of operational needs.

1.3 Research Objectives

The objective of this research is to develop and test a multi-level continuous-model-updating and uncertainty quantification procedure using EnKF and MCMC that satisfies the following requirements:

- Takes advantage of the efficiency of EnKF without compromising the accuracy of MCMC sampling at the second level.
- Is flexible enough to be easily integrated in CLRM strategy.
- Provides reliable model updates and forecasts in a timely manner that is consistent with operation needs and decision-making processes.

1.4 Remainder of the Dissertation

This remainder of this dissertation is divided into six sections. These sections are organized as follows. Section 2 summarizes and discusses existing approaches to solving the inverse problem in reservoir simulation. It also provides the theoretical and mathematical background for the methods used in this research. Section 3 explains the methodology of this research and presents the new procedure developed for multi-level EnKF and two-stage MCMC continuous model updating and uncertainty quantification. In Section 4, multi-level EnKF and one-stage MCMC sampling is tested on a small 1-D, single-phase problem to assess the proposal distribution based on the EnKF posterior covariance and its impact on MCMC posterior sampling. In Section 5, the multi-level EnKF and two-stage MCMC continuous model updating algorithm is tested on a 2-D, two-phase channelized reservoir. The resulting estimates of model parameters and production forecasts are presented and analyzed. Section 6 discusses the results of this research. Section 7 summarizes the conclusions of this work and provides recommendations for future work.

2. SOLUTION TO THE INVERSE PROBLEM

In most cases, many parameters used in reservoir modeling are not known exactly. Examples of such parameters include initial reservoir properties such as fluid contacts, pressures, and saturations; geological description parameters such as porosity and permeability; or properties of reservoir fluids. Some prior knowledge of such parameters might exist from geological conceptualization and the analysis of static data (e.g., core, logs, and seismic). Dynamic data, such as measured well pressures and flow rates, are often integrated with reservoir models to improve the estimates of these parameters. In doing so, reservoir models are calibrated to approximately reproduce the actual observed measurements. This provides some level of confidence in forecasts generated with such models. This process is often called history matching or the inverse problem in reservoir simulation.

Because the number of parameters that must be estimated in the inverse problem is often much larger than the available measured date, the problem is characterized as being ill-posed or underdetermined (Backus and Gilbert 1967; Oliver et al. 2008). Consequently, the inverse problem could have more than one mathematical solution. Additionally, because the relationship between model parameters and observed measurements is nonlinear, the problem requires an iterative solution.

This chapter summarizes and discusses the major approaches to solving the inverse problem in the petroleum literature. More attention is dedicated to explaining Ensemble

Kalman Filter (EnKF) and Markov-Chain Monte Carlo (MCMC) as they are major components in this research.

The first two sections address gradient-based and global search methods. Then, the Bayesian approach to the inverse problem is introduced. MCMC methods are then presented and explained. Next, a brief description and summary of recursive methods and EnKF is given. Finally, parameterization methods are introduced and summarized.

2.1 Gradient-Based Minimization Methods

In this group of methods, parameter estimation is obtained by iteratively searching for a vector of model parameters θ that minimizes an objective function $O(\theta)$. The objective function usually involves a least-squares term, and it could also include some other regularization terms or prior terms **(Eq. 1)**.

$$O(\theta) = (g(\theta) - d_{\text{obs}})^T C_D^{-1} (g(\theta) - d_{\text{obs}}) \quad (1)$$

Here, $g(\theta)$ is the response of the model at a certain value of the parameter θ, d_{obs} is a vector of noisy observed measurements, and C_D is the covariance of the measurement errors.

Many minimization algorithms are used in the literature, such as Gauss-Newton, Levenberg-Marquardt, Broyden-Fletcher-Goldfarb-Shanno (BFGS), and low-memory BFGS (LBFGS). Although they differ in details, the algorithms usually solve the minimization problem by evaluating the gradient of the objective function **(Eq. 2)**.

$$\nabla O(\theta) = 2\, C_D^{-1}\, (g(\theta) - d_{\text{obs}}) \nabla g(\theta) \quad (2)$$

At each iteration, a new parameter value is suggested by solving a linear equation that usually involves evaluating the gradient and the Hessian matrix, $H(\cdot)$, evaluated at the previous iteration following some form of Newton's method **(Eqs. 3 and 4)**.

$$H\left(\theta^{\ell}\right)\delta\theta^{\ell+1} = -\nabla O(\theta^{\ell}) \tag{3}$$

$$\theta^{\ell+1} = \theta^{\ell} + \delta\theta^{\ell+1} \tag{4}$$

After a number of iterations, the solution might converge to a minimum. Evaluating the gradient usually requires the calculation of the sensitivity coefficients, $\nabla g(\theta)$, at each iteration, which could be quite expensive. Often adjoint methods are used to calculate the sensitivity coefficients, which are less computationally demanding than the standard perturbation method.

One main concern with gradient-based methods is that they might not converge to global minima. Additionally, because the goal is, generally, finding a single solution, uncertainty quantification is limited to the characterization of uncertainty around this one solution.

2.2 Global Search Methods

The goal of global search methods is to find global minima. In general, these methods are stochastic in nature, and include a variety of approaches. Some global search methods do not require the calculation of gradients. Those that do require the calculation of gradients are combined with elements of randomness. Some global search methods are population or ensemble based and utilize concepts from genetics or social behavior such as mutations and evolution to find solutions (e.g., Genetic Algorithms (GA) and Particle

Swarm Optimization (PSO)). In general, global search methods include two features: (1) exploration, in which the parameter space is searched in order to find promising regions of the objective function; (2) exploitation, in which the search is refined in an area of potential solution. Because these methods search for solutions by attempting to explore the entire parameter space, they usually come with high computational cost. When such methods are used, statistical inference and uncertainty quantification is often based on a set of a limited number of solutions with equal or similar objective function values.

2.3 Bayesian Formulation to the Inverse Problem

In the Bayesian approach to the inverse problem, the parameter being estimated is treated as a random variable. The formulation starts with assigning a probability density function, $\pi(\theta)$, which represents the prior knowledge of the parameter θ. Then, when a data set y that relates to the parameter θ by a function $f_\theta(y)$ is observed, a posterior distribution can be calculated by Bayes' rule **(Eq. 5)**. This distribution combines prior knowledge and knowledge derived from data and theory. The likelihood function $f_\theta(y)$ evaluates the likelihood of observing the data set y for a given value of the parameter θ, i.e., $p(y|\theta)$.

$$\pi(\theta|y) = \frac{f(y,\theta)}{m(y)} = \frac{f_\theta(y)\pi(\theta)}{\int_\Omega f_\theta(y)\pi(\theta)d\theta} \quad (5)$$

Sampling directly from the posterior distribution requires the calculation of the marginal distribution of the data in the denominator of **Eq. 5**. Usually, this integral cannot be calculated analytically, especially for high-dimensional, non-linear problems. When

the distribution cannot be sampled directly and cannot be easily approximated, indirect iterative methods such as MCMC are used.

2.4 Markov-Chain Monte Carlo

In this class of methods, the aim is to generate a Markov chain with a specific target density (i.e., posterior density). As the name implies, properties of Markov theory are combined with Monte Carlo simulations; any statistical measure of interest to a random variable θ can be obtained by randomly sampling the corresponding density function. Combining these two elements makes it possible to sample the posterior distribution through an iterative process, even when the samples are not independent (i.e., exhibit some level of auto-correlation). In the following subsections, Markov chain theory in the context of Bayesian statistics is introduced. Then, M-H and randomized maximum likelihood (RML) samplers are introduced and discussed.

2.4.1 Markov Chain

A Markov chain is a sequence of random variables generated by a Markov process. A Markov process is a process where the conditional probability of the current state of the system, X_{n+1}, depends only on the previous state of the system, X_n, rather than the entire history of the system, $(X_0, \dots, X_n)$, as in **Eq. 6**.

$$P\left(X_{n+1} = s_j \middle| X_0 = s_k, \dots, X_n = s_i\right) = P\left(X_{n+1} = s_j \middle| X_n = s_i\right) \tag{6}$$

Each Markov chain is defined by its transition probability function:

$$P(i,j) = P(i \to j) = P(X_{n+1} = s_j \,|\, X_n = s_i) \tag{7}$$

The transition probability function defines the probability of transitioning from a given state i to another state j at a single step. The chain produced by such a Markov process is said to be invariant (stationary) for the transition kernel P if

$$P(Y) = \int P(X,Y)P(X)dX. \tag{8}$$

Under mild regularity conditions, namely irreducibility and aperiodicity, the chain converges to an invariant distribution. Consequently, it must be possible to move from any state to any other state in the domain of the target distribution (i.e., irreducibility). Additionally, the chain does not move deterministically with a fixed length between certain states (i.e., aperiodicity). A Markov chain can be shown to be invariant if it satisfies the detailed-balance or reversibility condition,

$$P(X,Y)P(X) = P(Y,X)P(Y). \tag{9}$$

The samples generated by a Markov chain are, by definition, not independent, but rather have some measure of auto-correlation. However, the pointwise ergodic theorem (also called the law of large numbers for Markov chains) states that for a sufficient number of samples, the statistics obtained from the chain represents the statistics of the target distribution (Jackman 2009b).

2.4.2 Metropolis-Hasting

The Metropolis-Hasting algorithm samples a Markov chain. It was originally proposed by Metropolis et al. (1953), and extended by Hastings (1970). Chib and Greenberg (1995) provide a detailed review of the algorithm, including the complete mathematical background. The algorithm can be summarized by the following steps:

1. Initialize by drawing a random sample θ_0.

2. Sample a proposed state θ^* using a specified proposal or jumping distribution, $q_t(\theta_{t-1}, \theta^*)$.
3. Calculate the acceptance ratio α,

$$\alpha(\theta_{t-1}, \theta^*) = \min\left(1, \frac{\pi(\theta^*)}{\pi(\theta_{t-1})} \frac{q_t(\theta^*, \theta_{t-1})}{q_t(\theta_{t-1}, \theta^*)}\right). \quad (10)$$

4. The proposed state is then accepted with probability equal to α and rejected with a probability equal to $1 - \alpha$
    - If the proposed state is accepted (i.e., $\alpha > U \sim \text{Unif}(0,1)$), then $\theta_t = \theta^*$.
    - Otherwise, $\theta_t = \theta_{t-1}$.
5. Repeat steps 2 to 4 until a sufficient number of samples is obtained.

The $\pi(\cdot)$ in **Eq. 10** is the posterior density function evaluated at either the current state or the proposed state. Because only the ratio of the posterior densities is calculated, it is not necessary to explicitly calculate the marginal distribution of the data—the integral in the denominator of Eq. 5, as it cancels out. According to the acceptance ratio (Eq. 10), the acceptance of a proposed state relies heavily on the ratio of its density to the current state in the chain. Consider the original case developed by Metropolis et al. (1953), in which the proposal distribution is symmetric (i.e., probabilities of jumping forward—from the current state to the proposed state, and jumping backward—from the proposed state to the current state, are equal, and the ratio of proposals is simply unity). If the proposed state increases the density of the posterior, then the ratio is larger than one, and the proposal is accepted. If the proposed state decreases the density of the posterior, then the ratio is less than one and the proposal is accepted with a probability equal to the acceptance ratio. In

other words, proposals having posterior densities larger than that of the current state are accepted. Proposals having posterior densities smaller than that of the current state are accepted with probabilities proportional to the reduction of the posterior density relative to the current state.

The transition probability (i.e., transition kernel) for the Markov chain generated by the Metropolis-Hasting algorithm is (Chib and Greenberg 1995):

$$P(\theta_{t-1}, \theta_t) = \ q_t(\theta_{t-1}, \theta^*) \ \alpha(\theta_{t-1}, \theta^*) + r(\theta_{t-1})\delta_{\theta_{t-1}} \tag{11}$$

where $r(\theta_{t-1})$ is the marginal distribution at θ_{t-1}:

$$r(\theta_{t-1}) = 1 - \int q_t(\theta_{t-1}, \theta^*)\, \alpha(\theta_{t-1}, \theta^*)\, d\theta \tag{12}$$

It is worth noting that the transition probability depends only on the current state of the chain and not the entire history. A proof that the Metropolis-Hasting transition probability **(Eq. 11)** satisfies the detailed balance or reversibility condition is provided in Appendix A.1.

Having established the theoretical foundation of the Metropolis-Hasting algorithm, several issues related to the application of the algorithm are discussed in the following subsections—in particular, proposal density selection, chain mixing, convergence diagnostics, and improved forms of MCMC in reservoir simulation.

2.4.2.1 Proposal Density Selection

The M-H proposal density function can have many forms. Two important groups of proposal densities are random-walk perturbation and independent proposals. In the random-walk methods, the proposal is calculated by randomly perturbing the current state. Usually, a random perturbation variable is drawn from a Gaussian or uniform distribution

with a zero mean and added to the current state. In the independent methods, the proposal calculation does not depend on the current state. Ma et al. (2008) used a Langevin proposal calculated by adding a term that contains the gradient of the posterior evaluated at the current state, and a random perturbation term drawn from a Gaussian distribution. The covariance of the proposal density is an important parameter that affects convergence and chain mixing. A convenient form used for random-walk methods is the negative of the inverse of the Hessian matrix evaluated at the current state (i.e., maximum likelihood estimate (MLE), see (Jackman 2009a)). This is, however, extremely computationally intensive for most engineering problems.

2.4.2.2 Chain Mixing

Theoretically, a Markov chain sampled using the M-H algorithm converges to a unique and invariant (stationary) distribution, the target distribution, regardless of the choice of the proposal distribution. In practice, the choice of the proposal distribution is very influential on the performance of the chain, as it controls how long it takes for the chain to reach a stationary distribution (i.e., "burn-in" period), how well the chain covers the regions of the target distribution (i.e., chain mixing) and the acceptance rate (i.e., the rate at which proposed samples are accepted) (Chib and Greenberg 1995).

The variance or the spread of the proposal is a key element that affects the performance of the chain. When the variance is large, the size of the jump from the current state to the proposed state is large, and the proposal is less likely to be accepted. As a result, the current state is repeated in the sequence, the acceptance rate drops, and the chain takes much longer to cover all the regions of the target distribution. If the spread is too

small, the size of the jump is small, and the proposal is more likely to be accepted. Consequently, the acceptance rate increases, but small regions of the target distribution are being visited. In both cases, the chain is said to be poorly-mixed, and high auto-correlation between samples are expected because either repetition in the case of low acceptance rate, or the samples are in close proximity to each other—as in the case of high acceptance rate. Although, from a computational perspective it is advantageous to have a higher acceptance rate, it should not come at the cost of chain mixing. In practice, the variance of the proposal is used as a tuning parameter to achieve a good balance between acceptance ratio and chain mixing. Some research suggests that if both the proposal and the target distributions are Gaussian, the variance should be tuned to achieve acceptance ratios of approximately 0.45 in one-dimensional cases and 0.23 as the number of dimensions approaches infinity (Chib and Greenberg 1995).

2.4.2.3 Convergence Diagnostics

Both the number of iterations that are needed for the chain to converge to the target distribution, and the number of iterations that are necessary, thereafter, to provide accurate estimates, are determined empirically (Chib and Greenberg 1995). Many different methods and approaches have been developed to test for convergence. The most common ones are described in this section.

The most common approach uses time-series plots. In such plots, a scalar estimate of interest is monitored. Examples of such estimates include model parameters, functions of model parameters, predicted future values, or values of the logarithm of the posterior density (Gelman et al. 2013). When the trace is moved from an initial value and appears

to have converged or settled around a certain value, it may be concluded that all members preceding this point are burn-in. However, there is no guarantee that the actual burn-in period would be much higher than that indicated by the trace (Walsh 2004). At least, time-series trace plots are useful in determining the minimum number of members that may be considered as burn-in.

Another approach, suggested by Gelman and Rubin (1992), is to run multiple chains and compare the variability within and between chains to gain information about convergence and stationarity. The authors argue that one cannot determine for any particular problem if a single chain has converged. It is only through running multiple chains that one can make inferences about sampling variability. In this work, a starting distribution that approximates the target distribution is first defined to obtain multiple starting values. Then, multiple sequences are run, and inferences from those sequences are obtained to estimate the target distribution. Geyer (1992), on the other hand, argues that inferences should be made based on one long Markov chain. He claims that similarities between multiple shorter chains do not necessarily imply convergence, and may, quite possibly, be induced by the experiment design. He concludes that the only value of multiple chain diagnostics is to signify the need for more runs when disagreement between chains is present.

Running one long Markov chain reduces dependency on the initial model. On the other hand, running several independent shorter sequences reduces the risk of bias on a slowly mixing chain with variability that is less than actual. Liu and Oliver (2003) addressed this debate using a small 1-D single-phase black-oil model, which,

unfortunately, did not contribute much to the resolution of this matter. Their results verify that (1) running shorter independent chains results in large differences of the means of individual chains, suggesting strong dependency on initial model, and (2) running longer chains results in slow mixing, suggesting less than actual variability.

Even after removing the burn-in period, adjacent members in the chain are expected to be positively correlated. This correlation can be quantified using an autocorrelation function (Walsh 2004). The correlation between members could introduce bias in estimating the target distribution when the sample size is not large enough to offset such effect. Walsh (2004) suggests the use of two time-series analysis plots: (1) the serial autocorrelation as a function of time lag, and (2) partial autocorrelation as a function of time lag. The author argues that these plots help underline correlation structure in the chain that is not as obvious when only looking at the time-series plot.

One simple and effective way to test for stationarity is suggested by Geweke (1992). This test suggests splitting the chain into two subsamples after discarding the burn-in period. If the chain is stationary, both subsamples should have similar means. A modified z-test can be done on both subsamples. Typically, values greater than two indicate that the mean is still drifting, and the distribution has not yet converged.

Raftery and Lewis (1992) introduced another method that determines how many initial runs should be discarded, the total chain length, and what thinning ratio (i.e., only retain every k^{th} element in the chain to offset autocorrelation) should be applied to the chain values. In their method, the problem is formulated by calculating a quantile of the posterior function with a certain specified accuracy. The chain is run for an initial number

of iterations. Then, using those iterations, specified quantile, and required accuracy, the number of burn-in runs and the total number of additional runs can be calculated.

Oliver et al. (2008, 145) state that in the case of a linear forward model, the minimum of the objective function follows a χ^2 distribution with degrees of freedom equal to half the number of observations, $N_d/2$. The authors also claim that this result reasonably applies to nonlinear cases. They suggest the use of a region of five standard deviations from the mean as a measure of the quality of Maximum a Posteriori (MAP) estimate,

$$N_d - 5\sqrt{2N_d} \leq 2\,O(\theta_{MAP}) \leq N_d + 5\sqrt{2N_d} \tag{13}$$

In the context of Bayesian methods, this identifies a point of reference to where the mode of the posterior lies. This also serves to indicate that the chain is sampling regions of high posterior probability or, perhaps, is either in transition or stuck in regions of low posterior probability.

2.4.2.4 Improved Forms of MCMC in Reservoir Simulation

Typical application of MCMC in reservoir engineering problems requires reservoir simulation to be run every time a candidate model is proposed in order to evaluate the likelihood part of the posterior function. Additionally, an initial sample of reservoir simulation models (usually hundreds and sometimes thousands) is considered burn-in and thus, is discarded. Even after the chain is stabilized, only accepted models are used for analysis; usually less than half of the reservoir simulation models are accepted.

Several modifications to the standard MCMC application have been proposed to make the process more efficient. They may be categorized into two approaches: (1) methods that aim to improve the proposal selection step of MCMC, and, hence,

increase the acceptance rate and reduce the burn-in period without sacrificing chain mixing quality, and (2) methods that do not require running a full reservoir simulation to evaluate the likelihood of either all proposals or, at least, some of them.

One approach to improve proposal selection are algorithms that use previously accepted states to "tune" the proposal distribution, such as Adaptive Proposal (AP), Adaptive Metropolis (AM), and Adaptive Genetic MCMC (Floris et al. 2001; Haario et al. 1999, 2001; Holden 1998). Another approach is the use of gradients or sensitivities in proposal selection (Efendiev et al. 2005; Ma et al. 2008). Emerick and Reynolds (2010, 2011) suggested a proposal selection approach based on an ensemble of realizations updated using EnKF.

The second group of methods usually involve an intermediate step where the full reservoir simulation is replaced by an up-scaled representation (i.e., flow up-scaling or spatial up-scaling), or approximated using gradient or sensitivity calculations (Efendiev et al. 2005; Ma et al. 2008). Another approach to approximating the forward model is by statistically estimating gridblock parameters and dynamic variables, and calculating forecasted well output using Peaceman equations (Emerick and Reynolds 2011).

2.4.3 Randomized Maximum Likelihood

Randomized maximum likelihood (RML) is a variation of the M-H algorithm introduced by Oliver et al. (1996). It can be shown that for a linear problem, RML accurately samples the posterior distribution. The algorithm can be summarized by the following steps:

1. Draw an unconditional pair of model parameters (θ_s) and perturbed observations ($d_{\text{obs},s}$) from a joint Gaussian distribution.
2. Find $\theta = \theta_{cal}$ that minimizes the distance between the points $(\theta_s, d_{\text{obs},s})$ and $\big(\theta, g(\theta)\big)$.
3. Use M-H criteria to either accept or reject the proposal from step 2.

$$\alpha(\theta_{t-1}, \theta_{cal}) = \min\left(1, \frac{\pi(\theta_{cal})}{\pi(\theta_{t-1})} \frac{q_t(\theta_{cal}, \theta_{t-1})}{q_t(\theta_{t-1}, \theta_{cal})}\right) \tag{14}$$

4. Go back to step 1 and continue until a sufficient number of samples are generated.

Because a minimization problem is used to obtain the proposal θ_{cal}, no analytical form is available to define the proposal density $q_t(\cdot)$. Theoretically, the calculation of the proposal at θ_{cal} involves an integration over the space of perturbed measurements and the calculation of the Jacobian of θ_s to θ_{cal} (see Oliver et al. 1996). This cannot be calculated for most nonlinear problems. As an approximation, it is suggested that either all proposed states are accepted (i.e., implicitly making the assumption that θ_{cal} is sufficiently close to θ_s), or dropping the ratio of proposal densities in Eq. 10 (i.e., implicitly making the assumption that the proposal densities are symmetric). Ma et al. (2008) provides an analysis of the RML method and suggests that assumptions made in the nonlinear case could be easily violated.

2.5 Sequential Updating Methods (Recursive)

In these methods, reservoir parameters and states (e.g., gridblock pressures and saturations) are updated whenever new measurements become available. The new estimate is a function of both the previous estimate and recently observed measurements. A Bayesian formulation can be developed, using a set of observations d_t for recursively estimating a vector of parameters m and a vector representing the states of the model at specific times X_t, as illustrated in **Fig. 1.**

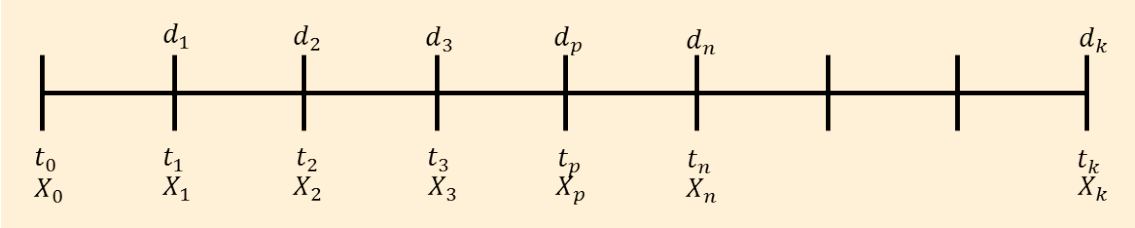

Fig. 1—Discretization in time to illustrate the process of recursive methods in updating model parameters and states, as newly observed measurements are assimilated.

Using Markov assumptions for the states **(Eq. 15),** and assuming that observations at a particular time t_n are related only to current estimates of model states and parameters **(Eq. 16),** the joint probability function of model parameters and model states is calculated using **Eq. 17.**

$$X_{t_i} = g\left(X_{t_{i-1}}, m\right) \tag{15}$$

$$d_{t_i} = h\left(X_{t_i}, m\right) \tag{16}$$

$$f(X_1, \dots, X_n, m) \propto f(m) \prod_{i=1}^{n} f(X_i | X_{i-1}, m) \tag{17}$$

Assuming measurement errors that are not correlated in time and using conditional probability rules **(Eq. 18),** the probability of the joint distribution of model parameters and states conditioned on all observed measurements available is calculated using **Eq. 19.**

$$(d_{\text{obs}} | X_1, \dots, X_n, m) \propto \prod_{i=1}^{n} f\left(d_{\text{obs},i} \middle| X_i, m\right) \tag{18}$$

$$\begin{aligned} &f(X_1, \dots, X_n, m | d_{\text{obs}}) \\ &\quad \propto f(m) \prod_{i=1}^{n} f(X_i | X_{i-1}, m) \prod_{i=1}^{n} f\left(d_{\text{obs},i} \middle| X_i, m\right) \end{aligned} \tag{19}$$

Equation 19 may, alternatively, be expressed as:

$$\begin{aligned} &f\left(X_1, \dots, X_n, m \middle| d_{\text{obs},1}, \dots, d_{\text{obs},n}\right) \\ &\quad \propto f\left(X_1, \dots, X_p, m \middle| d_{\text{obs},1}, \dots, d_{\text{obs},p}\right) f\left(X_n \middle| X_p, m\right) f\left(d_{\text{obs},n} \middle| X_n, m\right) \end{aligned} \tag{20}$$

In **Eq. 20,** the posterior density of the joint distribution of model states and parameters is expressed as the product of three functions: (1) estimate of the joint distribution from the previous time step, p, (i.e., prior); (2) the forecast of model states from the previous time step to the current time step; and (3) the conditioning on newly observed measurements (i.e., update step).

A classical approach to sequential updating in linear problems is the Kalman Filter (KF). EnKF is an extended version of KF designed for large and non-linear problems. Both methods are presented in the following subsections.

2.5.1 Kalman Filter

Kalman (1960) developed a theory for optimal estimation of the states of a linear model by recursively assimilating noisy measurements that are linearly related to the states. The estimate is derived to satisfy unbiasedness and minimum squared error (MSE)

conditions, assuming measurement noises that are uncorrelated in time, and assuming that measurement noise and model noise are independent. The KF method is summarized concisely by Aanonsen et al. (2009). First, a model with a state vector x_t that is related linearly only to the states of the model at the previous time step (i.e., Markov assumptions) is assumed **(Eq. 21).**

$$x_t = Ax_{t-1} + w_t \tag{21}$$

Here, w_t is a modeling error with an expectation of zero. Also, d_t is a vector of noisy observed measurements that is linearly related to the states of the model,

$$d_t = Hx_t + v_t \tag{22}$$

Then, forecast estimates for the states at time t are only linearly dependent on the updated estimate from the previous time step **(Eq. 23).**

$$x_t^f = Ax_{t-1}^u \tag{23}$$

Here, the superscripts f and u denote the forecast and the update estimates, respectively. Also, the forecast of the error covariance is a linear function of the updated error covariance from the previous time step **(Eq. 24).**

$$C_{x_t}^f = AC_{x_{t-1}}^u A^T + C_\epsilon \tag{24}$$

Here, C_ϵ is a diagonal covariance matrix of model noise (i.e., non-correlated modeling errors). After assimilating a newly observed set of measurements, $d_{\text{obs},t}$, the updated state estimate is calculated using **(Eq. 25).**

$$x_t^u = x_t^f + K_t\left(d_{\text{obs},t} - Hx_t^f\right) \tag{25}$$

Where K_t is the Kalman gain,

$$K_t = C_{x_t}^f H^T \left(H C_{x_t}^f H^T + C_{d_t}\right)^{-1} \tag{26}$$

Finally, the updated error covariance is calculated using:

$$C_{x_t}^u = C_{x_t}^f - K_t H C_{x_t}^f \tag{27}$$

This may, alternatively, be expressed using the identity matrix *I*,

$$C_{x_t}^u = (I - K_t H) C_{x_t}^f \tag{28}$$

Eq. 28 describes the updated estimate as a linearly weighted average of the forecast estimate and information derived from observations. Eqs. 25 and **26** imply that during the forecast step, the error covariance increases (i.e., uncertainty around the estimate) by an amount that depends on the model noise covariance. After conditioning on the data, the error covariance decreases by an amount proportional to the Kalman gain (i.e., information obtained from the data). This means that the more noise there is around measurements, the less the Kalman gain, resulting in smaller improvement in estimation after assimilating the data (and vice versa).

Also, KF is a second order update. Although no Gaussianity assumptions are made in the derivation of the estimate, the update is only optimal if the underlying distribution is Gaussian. For any other distribution, the estimate is accurate only up to the second moment. For asymmetric distributions and distributions that are far from Gaussian, the first two moments might not be sufficient to characterize the distribution.

2.5.2 Ensemble Kalman Filter

EnKF was introduced by Evensen (1994) and is used extensively in weather forecasting. This method was first applied to reservoir engineering by Naevdal et al. (2002), who demonstrated its effectiveness in estimating permeability in the neighborhood

of a well using pressure measurements. In this method, an ensemble of models is used, and the model and measurement equations are not assumed to be linear **(Eqs. 29 and 30).**

$$x_t^{f,j} = f\left(x_{t-1}^{u,j}, m_{t-1}^{u,j}\right) \tag{29}$$

$$d_t^{f,j} = g\left(x_t^{f,j}, m_{t-1}^{u,j}\right) \tag{30}$$

Here, the superscript j denotes a particular member of an ensemble of size N_e. Additionally, we define an augmented vector $y_t^{f,j}$ that hosts the parameters, states, and forecasted model response **(Eq. 31).**

$$y_t^{f,j} \equiv \begin{bmatrix} m_t^{f,j} \\ x_t^{f,j} \\ d_t^{f,j} \end{bmatrix} \tag{31}$$

Adding the model response to the augmented state/parameter vector is a useful trick that allows the requirement of linear relationship between states and measurements to be removed **(Eq. 32).**

$$d_t^{f,j} = H y_t^{f,j} \tag{32}$$

Here H is a matrix that contains only zeroes and ones. Kalman gain is then defined in terms of the ensemble estimates of the error covariance and measurements covariance **(Eq. 33).**

$$K_t = \overline{\left(C_{y_t}^f\right)} H^T \left[H \overline{\left(C_{y_t}^f\right)} H^T + \overline{\left(C_{d_t}\right)}\right]^{-1} \tag{33}$$

This may, alternatively, be expressed in terms of the covariance operator,

$$K_t = \mathrm{cov}(y_t, d_t) \left[\mathrm{cov}(d_t, d_t) + \overline{\left(C_{d_t}\right)}\right]^{-1} \tag{34}$$

Finally, the updated augmented state/parameter vector is calculated using:

$$y_t^{u,j} = y_t^{f,j} + K_t\left[d_{\text{obs},t}^{j} - Hy_t^{f,j}\right] \tag{35}$$

It is worth mentioning that EnKF uses an ensemble of observed measurements, usually constructed by sampling a distribution with the actual observed measurements as the mean and some defined measurement error. The use of an ensemble-based representation for measurements is necessary to insure correct updated error covariance (Evensen 2009, 42).

In deriving the EnKF, there are no explicit assumptions about linearity or Gaussianity. Instead of linearly updating the mean and covariance estimates, those quantities are estimated using the updated ensemble members. Evensen (2009, 41-44) demonstrates that in the limit of an infinite ensemble, EnKF converges to the KF solution. This means for a joint Gaussian prior and a linear model, the EnKF samples the posterior correctly. In the case of a non-linear model, the forecast step is performed assuming full non-linearity, and the update step is a second-order weighted product of the forecast error covariance and measurement mismatch. Li and Reynolds (2007) show that for EnKF to sample the posterior correctly, the joint distribution at the update step is required to be Gaussian. This implies that the relationship between m, x, and d must be approximately linear. Clearly, this is a strong assumption.

One limitation of the EnKF approach is dependency on the initial ensemble. It is clear that any solution that is produced by the update lies in the subspace spanned by prior realizations. Thus, if the initial ensemble is limiting or does not correctly represent the prior, the results might be compromised. Evensen (2009, 165-168) suggests the use of an improved sampling strategy: first, a large number of realizations is sampled; then, the

initial ensemble is selected as the vectors corresponding to the leading singular values from the decomposition of the covariance matrix.

The standard applications of EnKF use an ensemble of perturbed measurements. This could introduce additional sampling errors. One way to handle this is to use square-root filters, thereby avoiding the use of perturbed measurements. Rather, the ensemble mean is updated separately using the means of the forecast ensemble and the observed measurements in **Eq. 35.** Then, an expression of the updated error covariance using the forecast ensemble is calculated, avoiding the use of perturbed measurements. See Aanonsen et al. (2009) and Evensen (2009, 197-203).

Additionally, because of the limited number of ensemble members, the updates might introduce artificial correlations between variables that would otherwise be uncorrelated. In such cases, covariance localization is performed. Several approaches to covariance localization are presented in the literature (Aanonsen et al. 2009), including distance-based methods, sensitivity-based methods, and methods that combine ensemble and spatial estimation.

Some state variables (e.g., water saturation at the location of the front) can have extremely non-Gaussian distributions. Additionally, the update step can result in non-physical values for the states. One simple solution to this problem is to truncate the distribution at its limit values. Other solutions use parameterization, forcing the states to be more Gaussian. Two examples are the use of saturation arrival time (Chen et al. 2009) to replace water saturation, and the use of discrete cosine transform (DCT) to

reparametrize the model parameter and state variables (Jafarpour and McLaughlin 2009a, 2009b).

Iterative methods are used to handle strong non-linearity and unphysical state values. Each member of the ensemble undergoes a minimization problem with respect to both its forecast value and new measurements. Refer to the literature for a few examples: Gu and Oliver (2007); Li and Reynolds (2007); and Reynolds et al. (2006), wherein RML is performed in the update step.

Two issues that arise when EnKF is used to update reservoir simulation models is lack of consistency and material balance errors. Because the updating process accounts for an evolving geological description, forecasts made using the final ensemble might not be consistent with forecasts derived from more simplistic models that use the same geological description for the entire run. Also, because the forecasted values of the states are changed during the update step of EnKF, and some values might be truncated, mass balance might not be maintained. In such cases, it is common to rerun the final ensemble from time zero to eliminate consistency issues and material balance errors.

Despite its limitations, EnKF is a promising model updating and data assimilation technique in reservoir management. The feature of not requiring the models to be run from time zero is particularly attractive. Since its introduction to the reservoir engineering literature in 2002, EnKF continues to be a subject of rapidly growing research.

2.6 Parameterization

The major goal of parameterization methods in the context of the inverse problem is to reduce the number of parameters. Advantages of a smaller parameter space include a better-posed problem, less redundancy (i.e., exploit correlations), and less computational overhead. Two major approaches to parameterization in reservoir simulation are spatial and linear transformation methods.

In the first approach, spatial upscaling or coarsening of grid-cells are usually performed. One basic approach is to uniformly merge a number of grid-cells to form coarser grid-cells. In some of these methods, the basis of upscaling is geological similarity. Other methods use an adaptive approach where finer grid-cells are used in different regions/clusters to include a more detailed geological description. Usually, a prior knowledge of the geology or information from the history-match gradient, e.g., gradzone method (Bissell 1994), is used to define the clusters where refinement is needed.

In the second approach, a linear mapping between the parameters at the original domain and some reduced codomain is applied. The goal of this method is to construct a set of mapping vectors Φ such that some of the weights α corresponding to these vectors are equal to or nearly equal to zero **(Eq. 36).**

$$m_{[N\times 1]} = \sum_{i=1}^{N} \phi_i \alpha_i \approx \sum_{i=1}^{k} \phi_i \alpha_i \qquad k < N \tag{36}$$

Eq. 36 describes a linear mapping constructed so that the weights of columns $(k + 1, \dots, N)$ are negligible, so that the number of parameters is effectively reduced to k parameters. The inverse problem is then solved with respect to α. When an estimate of the parameter at the reduced space is generated, the inverse of this mapping is used to return

to the original domain. Linear transformation methods use a variety of approaches for calculating the linear mapping, Φ.

One common approach is the Karhunen-Loeve (K-L) linear transform, which uses Principal Component Analysis (PCA) to construct the transformation matrix. In this approach, the eigenvalue decomposition of the covariance matrix is used, and only the vectors corresponding to the leading eigenvalues are retained.

$$m = \Phi \sqrt{\lambda}\ \alpha + \bar{m} \tag{37}$$

Here, Φ is the matrix corresponding to the leading singular vectors, $\sqrt{\lambda}$ is the diagonal matrix corresponding to the square-root of the leading singular values of the covariance matrix, and α is a random Gaussian variable with a mean of zero and unit variance. Because the parameterization is covariance dependent, prior knowledge of the true covariance matrix or a good approximation thereof is required. (This is not a requirement in most parameterization schemes.) The accuracy of the parameterization depends on how well the covariance matrix can be approximated using prior information.

Another method is the Gradual Deformation Method (GDM) (Hu 2000). In this method, a new realization is generated by linearly combining k realizations using the relationship:

$$m = \bar{m} + r_k\ \alpha \tag{38}$$

Here r_k is a matrix with column representing the residual of prior realizations with respect to the mean, and α is vector of variance normalizing constants defined by the relationship:

$$a_i = \begin{cases} \prod_{j=1}^{k} \cos(t_j), & i = 0 \\ \sin(t_i) \prod_{j=i+1}^{k} \cos(t_j), & i = 1,..,k-1 \\ \sin(t_i), & i = k \end{cases} \quad (39)$$

Here, $(t_0, \dots, t_m)$ are random variables drawn from a uniform distribution defined on $[-\pi, \pi]$. As in K-L, any new realization is sampled from the subspace spanned by the k prior realizations. Accurate GDM parameterization depends on how well these realizations cover the parameter space.

Jafarpour and McLaughlin (2009b) introduced the Discrete Cosine Transform (DCT) to the inverse problem in reservoir simulation. In DCT, an orthonormal set of basis functions is used to perform the mapping **(Eq. 40).**

$$\phi_{i,j} = \cos\left[\frac{\pi(2j+1)i}{2j}\right] \quad (40)$$

The advantage of DCT, when compared to K-L and GDM, is that it is data independent (i.e., no approximation of the covariance or prior realization is required). The number of basis vectors are chosen according to the required resolution. DCT can achieve up to 95% reduction in the number of parameters and still provide a reasonably good approximation. Additionally, prior information regarding the orientation and direction of some geological features may be incorporated to improve basis function selection and the quality of approximation (Jafarpour and McLaughlin 2009b).

3. MULTI-LEVEL CONTINUOUS MODEL UPDATING AND UNCERTAINTY QUANTIFICATION USING ENKF/TWO-STAGE MCMC: METHODOLOGY AND ALGORITHM

In this section, the multi-level continuous model updating and uncertainty quantification procedure using EnKF/two-stage MCMC is presented. The procedure is composed of two major levels. In the first level, recursive updating is performed using EnKF at a higher frequency. After a specified number of assimilation cycles, the second level is reached and model updating is performed using a two-stage MCMC approach and utilizing the entire available production history at the time (i.e., non-recursive).

Adopting this multi-level approach takes advantage of the computational efficiency of EnKF and the robustness of MCMC. In this procedure, the posterior covariance estimated at the end of the first level is used in the proposal selection at the MCMC level. Additionally, because the EnKF posterior covariance includes both model parameters and states, it can be used to approximate reservoir response at the first stage of MCMC, which can significantly improve efficiency by reducing simulation run requirements.

This procedure differs from the Emerick and Reynolds (2011) combined EnKF-MCMC approach in the way the likelihood function is handled. In the multi-level EnKF/two-stage MCMC, the likelihood function is calculated exactly rather than approximated. To reduce the computational cost associated with the exact evaluation of the likelihood, a filter stage of MCMC is introduced where the likelihood function is

approximated using information obtained from the posterior covariance. Doing so preserves the requirements of generating valid samples through MCMC while capitalizing on the information obtained during the EnKF level to guide the proposal selection and to evaluate the proposals at the filter stage.

This multi-level approach mimics the multi-level nature of the production and decision cycles in the actual field production environment. By adopting this approach, the operators are provided with models that are updated rapidly and can be used in short-term decision and operation cycles. A more rigorous model update and uncertainty characterization is available at a lower frequency and can be used in longer-term decision and operation cycles.

3.1 The General Workflow

As shown in **Fig. 2,** this workflow is composed of two major levels: EnKF level, and two-stage MCMC level. In the first level, the updated ensemble from the previous assimilation cycle is forecasted to the end of the current assimilation cycle using reservoir simulation. Then, observed measurements are used to update the ensemble—as described in the EnKF approach **(Eqs. 29–35).** This process continues recursively until a specified number of assimilation cycles is achieved. In the second level, two-stage MCMC is performed. Before the MCMC chain is initialized, a matrix, $Y_{t_{1,t_f}}$, collecting the parameters and the states (from the first assimilation cycle, t_1, up to current assimilation cycle, t_f) for all the ensemble members is assembled **(Eq. 41).**

$$Y_{t_1,t_f} = \begin{bmatrix} y^1_{t_1,t_f} & \dots & y^{N_e}_{t_1,t_f} \end{bmatrix} = \begin{bmatrix} m^1_{t_f} & \dots & m^{N_e}_{t_f} \\ X^1_{t_1} & \dots & X^{N_e}_{t_1} \\ \vdots & \dots & \vdots \\ X^1_{t_f} & \dots & X^{N_e}_{t_f} \end{bmatrix} \quad (41)$$

In Eq. 41, m is a column that contains model parameters, X is a column that contains model states (e.g., gridblock pressures and saturations), the subscripts denote the time-step, and the superscripts denote the ensemble member. The covariance matrix is then calculated using **Eq. 42.**

$$C_{Y\,t_1,t_f} = \frac{\Delta Y_{t_1,t_f}\,\Delta Y^T_{t_1,t_f}}{N_e - 1} \quad (42)$$

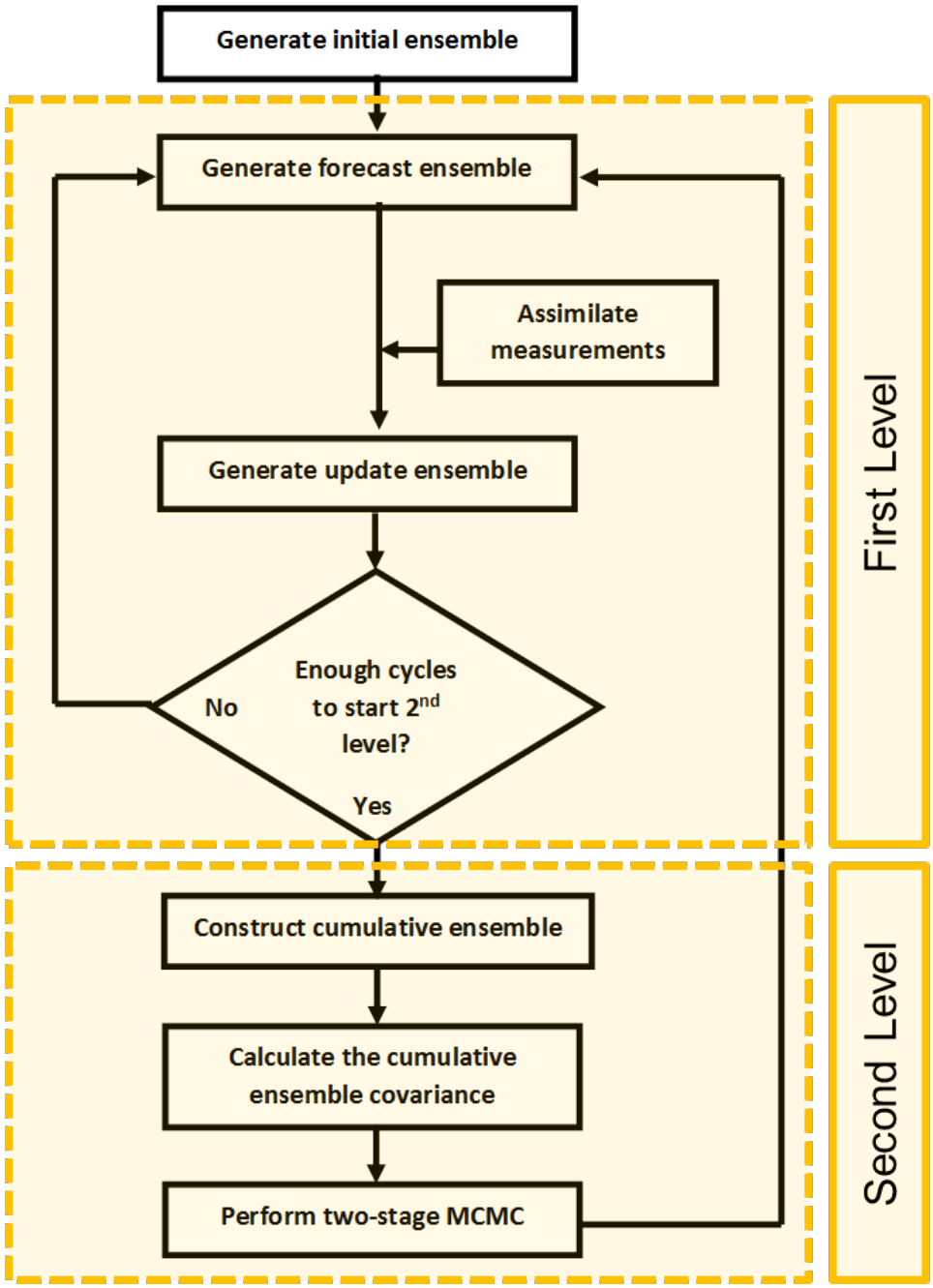

Fig. 2—The general workflow of the multi-level continuous model updating the uncertainty quantification procedure.

Here, $\Delta Y_{t_1,t_f}$ is a matrix with columns that contain the residuals of the columns of Y_{t_1,t_f} around the column mean of Y_{t_1,t_f} **(Eq. 43).**

$$\Delta Y_{t_1,t_f} = Y_{t_1,t_f} - \overline{Y_{t_1,t_f}} \tag{43}$$

In the equation above, $\overline{Y_{t_1,t_f}}$ is a matrix with each column containing the column mean of Y_{t_1,t_f}. The covariance matrix calculated in Eq. 42 is used to propose samples in the MCMC level.

As shown in **Fig. 3,** the two-stage MCMC process starts with drawing a random realization from the proposal distribution **(Eq. 44).**

$$y^{(0)}_{t_1,t_f} = \overline{y_{t_1,t_f}} + C^{\frac{1}{2}}_{Y_{t_1,t_f}} \hat{z} \tag{44}$$

Here, $C^{\frac{1}{2}}_{Y_{t_1,t_f}}$ is the square-root of the covariance matrix, and $\hat{z}$ is a Gaussian random variable with a mean of zero and some variance. Then, the sampled realization is run using the ECLIPSE® reservoir simulator and the exact likelihood is calculated using **Eq. 45.**

$$L\left(m^{(0)}\right) = \exp\left\{-\frac{1}{2}\left(g\left(m^{(0)}\right) - d_{\text{obs}}\right)^T C_D^{-1}\left(g\left(m^{(0)}\right) - d_{\text{obs}}\right)\right\} \tag{45}$$

Here, $g\left(m^{(0)}\right)$ is the predicted well measurements (e.g., well bottom-hole pressures (BHP) and rates) calculated using both reservoir simulation and $m^{(0)}$. The posterior function is evaluated using **Eq. 46.**

$$\pi\left(m^{(0)}\right) = \exp\left\{-\frac{1}{2}\left[\left(m^{(0)} - m_o\right)^T C_M^{-1}\left(m^{(0)} - m_o\right) + \left(g\left(m^{(0)}\right) - d_{\text{obs}}\right)^T C_D^{-1}\left(g\left(m^{(0)}\right) - d_{\text{obs}}\right)\right]\right\} \tag{46}$$

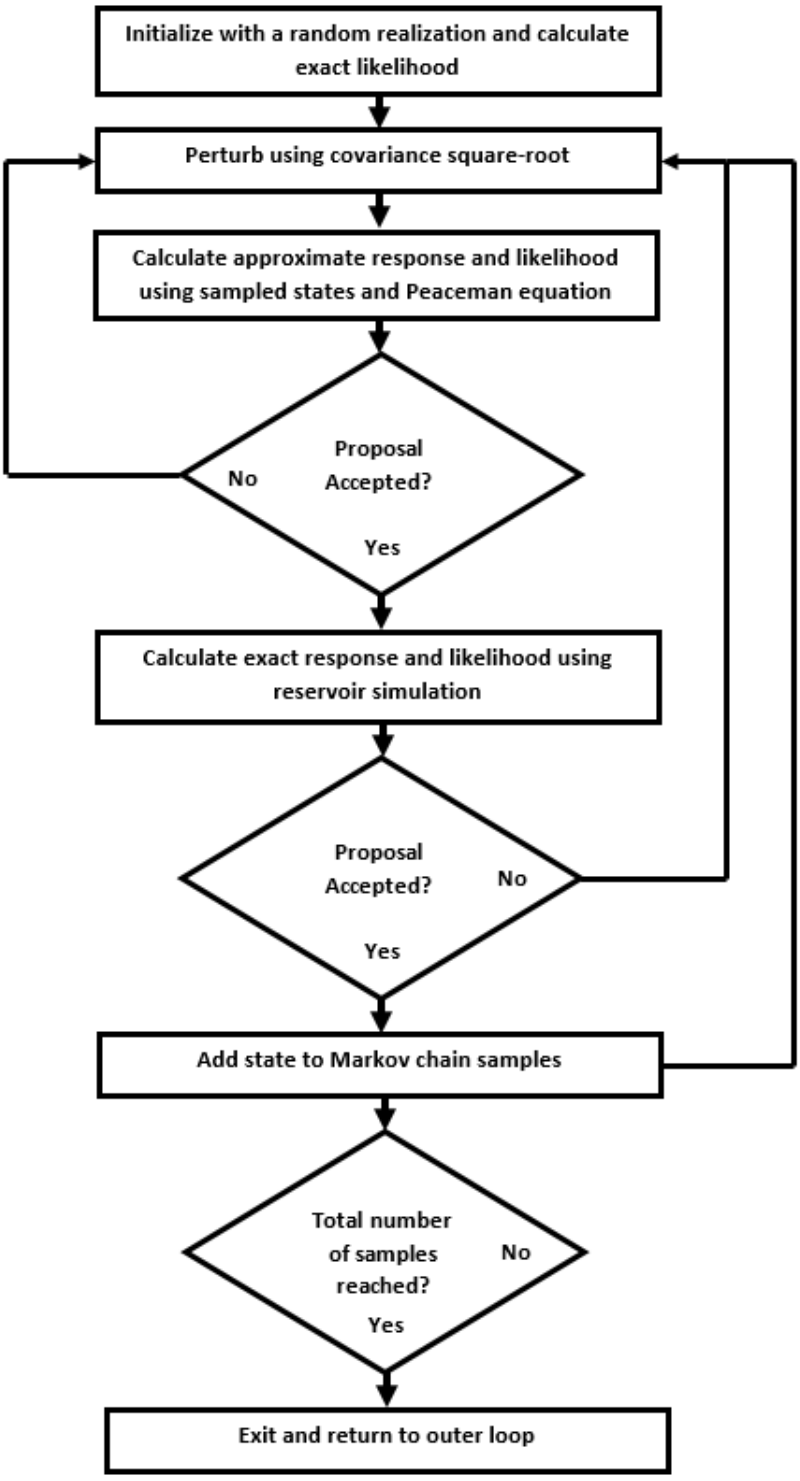

Fig. 3—Two-stage MCMC workflow using EnKF-based proposal density and Peaceman equations.

Then, this initial sample is perturbed using the covariance square-root **(Eq. 47).**

$$y_{t_1,t_f}^{(k)} = y_{t_1,t_f}^{(k-1)} + C_{Y_{t_1,t_f}}^{\frac{1}{2}} \hat{z} \tag{47}$$

Peaceman equations (Peaceman 1978) are used to directly calculate well profiles using the model parameters and states at well locations, $y_{t_1,t_f}^{(k)} \mid_{\text{wells}}$. The approximate likelihood is then calculated using **Eq. 48.**

$$L^*\left(m^{(k)}\right) = \exp\left\{-\frac{1}{2}\left(g^*\left(m^{(k)}, x^{(k)}\right) - d_{\text{obs}}\right)^T C_D^{-1}\left(g^*\left(m^{(k)}, x^{(k)}\right) - d_{\text{obs}}\right)\right\} \tag{48}$$

Here, $g^*(\cdot)$ is the well profiles calculated by Peaceman equations. The approximate posterior is calculated using **Eq. 49.**

$$\pi^*\left(m^{(k)}\right) = \exp\left\{-\frac{1}{2}\left[\left(m^{(k)} - m_o\right)^T C_M^{-1}\left(m^{(k)} - m_o\right) + \left(g^*\left(m^{(k)}, x^{(k)}\right) - d_{\text{obs}}\right)^T C_D^{-1}\left(g^*\left(m^{(k)}, x^{(k)}\right) - d_{\text{obs}}\right)\right]\right\} \tag{49}$$

The acceptance ratio at the first stage of MCMC is then calculated according to Metropolis-Hasting algorithm **(Eq. 50**Error! Reference source not found.**).**

$$\alpha = \min\left(1, \frac{\pi^*\left(m^{(k)}\right)}{\pi^*\left(m^{(k-1)}\right)}\right) \tag{50}$$

If the proposed sample is rejected, then the sample is discarded, and the current accepted sample in the chain is perturbed again. If the proposed sample is accepted, it enters the second stage of MCMC. In the second stage of MCMC, the proposed sample is run using ECLIPSE® and the exact likelihood and posterior are calculated. The two-stage Metropolis-Hasting acceptance ratio (refer to Appendix A.2) is calculated using **Eq. 51.**

$$\beta = \min\left(1, \frac{\pi\left(m^{(k)}\right)}{\pi\left(m^{(k-1)}\right)} \frac{\pi^*\left(m^{(k-1)}\right)}{\pi^*\left(m^{(k)}\right)}\right) \tag{51}$$

If the proposed sample is accepted at the second stage, it is added to the chain. If the sample is rejected at the second stage, the current accepted sample is repeated in the chain, and the process goes back to perturbation at the first stage. When the chain converges and enough samples are collected, the MCMC level terminates, and the process goes back to the EnKF level again.

3.2 The Algorithm

- First level
    1. Perform the forecast step of EnKF on the initial ensemble by forecasting each member of the initial ensemble to the end of the first assimilation cycle using ECLIPSE® reservoir simulator.
    2. Collect model states and parameters, as well as forecasted model response for the entire ensemble.
    3. Perform the update step of EnKF using the observed measurements.
    4. Store the updated model states and parameters.
    5. Initialize the ensemble for the next assimilation cycle using the updated model parameters and states.
    6. Repeat until a specified number of assimilation cycles are reached, and then enter the second level.
- Second level
    1. Construct the cumulative ensemble (Eq. 41).

2. Calculate the covariance matrix and the square-root of the covariance matrix (Eqs. 42 **Error! Reference source not found.**and 43).
3. Initialize the two-stage MCMC by drawing a random realization (Eq. 44), run the sample using ECLIPSE®, calculate the exact likelihood (Eq. 45) and the exact posterior (Eq. 46).
4. Perturb using the square-root of the covariance matrix (Eq. 47).
5. Calculate predicted well measurements using $y_{t_1,t_f}^{(k)} \Big|_{\text{wells}}$ and Peaceman equations.
6. Calculate the approximate likelihood and posterior (Eqs. 48 and 49).
7. Calculate the Metropolis-Hasting acceptance probability (Eq. **Error! Reference source not found.**).
8. If the proposal is rejected, return to step 4. If the proposal is accepted, enter the second stage of MCMC.
9. Run the proposal using ECLIPSE®.
10. Calculate the exact likelihood and posterior.
11. Calculate the two-stage Metropolis-Hasting acceptance probability (Eq. 51).
12. If the proposal is rejected at the second stage, repeat the current accepted sample in the chain and return to step 4. If the proposal is accepted, save the sample in the chain and return to step 4.
13. Continue until the chain reaches stationarity and the desired number of samples are being collected.

14. Exit the second level, and return to the first level.

4. MULTI-LEVEL ENKF/ONE-STAGE MCMC SAMPLING: 1-D SINGLE-PHASE TEST PROBLEM

In this section, multi-level EnKF/one-stage MCMC sampling approach is used to investigate the impact of using EnKF posterior covariance in the proposal selection of MCMC on the accuracy of sampling and efficiency of the process.

Here, the multi-level algorithm (Fig. 2) is applied only one time (i.e., not continuously), and without the use of a two-stage approach in the MCMC level, to sample the posterior of a relatively small 1-D single-phase test problem conditioned to 18 pressure measurements.

First, two long chains are generated using standard random-walk perturbation to establish a posterior distribution that can be used as a reference case. Analysis of the statistics within and across the two chains are used to assess convergence and stationarity of this posterior distribution. Then, a chain generated by the multi-level approach is compared to this reference posterior. To assess only the impact of the multi-level approach on chain convergence and mixing, the scaling factor of the proposal is kept the same for all the chains. Assessment of the multi-level sampling accuracy and improvement in efficiency is provided.

The relatively small size of the simulation model (20 gridblocks) and small total simulation time (0.1 days) make it feasible to run extremely long chains (close to one million iterations) and allow for more thorough investigation of convergence, stationarity, chain-mixing and dependence on initial guess.

The following subsections explain the simulation model and the prior used in this problem. It also presents and discusses the results of the EnKF updating case, the reference case, and the multi-level EnKF/one-stage MCMC sampling algorithm.

4.1 Simulation Model Description and Prior Definition

4.1.1 Simulation Model

The simulation model constructed for this work is adopted from Liu and Oliver (2003). The 1-D mode is discretized into 20 Cartesian gridblocks. Each gridblock is $50\times50\times50$ ft^3. The flow is single phase with an oil viscosity of 1 cp. The initial reservoir pressure is 3500 psi, the initial water saturation is 0.1. The porosity at the initial pressure is 0.25 and the rock compressibility is $3x10^{-6}$ psi^{-1}. The total simulation time is 0.1 hours discretized over six time steps.

Three wells are modeled and located at gridblocks 7, 13, and 18. The well located in gridblock 13 is an oil producer operated with a constant rate of 4000 bpd. The other two wells are observation wells.

A true synthetic permeability field **(Fig. 4)** is used to generate pressure data **(Fig. 5).** Gaussian noise was added to the true pressure drop data with a standard deviation of 0.5 psi.

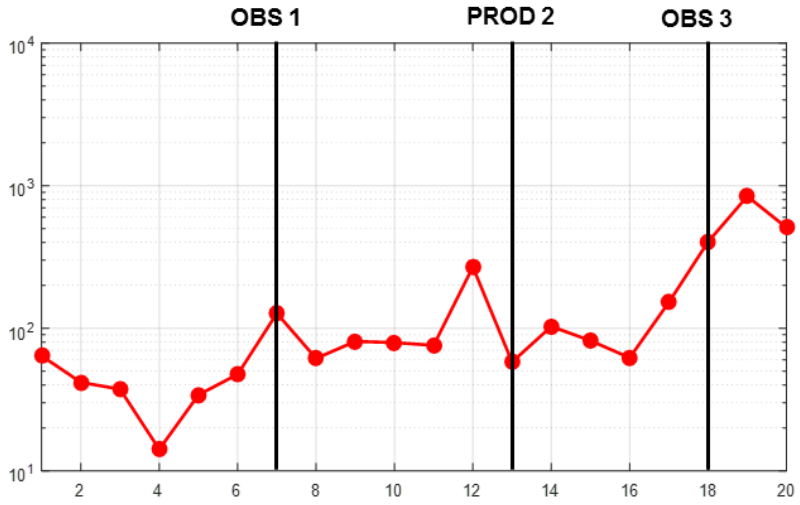

Fig. 4—True permeability field for the 1-D single-phase test problem showing well locations.

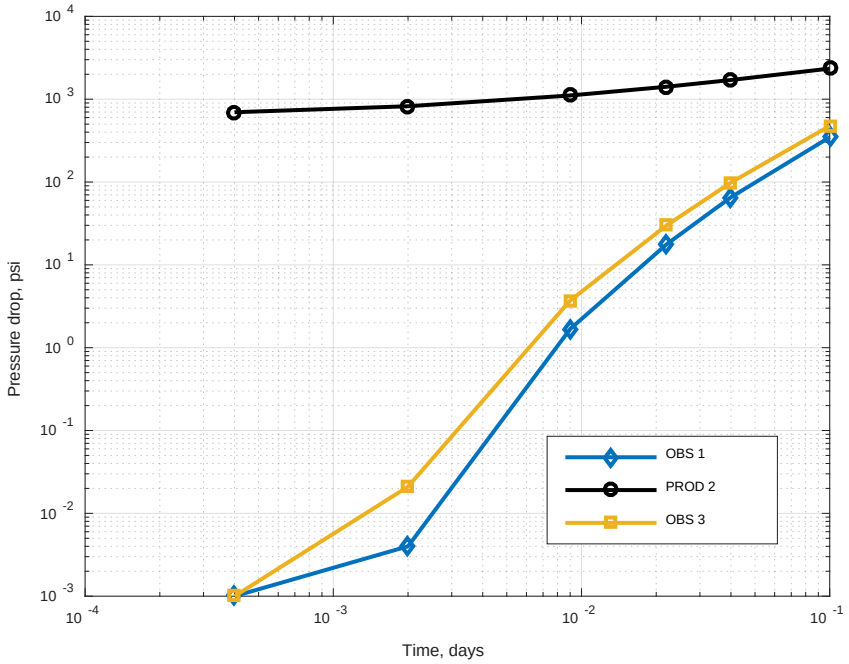

Fig. 5—Pressure drop measurements for the truth case of the 1-D single-phase test problem (without noise).

4.1.2 Prior Distribution

The prior distribution of log-permeability field, m, is assumed to be a multivariate Gaussian distribution with a mean of 4.5 and an exponential covariance, C_M, with a range of 175 ft. **Fig. 6** shows the initial ensemble of permeability for 500 realizations, sampled from the prior distribution. **Fig. 7** shows the standard deviations for the gridblock permeability values estimated from the initial ensemble. The values range from 100 to 400 mD.

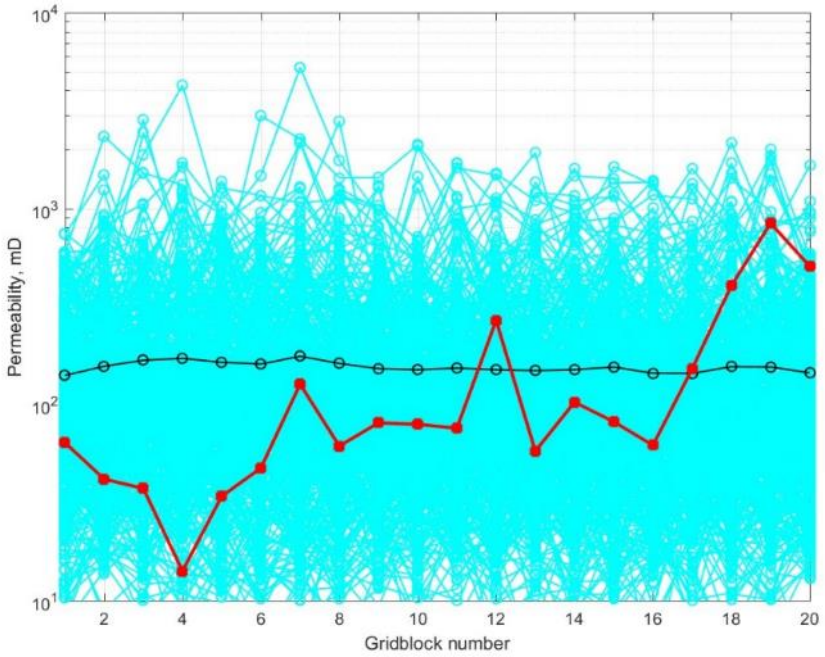

Fig. 6—Initial ensemble for the test problem showing the 500 initial realizations (cyan), the mean realization of the initial ensemble (black) and true permeability field (red).

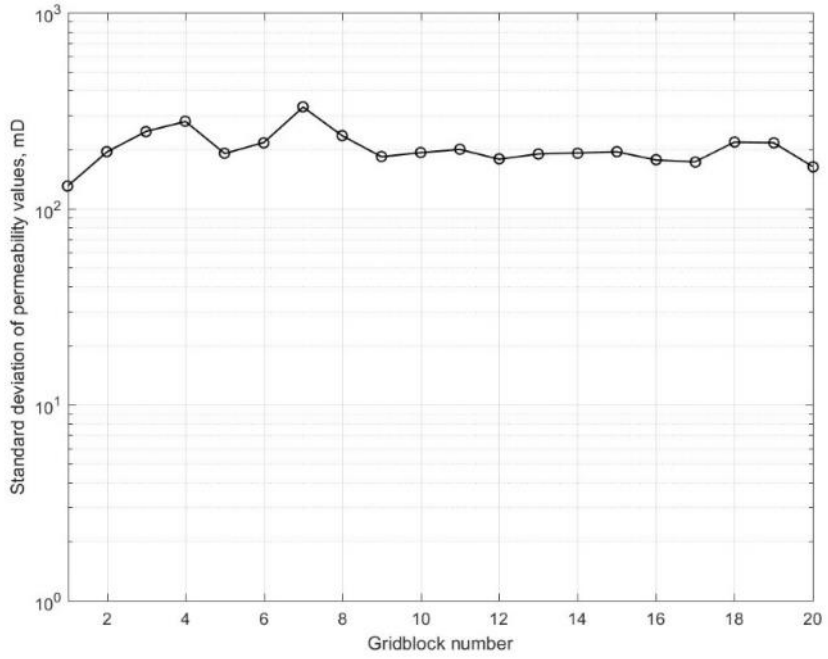

Fig. 7—Standard deviation values for the permeability field of the initial ensemble for the test problem.

4.2 EnKF Updating Case

Fig. 8 shows the permeability fields for the EnKF realizations across the six updates. The plots show continuous narrowing down of the range of the permeability realizations around the true realization as more data are assimilated. Also, the mean error estimate (i.e., the difference between the mean realization and the true realization) continues to reduce, particularly at and close to the location of the producer well.

Fig. 9 shows, in general, a continuous decline for the standard deviation estimates of the gridblock permeability values as more data are assimilated. The decline in standard deviation is more prominent at the location of the producer well. This is because the

correlation between the observed data and the permeability value is the strongest where the producer well is located.

Fig. 10 shows the posterior objective function values calculated for the final ensemble, updated by EnKF algorithm for the test problem. The values show a mean of 14,193 and a standard deviation of 20,091. The minimum of the objective function values is 413, and the maximum is 265,637. The prior term of this objective function shows values that range from close to zero to approximately 60 with a mean close to 18. The small contribution of the prior term in the calculation of the posterior indicates that the posterior function values are driven mostly by the likelihood term, the observed data mismatch.

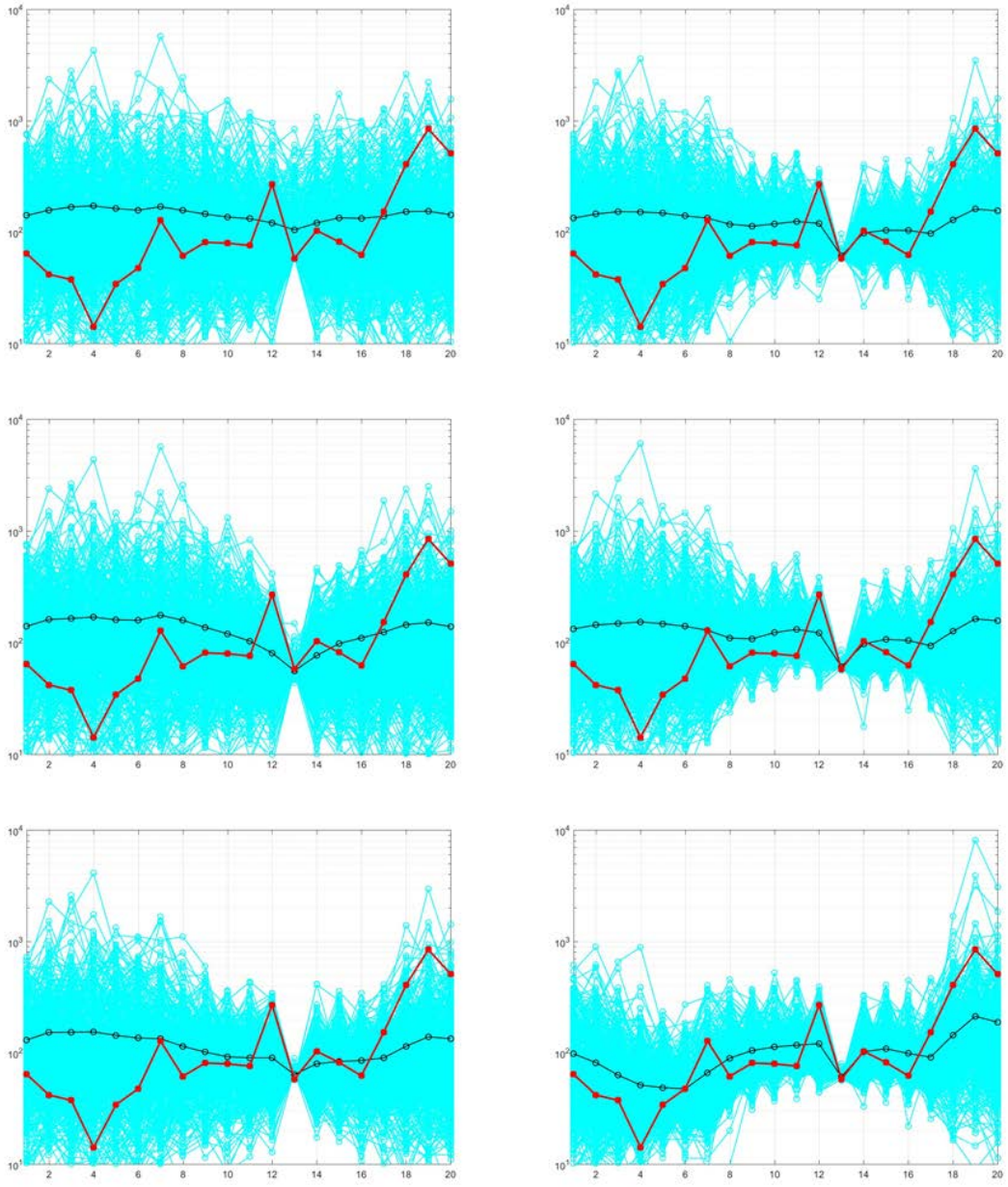

Fig. 8—Permeability fields for the updated ensembles using EnKF showing the ensemble realizations (cyan), mean ensemble realization (black) and the true realization (red): 1st update (top left), 2nd update (middle left), 3rd update (bottom left), 4th update (top right), 5th update (middle right) and 6th update (bottom right).

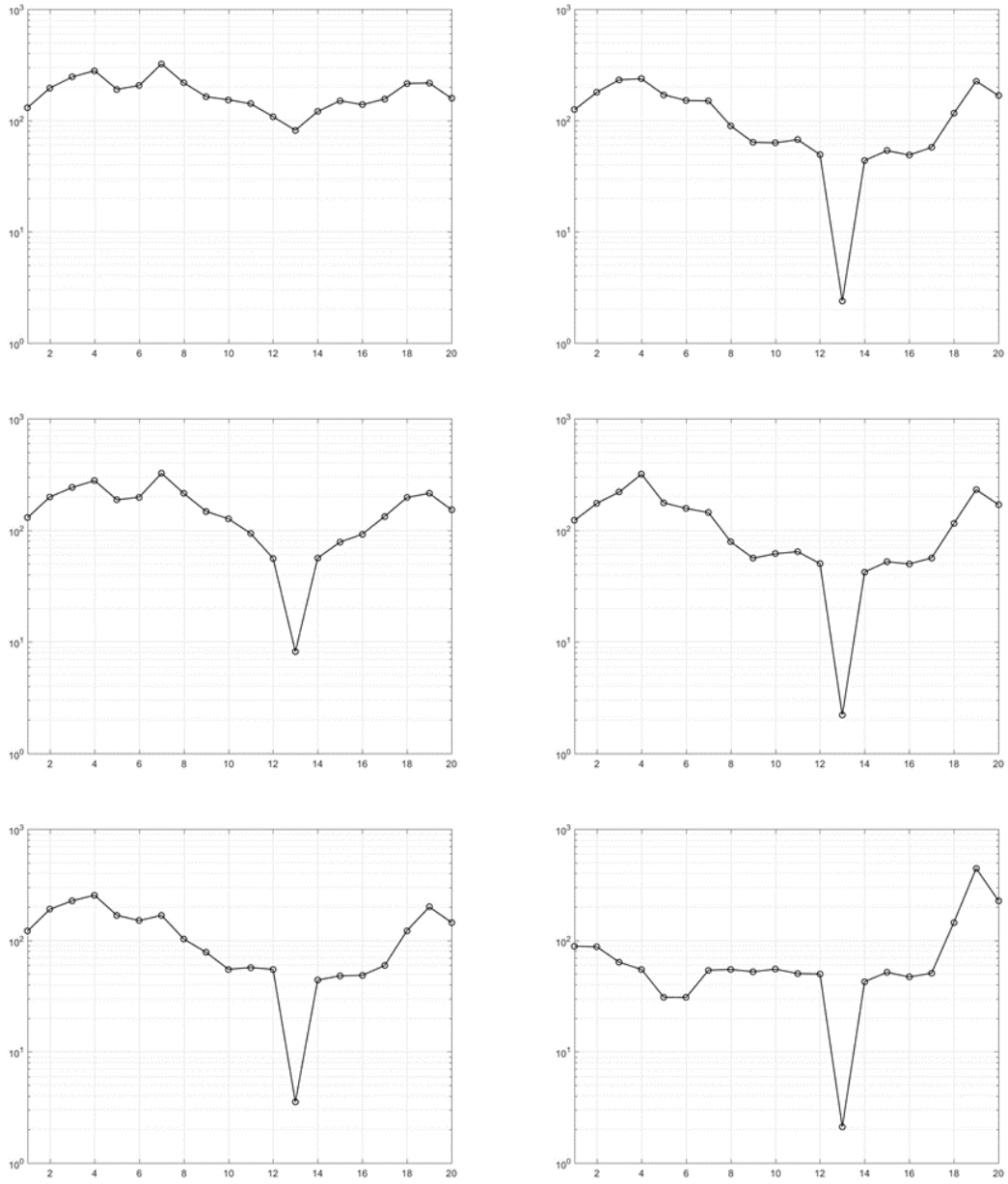

Fig. 9—Standard deviation values for the permeability field for the updated ensembles using EnKF: 1st update (top left), 2nd update (middle left), 3rd update (bottom left), 4th update (top right), 5th update (middle right) and 6th update (bottom right).

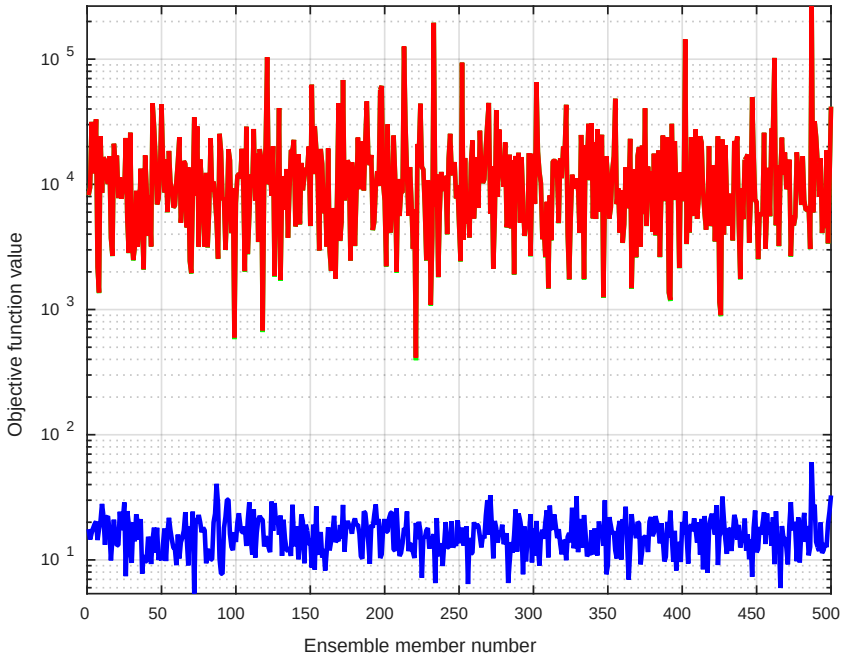

Fig. 10—Posterior objective function values (red) and prior term values (blue) for the final ensemble generated by EnKF for the test problem.

4.3 Standard Random-Walk Perturbation Case

Two long chains are generated using the standard MCMC random-walk perturbation sampler. Convergence and stationarity is assessed by comparing statistical estimates within and across the two chains. The posterior generated by this standard method is used as a reference case for the posterior obtained using the multi-level EnKF/one-stage MCMC sampling.

4.3.1 Proposal Density

Proposals are generated by random-walk perturbation. A multivariate random variable $\hat{z}$ is drawn from a Gaussian distribution with a mean of zero and a covariance equal to the prior covariance multiplied by a scaling factor σ^2 **(Eqs. 52 and 53).**

$$m^* = m^k + \hat{z} \tag{52}$$

$$\hat{z} \sim N(0, C_M \sigma^2) \tag{53}$$

After several trial and error iterations to tune the scaling factor to achieve a well-mixed chain, the scaling factor was chosen to be $(0.005)^2$.

4.3.2 Convergence Diagnostics

Fig. 11 shows the objective function values for the two long standard random-walk perturbation chains. For the first chain, the objective function curves continue to decline for the first 150,000 iterations until it appears to settle down. After 150,000 iterations until the end of the chain at around 400,000 iterations, the objective function curves appear to be stationary with values constrained between 20 and 40, approximately. Although the second chain is not as long as the first chain (currently at 60,000 iterations), it does not show signs of convergence. On the contrary, it continues to show a trend suggesting the chain is still in transitionary behavior. **Fig. 12** shows a comparison of the objective function values for the two chains using box plots. The plot also illustrates that the second chain has higher values of the posterior and appears to be in a transient phase. Because the second chain has not been run long enough—at least not as long as the first chain, no conclusion about the stationarity of the first chain can be drawn at this point.

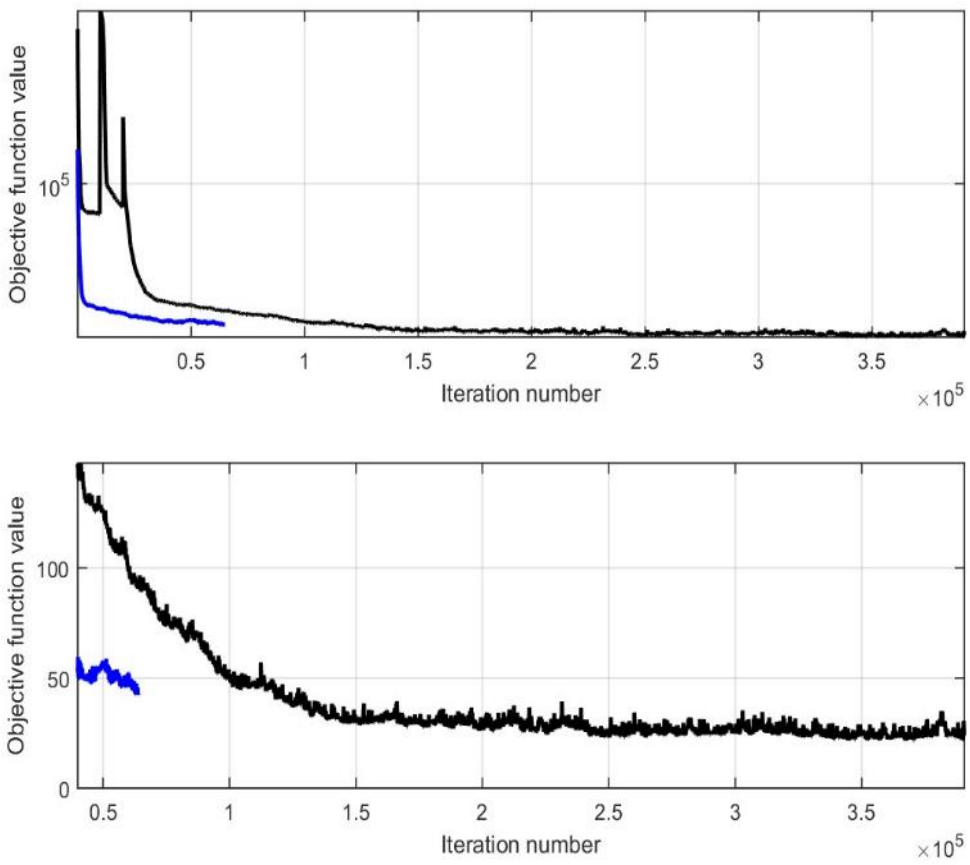

Fig. 11—Posterior objective function values for the two standard random-walk perturbation chains, chain 1 (black) and chain 2 (yellow), of the test problem, all iterations (top) and excluding burn-in iterations (bottom).

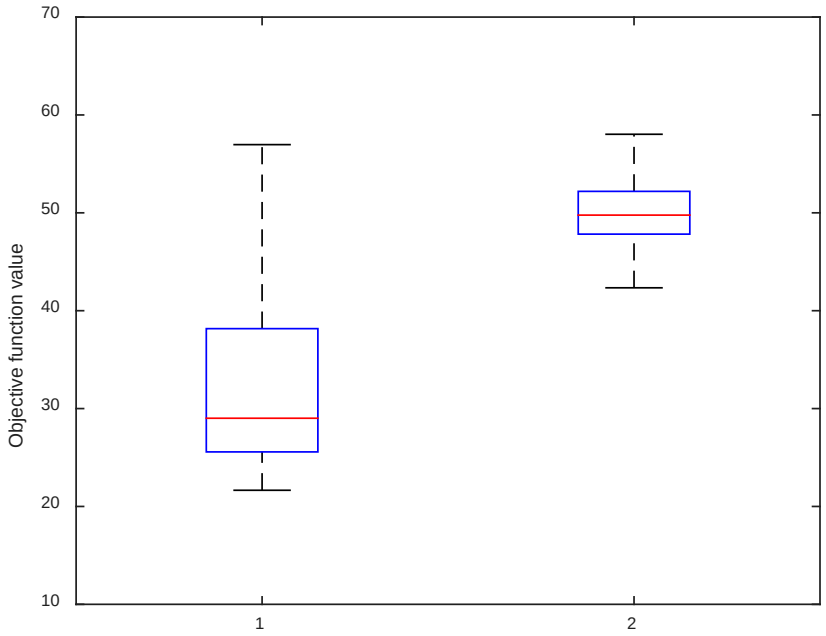

Fig. 12—Box plot for the objective function values of the two long standard random-walk perturbation chains for the test problem showing the 50th percentile (red line), 25th and 75th percentiles (blue box), the minimum and maximum (black lines).

Later, these results will be compared to the multi-level case and more discussion about stationarity and chain mixing will be provided.

4.3.3 Posterior Results

Fig. 13 shows posterior samples of the permeability fields, sampled using the standard random-walk perturbation algorithm. The results of both chains do not seem to bracket the true solution, which might be an indication of poor mixing, or that the chain has not yet converged. **Fig. 14** shows the mean log-permeability values for the two chains including uncertainty bars—each uncertainty bar has a length of two standard deviations.

Although the means and standard deviations of two chains do not appear to be similar, more iterations should be added to the second chain to draw meaningful conclusions with regard to this plot.

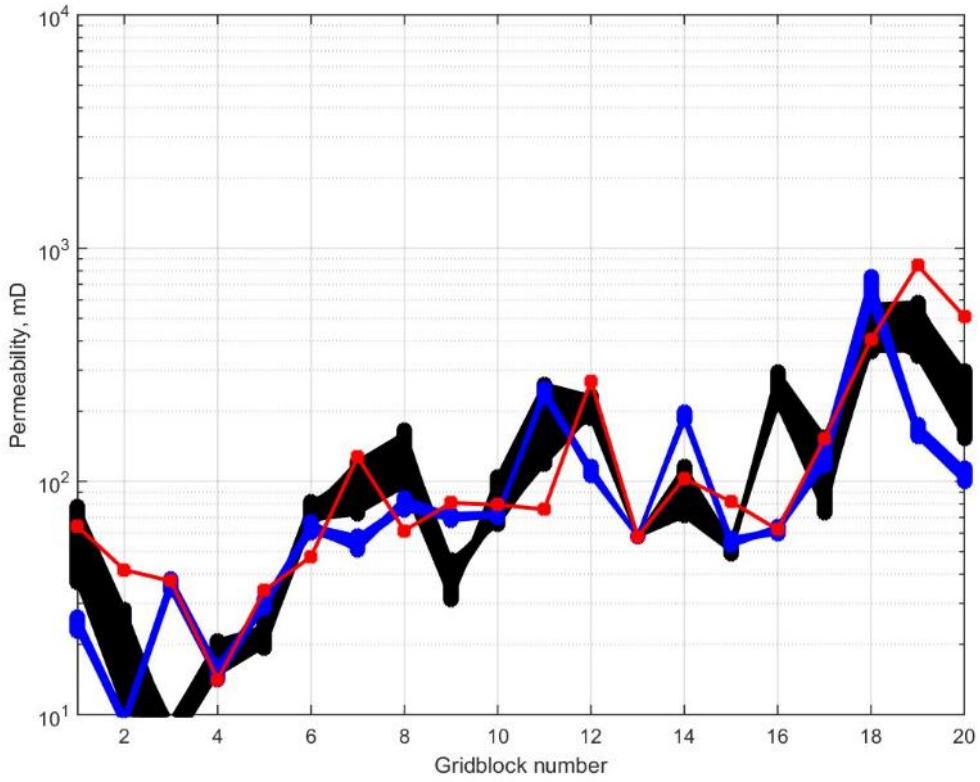

Fig. 13—Permeability fields for the test problem sampled using the standard MCMC random-walk perturbation algorithm: chain 1 (black), chain 2 (blue) and true permeability field (red).

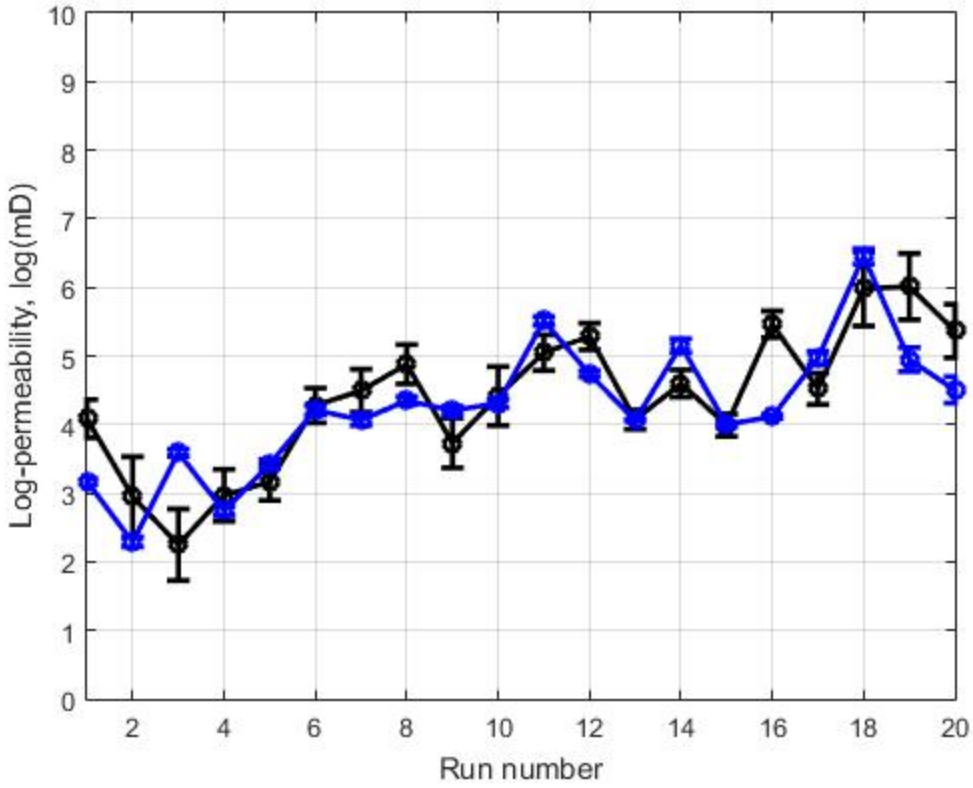

Fig. 14—Mean realization of the log-permeability field for the test problem using the standard MCMC random-walk perturbation algorithm including uncertainty bars: chain 1 (black) and chain 2 (blue).

4.4 Multi-Level EnKF/One-Stage MCMC Case

The posterior covariance generated by EnKF updating, including only the log-permeability parameters, is used in the proposal selection at the MCMC level. The posterior distribution generated by this method is compared to the posteriors obtained through the standard random-walk perturbation method. Assessment of the accuracy of this sampling method and improvement in efficiency is provided.

4.4.1 Proposal Density

The covariance of the log-permeability realizations for the EnKF updated ensemble after the sixth assimilation cycle is calculated, $C_{M,EnKF}$. Proposals at the MCMC chain are generated by adding a random variable $\hat{\beta}$ drawn from a Gaussian distribution with a zero mean and a covariance equal to $C_{M,EnKF}$ multiplied by the same scaling factor σ^2.

$$m^* = m^k + \hat{\beta} \tag{54}$$

$$\hat{\beta} \sim N\left(0, C_{M,EnKF}\,\sigma^2\right) \tag{55}$$

4.4.2 Comparison to Standard Random-Walk Case

Fig. 15 shows a comparison of the posterior objective function values for the multi-level case with values for the standard random-walk perturbation case. The plot shows that using the multi-level case improves the posterior objective function value of the first guess, from a value with a magnitude of 10^7 or higher in the case of standard random-walk perturbation to a value with a magnitude of 10^4 in the multi-level case. Furthermore, Fig. 15Fig. 15 shows a much faster convergence rate for the multi-level case, when compared to the standard random-walk perturbation case. While it took more than 100,000 iterations for the standard random-walk perturbation case to reach an objective function value of 30, it took less than 5,000 iterations for the multi-level case to converge to values even less than that (around 20). Even after running the standard case for over 350,000 iterations, the objective function values were not as low as those achieved after only 5,000 iterations using the multi-level. This suggests that using EnKF updated realization to guide the

proposal selection in MCMC leads to better selection of the initial guess, faster convergence rate, and a smaller burn-in size.

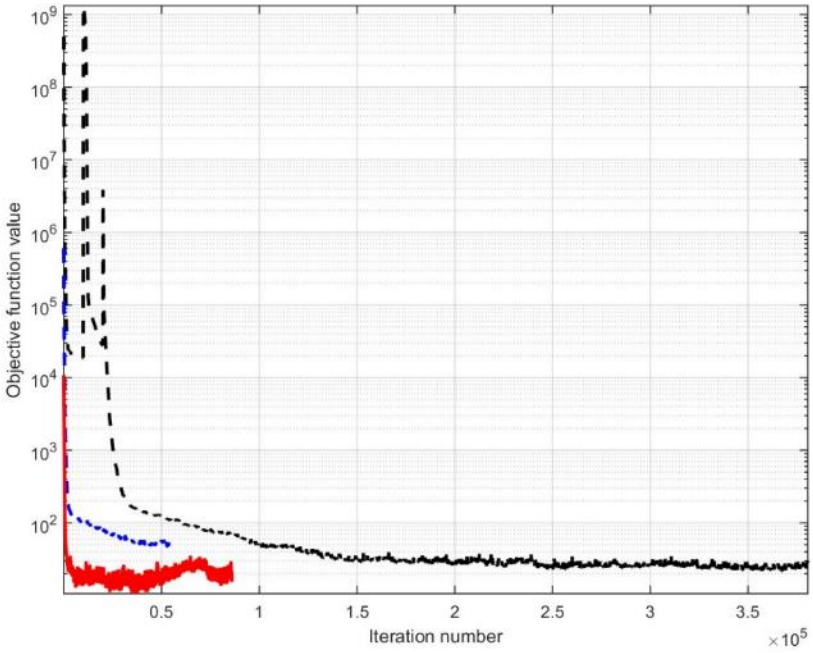

Fig. 15—Posterior objective function value comparison between the two standard random-walk perturbation chains (dashed black and blue curves) and MCMC with EnKF based proposal (solid red).

Fig. 16 shows a comparison between the objective function values for the two standard random-walk perturbation runs after eliminating the first 40,000 iterations, and a multi-level run after eliminating the first 5,000 iterations. Even with a much smaller number of iterations, the multi-level case reaches objective function values lower than those obtained by the standard random-walk perturbation case. This suggests that using the multi-level approach could significantly improve chain mixing and speed up convergence. It also shows that, even for a relatively small problem, the standard case

requires a significantly larger number of iterations to transition to the posterior distribution. In fact, Liu and Oliver (2003) showed that for a similar engineering problem, it would require over a million iterations to be able to estimate the posterior reliably.

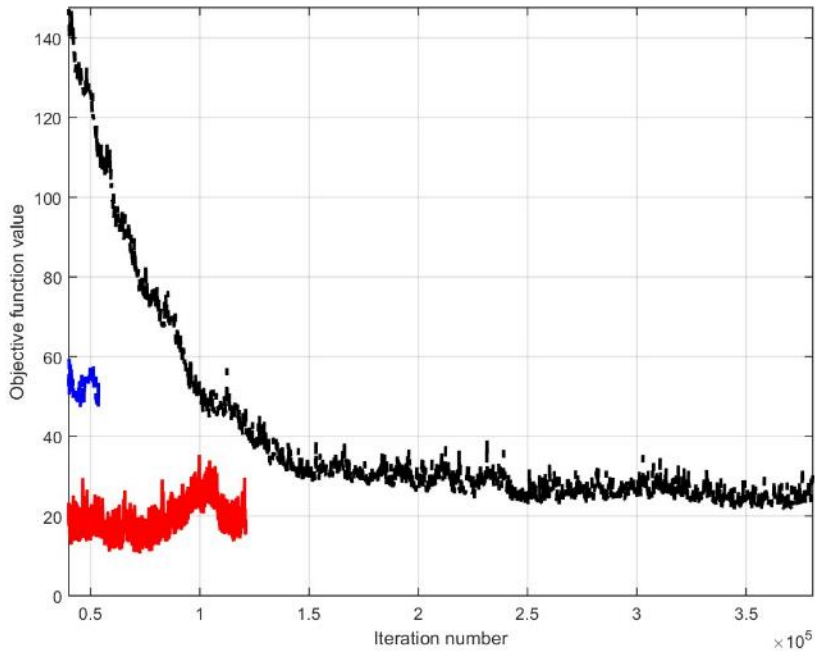

Fig. 16—Comparing the last 100 thousand iterations of the posterior objective function values for the two standard random-walk perturbation chains to the last 50 thousand iterations of the MCMC with EnKF based proposal.

Fig. 17 shows a box-plot comparison for the objective function values for the two standard random-walk perturbation chains and a multi-level chain. The multi-level case generated a chain where the majority of the objective function values are lower than both standard random-walk perturbation cases. These plots reiterate the above conclusions and show that the sampling obtained by the standard case, even with substantially larger

sample size, is of lower quality (i.e., sampling from regions with higher values of the posterior objective function which corresponds to lower posterior probability) than sampling obtained by the multi-level case.

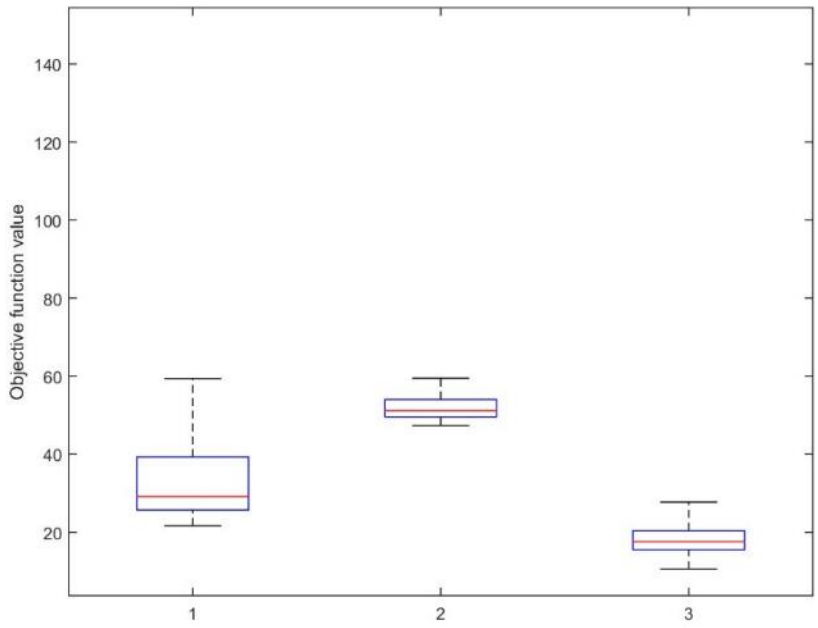

Fig. 17—Box plot comparison for the objective function values of the two standard random-walk perturbation chains (1 and 2) and the multi-level chain (3) after eliminating burn-in iterations showing the 50^{th} percentile (red lines), 25^{th} and 75^{th} percentiles (blue box), the minimum and maximum (black lines).

Fig. 18 compares the acceptance ratio curves (the cumulative sum of accepted iterations divided by the number of iterations) for two standard random-walk perturbation chains and a multi-level chain. The multi-level chain shows an improvement in the acceptance

ratio to a more desirable value of approximately 0.25, suggesting improvement in chain mixing and sampling efficiency.

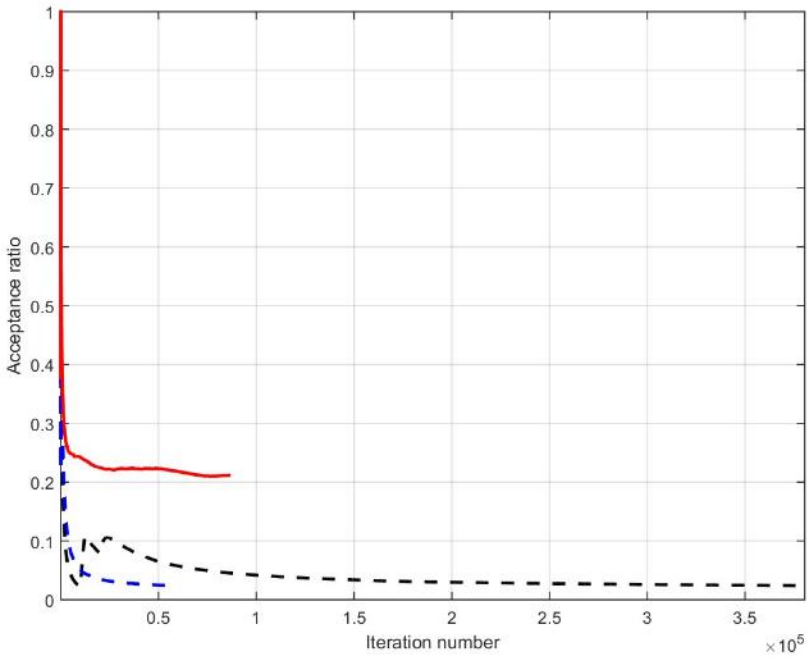

Fig. 18—Comparison of the acceptance ratio curves for the two standard random-walk perturbation chains (dashed black and dashed blue) and the multi-level chain (solid red).

4.4.3 Posterior Results

Fig. 19 shows the posterior permeability realizations sampled using the two standard random-walk perturbation chains and the multi-level chain. The multi-level case, in contrast to the standard case (Fig. 13), brackets the true solution. Also, when compared to the EnKF cases (Fig. 8), the multi-level case shows reduction in the uncertainty of the permeability field (i.e., the realizations have less spread), as well as improved values of

the posterior objective function (Fig. 18). This is indicative of better sampling of the posterior distribution.

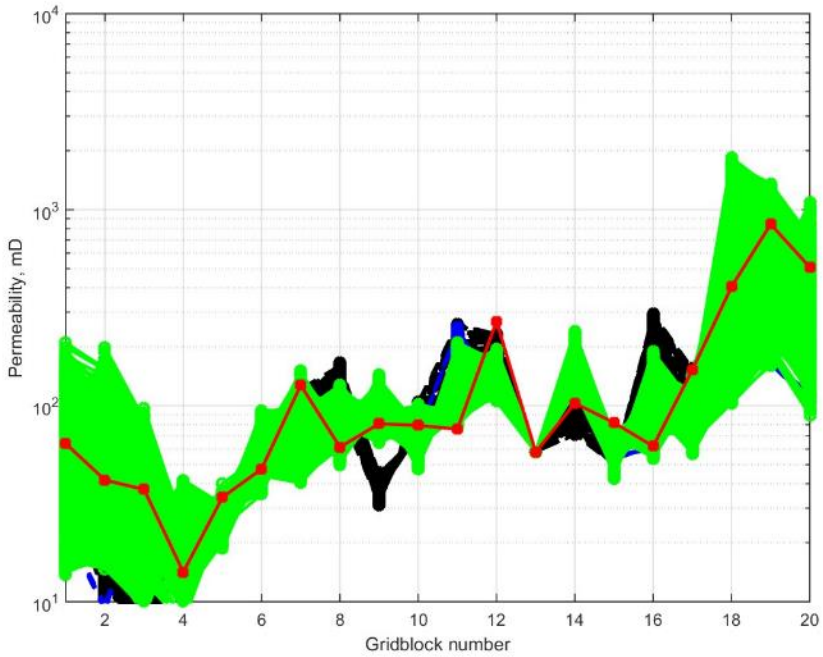

Fig. 19—Comparing the posterior permeability realizations sampled using the two standard random-walk perturbation chains (black and blue), the multi-level chain (green), and the true permeability field (red).

5. MULTI-LEVEL CONTINUOUS MODEL UPDATING AND UNCERTAINTY QUANTIFICATION USING ENKF/TWO-STAGE MCMC: 2-D CHANNELIZED RESERVOIR WATER FLOODING PROBLEM

In this section, the continuous multi-level model updating and uncertainty quantification algorithm (Sec. 3.2) is applied in a 2-D synthetic channelized-reservoir water-flooding experiment. Results obtained by the proposed algorithm are compared to results of EnKF, the standard random-walk perturbation algorithm, and multi-level cases using EnKF/one-stage MCMC. Estimates of the posterior permeability field generated by these methods are compared and analyzed, in reference to the true permeability field. Also, uncertainty quantification of the forecasted production is provided and assessed. Additionally, convergence, chain mixing and efficiency improvement in the proposed method are discussed.

The following subsections present the reservoir model, initial ensemble, the true synthetic realization, observed measurements and the parameterization used in this work. Then, EnKF results are provided. This is followed by presenting the results and analysis of the continuous multi-level approach using one-stage and two-stage MCMC.

5.1 Simulation Model Description

The reservoir simulation model used in this section was originally developed by Brouwer et al. (2004), and later studied by Sarma et al. (2005) and Jafarpour and McLaughlin (2009b). The 2-D model is discretized into a 45-by-45 Cartesian grid. Each

gridblock is 35×35×35 ft^3. The initial reservoir pressure is 3000 psi, and the initial water saturation is 0.1. The porosity is 0.2 and is homogeneous. The rock compressibility is 3×10^{-6} psi^{-1}. The flow is two-phase with both oil and water viscosities of 1 cp. Fluid densities are 45 and 63 lb/cu-ft for oil and water, respectively. Capillary forces are neglected. The relative permeability data are provided below **(Fig. 20).**

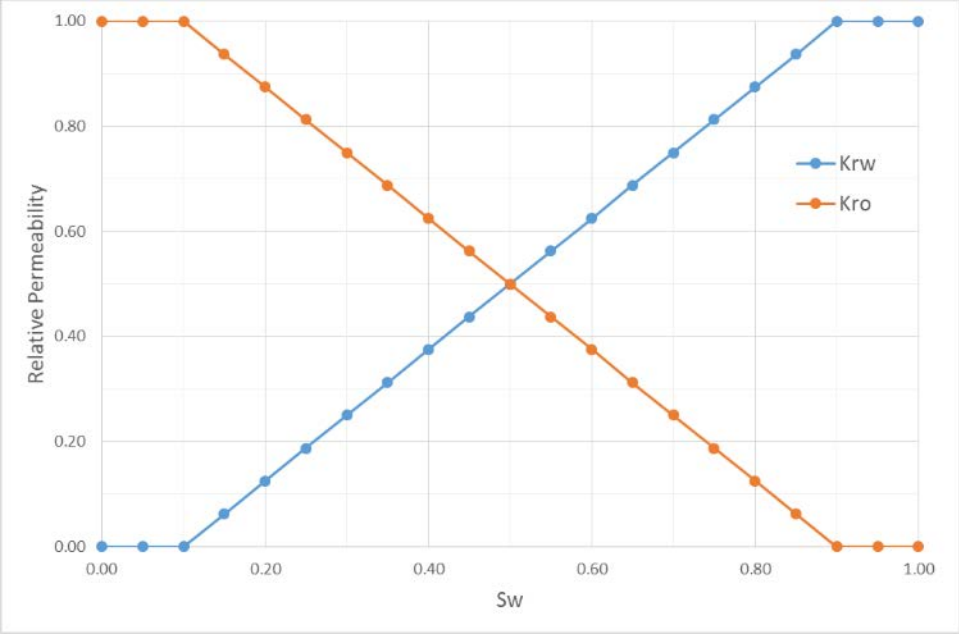

Fig. 20—Relative permeability data showing water relative permeability (blue) and oil relative permeability (brown).

Two horizontal wells, each with 45 well ports, are modeled. Each well is divided into three groups of 15 well ports. The injector well is located at the left side of the reservoir while the producer is located at the right side of the reservoir. The total simulation time is 1080 days. Time is discretized into 12 intervals of 90 days. A total of

one pore volume (PV) is injected into the reservoir during the simulation. The production is controlled by a BHP specified for each of the producer's well ports.

Each group of well ports shares the same BHP control **(Table 1).** The injection is controlled by a target rate specified for each of the injector's well ports. In each time interval, one-twelfth PV is injected. The injection volume is allocated among the three groups of the injector well. The rate allocated for each group is divided equally among the 15 well ports of that specific group **(Table 2).**

Table 1—BHP controls for the well ports of the producer well.

Time (days)	Group 1 BHP (psi)	Group 2 BHP (psi)	Group 3 BHP (psi)
0 – 90	2990	2990	2990
90 – 180	2990	2990	2990
180 – 270	2990	3000	2990
270 – 360	2990	3000	2990
360 – 450	2990	3000	2990
450 – 540	2990	3000	2990
540 – 630	3000	2990	3000
630 – 720	3000	2990	3000
720 – 810	2990	2990	2990
810 – 900	2990	2990	2990
900 – 990	3000	2990	3000
990 – 1080	3000	2990	3000

Table 2—Injection rate control for the well ports of the injector well.

Time (days)	Group 1 (bpd)	Group 2 (bpd)	Group 3 (bpd)
0 – 90	942	942	942
90 – 180	942	942	942
180 – 270	1414	0	1414
270 – 360	1414	0	1414
360 – 450	0	2827	0
450 – 540	0	2827	0
540 – 630	1414	0	1414
630 – 720	1414	0	1414
720 – 810	942	942	942
810 – 900	942	942	942
900 – 990	0	2827	0
990 – 1080	0	2827	0

5.2 Initial Ensemble

The initial ensemble is created following the procedure by Jafarpour and McLaughlin (2009b). A training image **(Fig. 21)** is used to generate channelized reservoir realizations. Single Normal Equation (SNESIM) algorithm (Strebelle 2002; Strebelle and Journel 2001) in the SGeMS® package is used to generate 300 permeability fields. Two facies are modeled: channel (10,000 mD) and non-channel (500 mD) with a target marginal distribution of 30% for channel and 70% for the non-channel categories. Three multigrid template levels are used in the sequential simulation process (Strebelle 2002) to generate the initial ensemble. **Fig. 22** shows examples of the realizations of the initial ensemble.

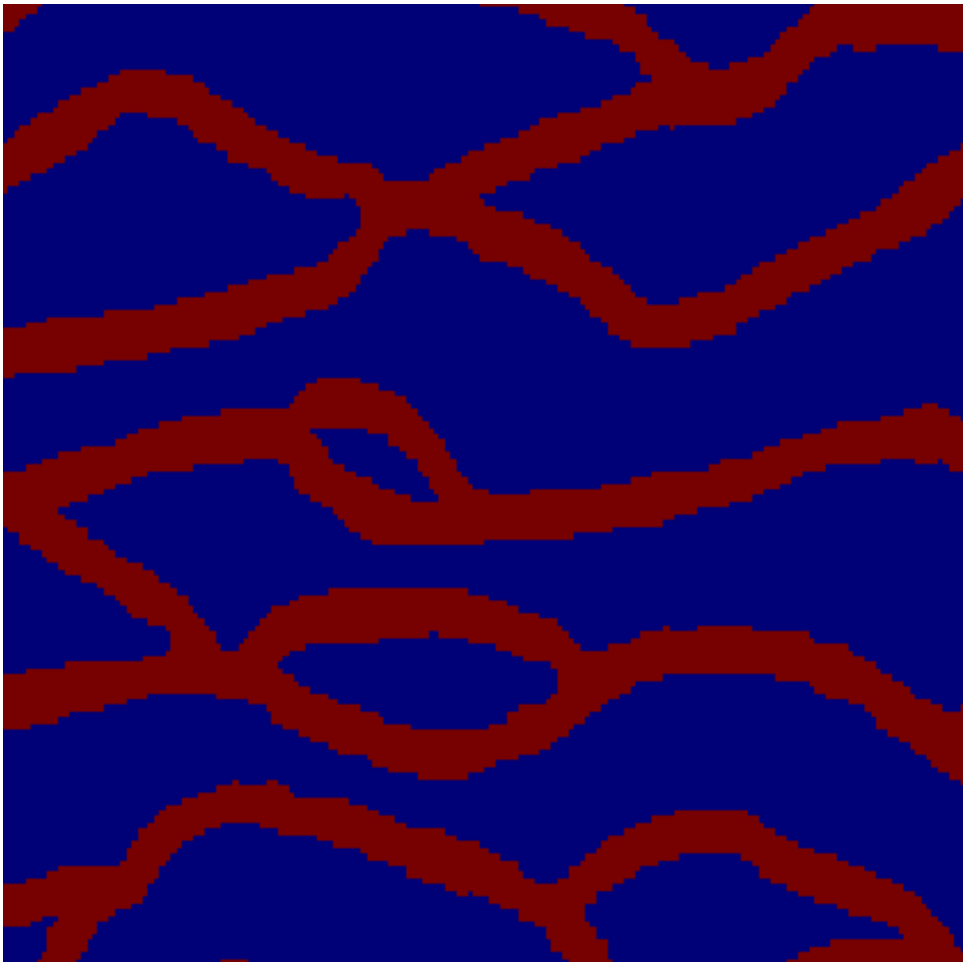

Fig. 21—Training image for the channelized reservoir description: channel (red) and non-channel (blue).

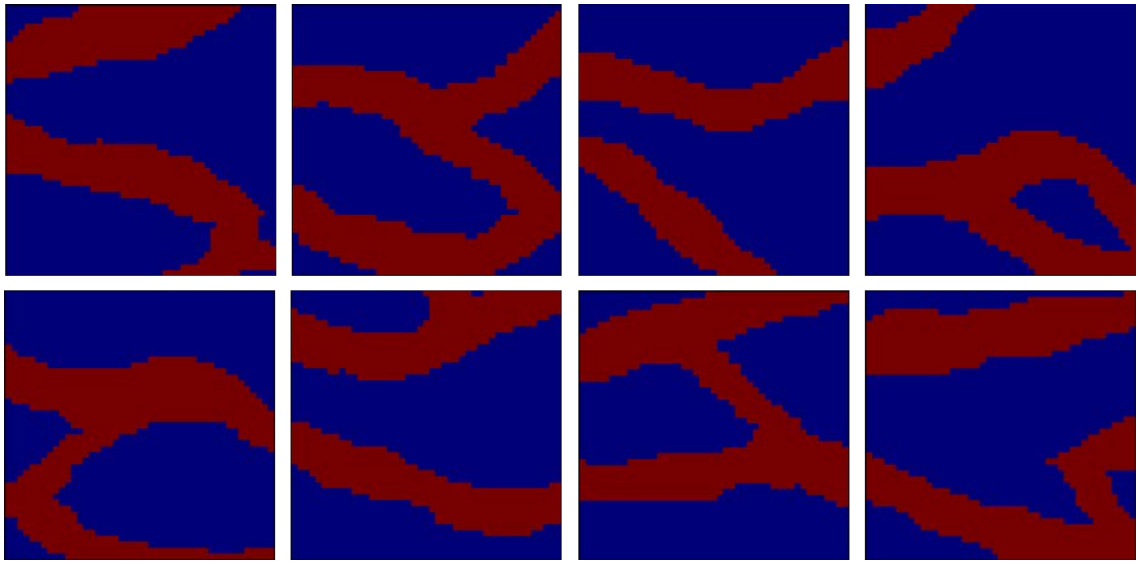

Fig. 22—Example members of the initial ensemble: channel (red) and non-channel (blue).

5.3 True Synthetic Realization and Observed Measurements

A true synthetic permeability field **(Fig. 23)** is used to generate observed injector well-portal BHPs and producer well-portal rate measurements. The true synthetic permeability field is composed of approximately 60% non-channel facies and 40% channel facies. The true synthetic reservoir performance is shown in **Fig. 24 and 25** and compared to the reservoir performance of all the members of the initial ensemble.

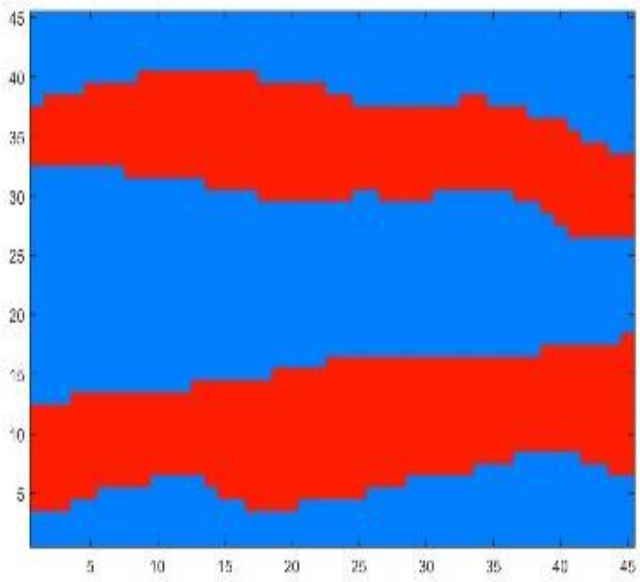

Fig. 23—True synthetic permeability field showing channel (red) and non-channel (blue) features.

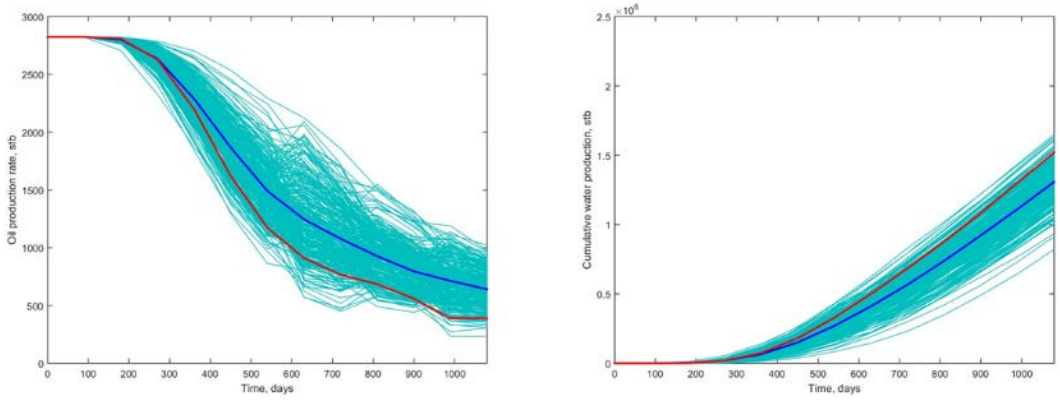

Fig. 24—Oil production rate (left) and cumulative oil production (right) profiles for the true synthetic case (red), initial ensemble members (cyan) and the average of the initial ensemble member profiles (blue).

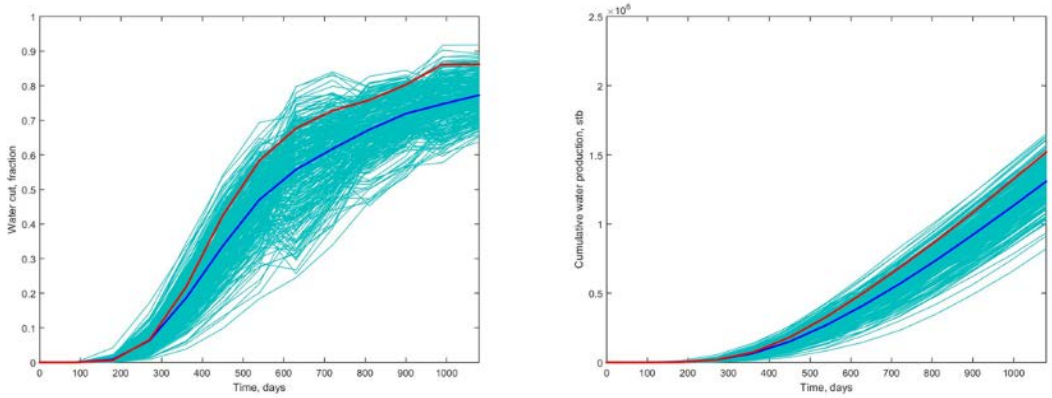

Fig. 25—Producer water cut (left) and cumulative water production (right) profiles for the true synthetic case (red), initial ensemble members (cyan) and the average of the initial ensemble member profiles (blue).

At the end of each of the 12 time steps corresponding to the assimilation cycles, 135 true well-portal measurements are generated: 45 portal BHP at the injector well, 45 portal oil production rate and 45 portal water production rate at the producer well. The total number of measurements is 1620. An ensemble (300 realizations) of observed measurements are generated by randomly adding Gaussian noise to true well portal production rates with a standard deviation of 20 bpd and true well portal BHP with a standard deviation of 20 psi. The covariance, $\overline{C_d}$, estimated from these measurement realizations are used in the EnKF experiment (Eq. 34).

5.4 Parameterization

2-D DCT algorithm (Jain 1989) is used to parameterize the log-permeability, pressure and water saturation fields. Using this parameterization, each of the log-

permeability, pressure and water saturation vectors is reduced from a length of 2025 (45×45) to a length of 100 (10×10) **(Eq. 56).**

$$\alpha_{k_1,k_2} = c_{k_1} c_{k_2} \sum_{n_1=0}^{N_1-1} \sum_{n_2=0}^{N_2-1} m_{n_1,n_2} \cos\frac{\pi(2n_1+1)k_1}{2N_1} \cos\frac{\pi(2n_2+1)k_2}{2N_2} \quad (56)$$

In the equation above, α_{k_1,k_2} is the reduced parameter corresponding to the k_1 row and the k_2 column in the reduced domain, m_{n_1,n_2} is the parameter corresponding to n_1 row and n_2 column in the original domain, N_1 and N_2 are the number of rows and columns in the original domain, and c_{k_1} and c_{k_2} are coefficients calculated using **Eqs. 57 and 58.**

$$c_{k_1} = \begin{cases} \frac{1}{\sqrt{N_1}} & , k_1 = 0 \\ \frac{\sqrt{2}}{\sqrt{N_1}} & , 1 \le k_1 < N_1 - 1 \end{cases} \quad (57)$$

$$c_{k_2} = \begin{cases} \frac{1}{\sqrt{N_2}} & , k_2 = 0 \\ \frac{\sqrt{2}}{\sqrt{N_2}} & , 1 \le k_2 < N_2 - 1 \end{cases} \quad (58)$$

The reduced parameterization of the log-permeability field is used in all EnKF/MCMC applications, while the reduced parameterization of the pressure and water saturation fields are used only in the update step of the EnKF algorithm and in the first MCMC stage of the multi-level EnKF/two-stage MCMC sampling. The inverse transformation from the reduced to the original domain can be calculated using **Eq. 59.**

$$m_{n_1,n_2} = \sum_{k_1=0}^{N_1-1} \sum_{k_2=0}^{N_2-1} c_{k_1} c_{k_2} \alpha_{k_1,k_2} \cos\frac{\pi(2n_1+1)k_1}{2N_1} \cos\frac{\pi(2n_2+1)k_2}{2N_2} \quad (59)$$

To ensure the update step in EnKF does not result in non-physical water saturation values (i.e., smaller than zero or more than one), the inverse of the error function is used to transform the water saturation field before it is parameterized using 2-D DCT. The transformation and inverse transformation are given by **Eqs. 60 and 61.**

$$S_w^* = \text{erf}^{-1}(2S_w - 1) \tag{60}$$

$$S_w = \frac{1}{2}\,\text{erf}\,(S_w^* + 1) \tag{61}$$

5.5 EnKF

Two EnKF experiments were conducted: one with 2-D DCT parameterization and one without any parameterization. In the case with 2-D DCT parameterization, the augmented parameter-state vector, y_t, at each time step has a length of 435: 100 reduced parameters for the log-permeability field, 100 reduced parameters for the pressure field, 100 reduced parameters for the water saturation field, and 135 predicted well measurements. The forecast covariance matrix, $\overline{C_{y_t}^f}$, has a size of 435 by 435. In the case with no parameterization, the augmented parameter-state vector, y_t, at each time step would have a length of 6210: 2025 log-permeability values, 2025 gridblock pressure values, 2025 gridblock water saturation values, and 135 predicted well measurements. The forecast covariance matrix, $\overline{C_{y_t}^f}$, has a size of 6210 by 6210.

In this subsection, EnKF posterior estimates of the log-permeability field for the two experiments are compared and analyzed, in reference to the true log-permeability field. Also, EnKF posterior estimates of the water saturation field are presented and compared with the true water saturation fields. Finally, production forecasts using the parameterized case are provided.

Fig. 26 presents the mean of the EnKF updated log-permeability realizations for the DCT parameterized case and the no-parameterization case. Comparing the results with

the true synthetic permeability show that both cases were capable of capturing the general trend and orientation of the channels as early as the first update. The main geological features continue to get more defined as the models are updated and more observed data are assimilated. It is also noticeable that the means do not significantly change between the 10^{th} update (30 months) and the 12^{th} update (36 months). The estimates generated by the DCT case are smoother than the case with no parameterization. This is a feature of the DCT parameterization. **Fig. 27** shows that the estimated errors (true log-permeability minus the mean estimate) continue to reduce, in general, as the models get updated. Both cases appear to capture the log-permeability values in the mid-channels more accurately, i.e., smaller error estimates. The EnKF posterior estimates for the permeability field is continuous (i.e., in contrast to the discrete, channel and non-channel realizations of the true field and initial ensemble). While the EnKF is capturing the location and the general trend of these channels, the permeability distribution inside the channels are more continuous than the true case. This explains how the mean error estimates inside the channels are the lowest in the middle, positive from the middle outward (i.e., EnKF estimates are underestimating the permeability values) and negative around the edges of the channels (i.e., the EnKF overestimating the permeability values). The estimates generated by the parameterized case are found to be slightly less accurate than estimates generated with no parameterization, especially at later updates. This could be due to the smoothing effect DCT imposes on the log-permeability field.

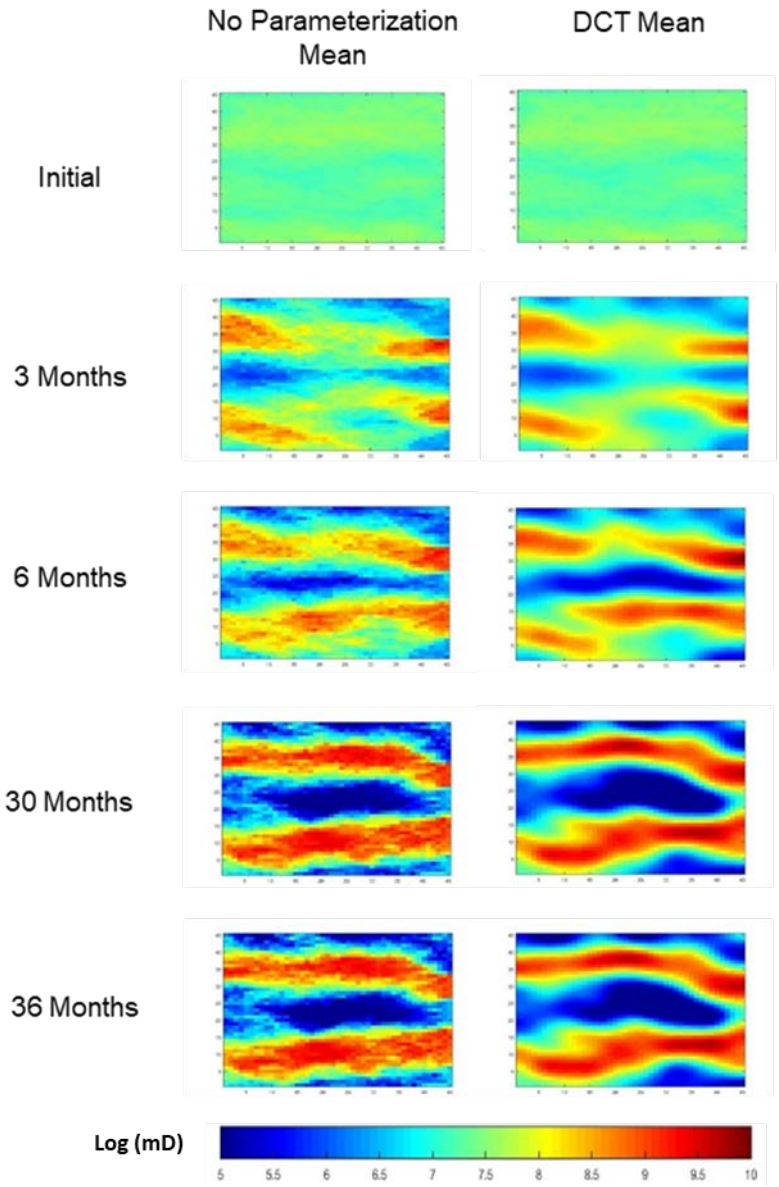

Fig. 26—Log-permeability fields for the ensemble mean of EnKF no-parametrization case (left column) and DCT parameterization case (right column) for the initial ensemble (1st row), at the end of the 1st assimilation cycle (2nd row), 2nd assimilation cycle (3rd row), 10th assimilation cycle (4th row) and 12th assimilation cycle (5th row).

Fig. 28 presents standard deviation maps for log-permeability fields of the EnKF realizations. Clearly, as model updating progresses, the uncertainty (i.e., standard deviation) continues to reduce. It is worth noting that uncertainty reduces first around the wells and continues to diminish along the flow paths. This is because at earlier times, the log-permeability values of the gridblocks closer to the wells are more correlated with observed measurements than other areas of the reservoir. Then, as time progresses, the correlation seems to follow the orientation of the flow paths in the reservoir. The maps also show that there is no noticeable uncertainty reduction between the last two assimilation cycles.

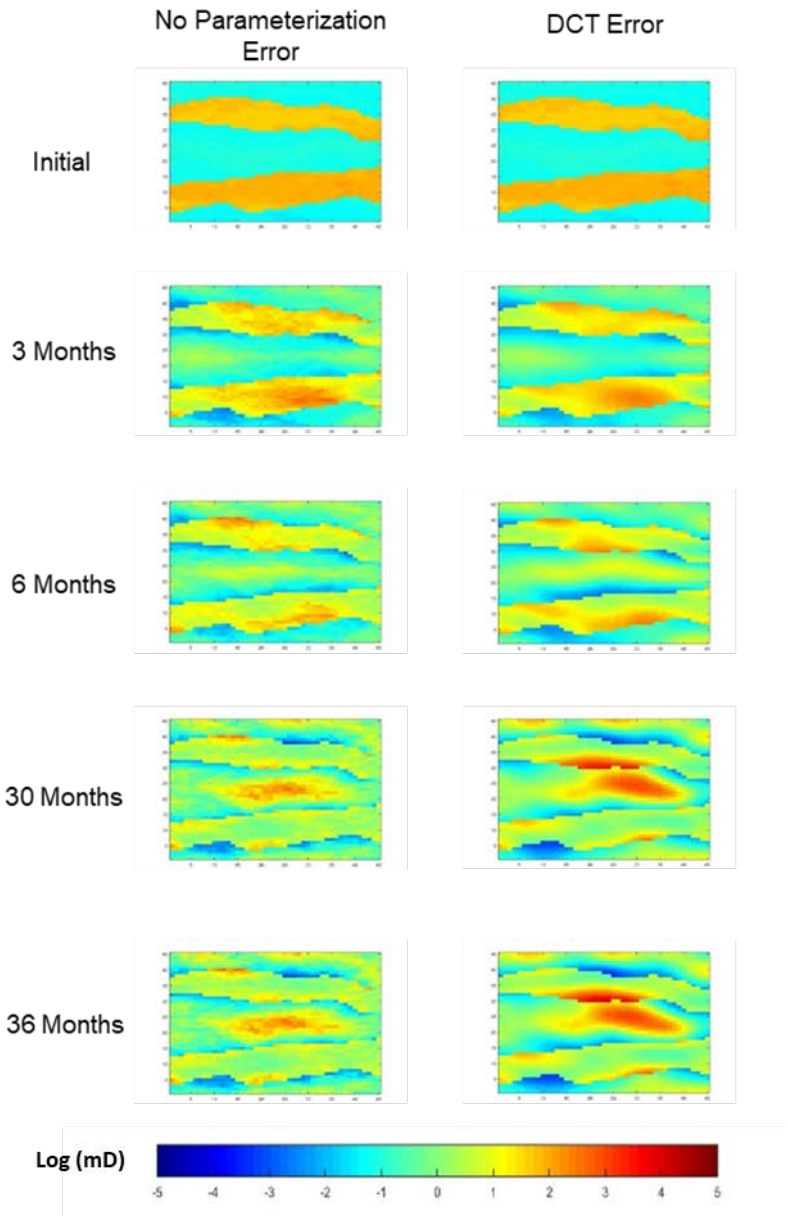

Fig. 27—The mean error estimate of the log-permeability fields for EnKF no-parameterization case (left column) and DCT parameterization case (right column) for the initial ensemble (1st row), at the end of the 1st assimilation cycle (2nd row), 2nd assimilation cycle (3rd row), 10th assimilation cycle (4th row) and 12th assimilation cycle (5th row).

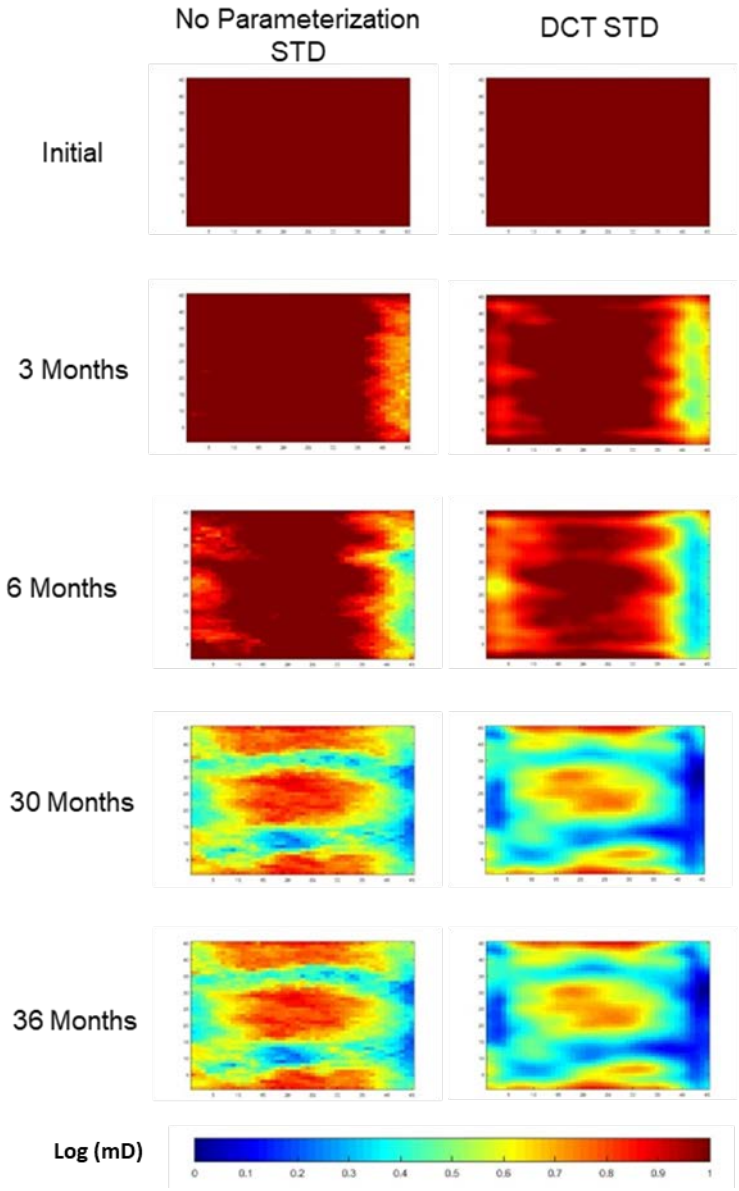

Fig. 28—Standard deviation of log-permeability fields of the EnKF realizations with no parameterization (left column) and with DCT parameterization (right column) for the initial ensemble (1st row), at the end of the 1st assimilation cycle (2nd row), 2nd assimilation cycle (3rd row), 10th assimilation cycle (4th row) and 12th assimilation cycle (5th row).

Fig. 29 compares the true oil saturation maps to the ensemble mean of both the no-parameterization case and the DCT case. The maps show that both cases can capture the overall flow patterns, channel locations and orientations. The EnKF mean estimates are smoother (i.e., no sharp edge features) than the true case. This is a result of averaging of many saturation field realizations.

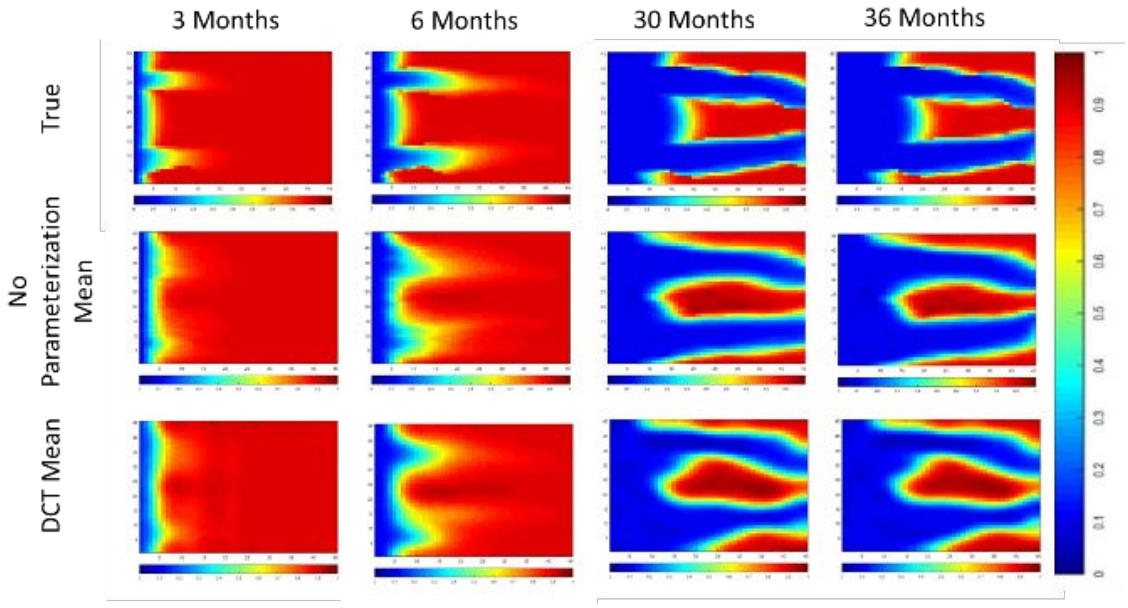

Fig. 29—Oil saturation maps for the true realization (top row), mean of the no-parameterization ensemble (middle row) and mean of the DCT ensemble (bottom row) at the end of the 1st assimilation cycle (1st column), 2nd assimilation cycle (2nd column), 10th assimilation cycle (3rd column) and 12th assimilation cycle (4th column).

Fig. 30–32 compare the ensemble of production forecasts obtained through EnKF without parameterization to the ones obtained by running the initial ensemble without model updating (open loop). The plots show that EnKF updating narrows the range of forecasts significantly and drives the distribution close to the truth case.

Fig. 33 shows the changes in the log-permeability fields as models continue to be updated through EnKF without parameterization. The plots show that log-permeability fields begin to change at the first update. Over time, the vertical patterns begin to break down, which more accurately models the overall flow patterns. Finally, all cases capture the two main horizontal channels connecting the injector and the producer. The differences between the final realizations seem to be in the width of channels, and the variation of log-permeability values within the channels and in the no-channel areas.

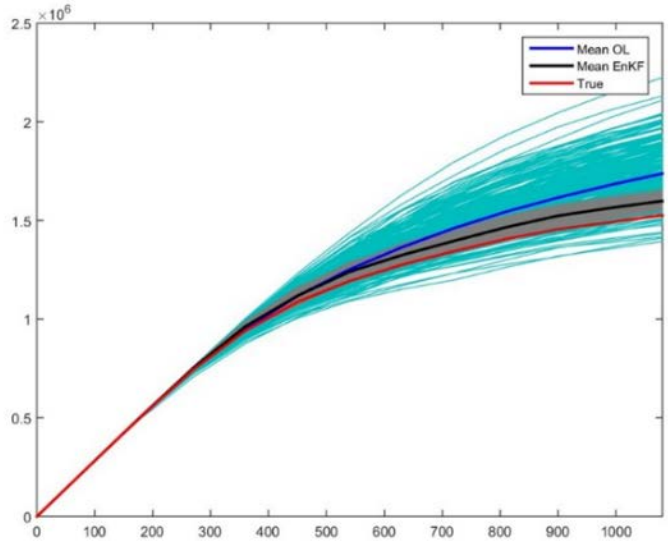

Fig. 30—Cumulative oil production showing open loop runs (cyan), the mean of open loop runs (blue), updated EnKF realizations (grey), the mean of EnKF realizations (black) and the truth case (red).

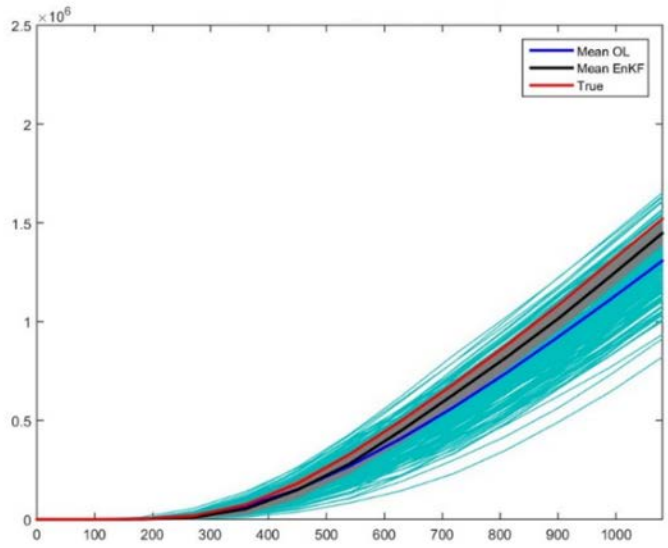

Fig. 31—Cumulative water production showing open loop runs (cyan), the mean of open loop runs (blue), updated EnKF realizations (grey), the mean of EnKF realizations (black) and the truth case (red).

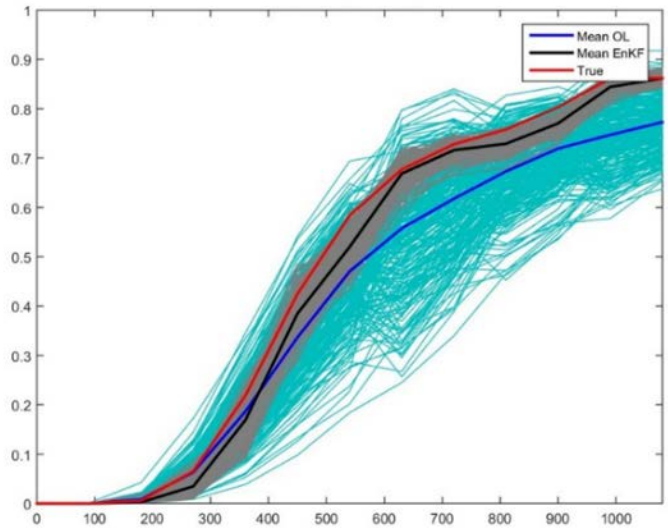

Fig. 32—Water cut showing open loop runs (cyan), the mean of open loop runs (blue), updated EnKF realizations (grey), the mean of EnKF realizations (black) and the truth case (red).

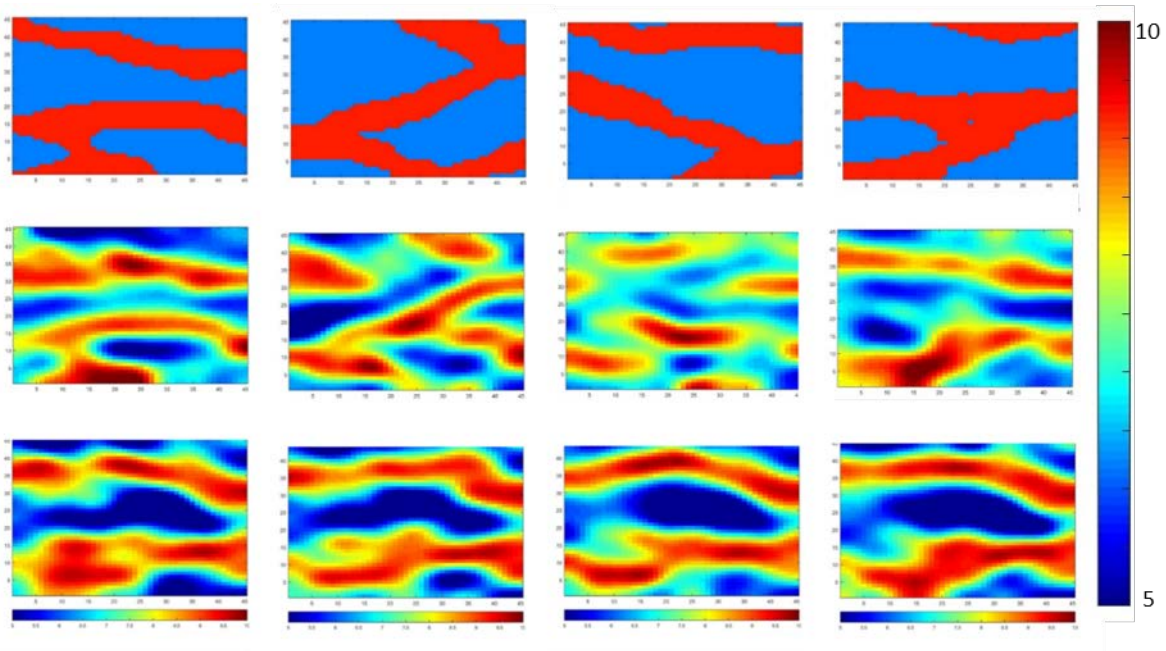

Fig. 33—Log-permeability fields (log-mD) for four members of the EnKF showing initial ensemble realizations (top row), realizations after the 1st update (middle row) and realizations after the last update (bottom row).

5.6 Continuous Multi-Level Cases Using EnKF/One-Stage MCMC

In this subsection, the EnKF posterior covariance of the log-permeability field is used to define the proposal density for MCMC. Four MCMC chains are presented: the first is based on the third update of the EnKF, i.e., conditioned to all observed measurements available at the end of the third assimilation cycle (270 days), the second is based on the sixth update of EnKF, i.e., conditioned to all observed measurements available at the end of the sixth assimilation cycle (540 days), the third is based on the ninth update of the EnKF, i.e., conditioned to all observed measurements available at the end of the sixth assimilation cycle (810 days), and the fourth is based on the twelfth update

of the EnKF, i.e., conditioned to all observed measurements available at the end of the sixth assimilation cycle (1080 days). Each chain of MCMC consists of 500 iterations. In all these chains, the covariance of the proposal distribution is estimated from the updated EnKF realizations. ECLIPSE® is used to run the proposed realizations. The likelihood function is evaluated exactly using reservoir simulation output.

These chains are generated to be compared to the multi-level EnKF/two-stage MCMC results in the following section. Acceptance ratio curves and objective function values generated using this method (i.e., using exact likelihood function evaluation) will form a basis for evaluating the efficiency and sampling validity for the EnKF/two-stage MCMC method.

Additionally, a comparison between a chain generated by the multi-level/one-stage MCMC method and standard random-walk perturbation method is presented. This comparison demonstrates the improvements in efficiency and sampling quality, if any, resulting from using the EnKF posterior covariance to form the proposal density of MCMC.

Posterior estimates of the log-permeability field for the four chains are presented and discussed. Convergence diagnostics such as acceptance ratio and objective function curves are presented and compared to the standard random-walk perturbation case. Additionally, the forecasted reservoir performance resulting from this experiment is shown and compared to both open-loop (i.e., running the prior realizations without conditioning on observed measurements) and EnKF cases.

5.6.1 Posterior Results at 270 Days

Fig. 34 presents the mean, mean error (true realization minus the mean estimate), and standard deviation estimates for the log-permeability field of the initial ensemble, the ensemble obtained at the end of EnKF third assimilation cycle (9 months) and the posterior samples obtained by MCMC with a proposal based on EnKF log-permeability posterior covariance. It also shows the true synthetic saturation field, the saturation field obtained by running a reservoir simulation for the mean EnKF realization, and the saturation field of the mean one-stage MCMC case, at 270 days. The mean and mean error estimates of both the EnKF and the one-stage MCMC cases show improvement in capturing the trend and the orientation of the main two channels in the field, when compared to the initial ensemble. The mean error estimates show that both the EnKF and the one-stage MCMC log-permeability estimates are, generally, more accurate in the regions close to the wells and least accurate in the unswept regions in the middle of the field. Thus, the log-permeability values in the regions close to the wells and in the swept regions are more resolved by the observed measurement information.

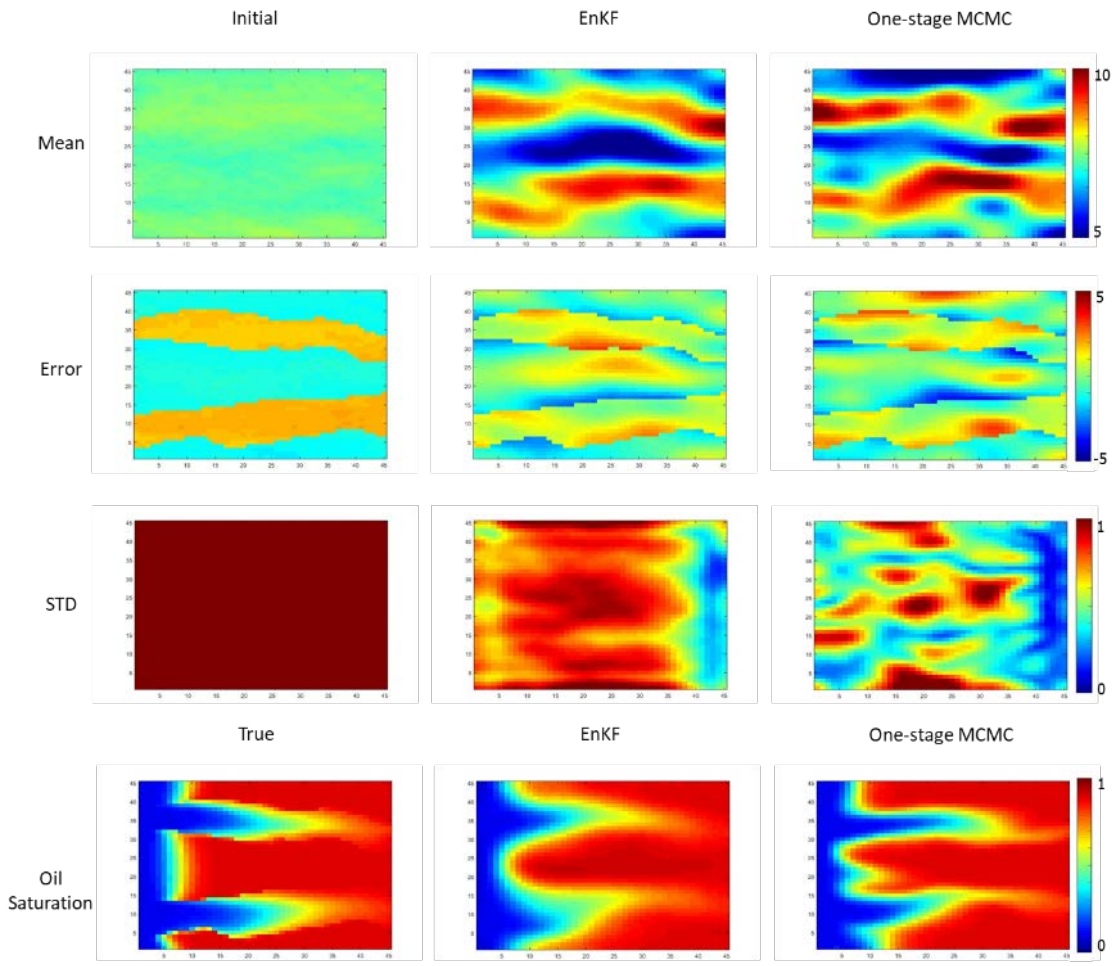

Fig. 34—The log-permeability (log-mD) fields of the mean realization (1st row), the mean error estimates of the log-permeability (log-mD) fields of the mean realization (2nd row) and the standard deviation of the log-permeability (log-mD) field (3rd row) among all realizations of the initial ensemble (1st column), EnKF realizations (2nd column) and the one-stage MCMC realizations (3rd column) after the 3rd update (9 months). Oil saturation maps at 270 days (4th row) for the true realization (1st column), EnKF ensemble mean (2nd column) and the mean of one-stage MCMC (3rd column).

Additionally, the mean error maps show the log-permeability estimates along the middle of the two channels to be more accurate than estimates near the edges of the channels. This is because both methods tend to smooth out the log-permeability values

rather than produce a sharp edge, as in the true log-permeability field. The standard deviation estimates for both cases show significant reduction over the initial ensemble. The standard deviation estimates of the EnKF are the smallest along the producer well (right side). This is because the amount of information obtained from the portals of the producer well is twice the amount of information obtained from the injector wells—90 data points per assimilation cycle for the producer well compared to 45 data points per assimilation cycle for the injector well. The standard deviation estimates closer to the wells and along the channels appear to be smaller than in unswept areas of the reservoir. While the mean and error estimates for both EnKF and one-stage MCMC cases look fairly similar, the standard deviation estimates for the MCMC case are smaller than those of EnKF. This could be due to one of two reasons: (1) the actual variability of the MCMC posterior is less than that of EnKF due to improved sampling, or (2) the variability produced by the MCMC chain is less than actual variability due to convergence or mixing issues. The convergence and mixing of the MCMC chains is discussed in more detail later in this section. The mean oil saturation maps show that both cases are capturing the general trend of the flood paths along the field and approximating the water front reasonably well. Estimates for the mean oil saturation field appear to be smoother than the true oil saturation field. This is due to both the effect of averaging an ensemble of oil saturation maps and the variability of log-permeability values within the channels for the EnKF and the one-stage MCMC cases.

5.6.2 Posterior Results at 540 Days

Fig. 35 compares the mean, error, standard deviation estimates and oil saturation maps at the end on ninth assimilation cycle (18 months). The mean estimate maps for both cases show the two channels to be more connected than the results obtained at 270 days. In general, the mean error estimates have improved, when compared to previous estimates. The MCMC error estimates are slightly better than the EnKF estimates, especially inside the channels. The standard deviation estimates show a clear reduction over previous estimates. This is more prominent in the regions adjacent to the two wells and along the two channels, as the flood front continues to advance, and parameter values in these areas become more resolved by the newly observed measurements. The MCMC standard deviation estimates are shown to be significantly less than those for EnKF. The same analysis made previously in this regard applies here as well. The oil saturation maps continue to show that both cases are approximating the flood front and the flow paths quite reasonably.

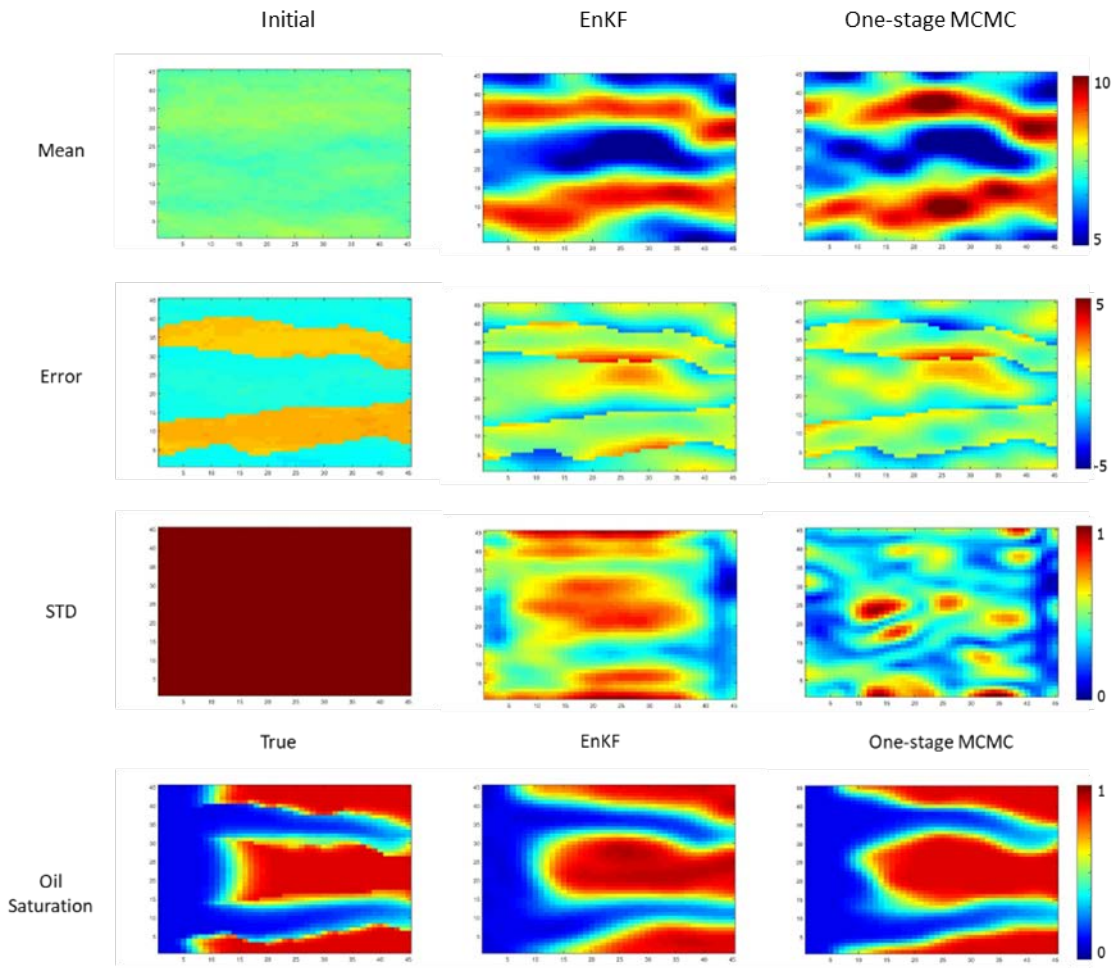

Fig. 35—The log-permeability (log-mD) field of the mean realization (1st row), the mean error estimates of the log-permeability (log-mD) field of the mean realization (2nd row) and the standard deviation of the log-permeability (log-mD) field (3rd row) among all realizations of the initial ensemble (1st column), EnKF realizations (2nd column) and the one-stage MCMC realizations (3rd column) after the 6th update (18 months). Oil saturation maps at 540 days (4th row) for the true realization (1st column), EnKF ensemble mean (2nd column) and the mean of one-stage MCMC (3rd column).

5.6.3 Posterior Results at 810 Days

Fig. 36 compares the mean, error, standard deviation estimates and oil saturation maps at the end of the ninth assimilation cycle (27 months). The mean estimates for both EnKF and one-stage MCMC cases show the channels becoming more defined and continuous. The mean error estimates for both cases are fairly similar to the previous estimates, at 540 days. The standard deviation estimates for both cases are smaller than those obtained previously. Overall, the incremental changes in the estimates over the previous update at 540 days are smaller than the changes that took place between the initial ensembles and the previous estimates, at 270 days and 540 days. Because smaller changes in flow patterns inside the reservoir have occurred since the previous update, the newly observed data contributes less to resolving the uncertain parameters.

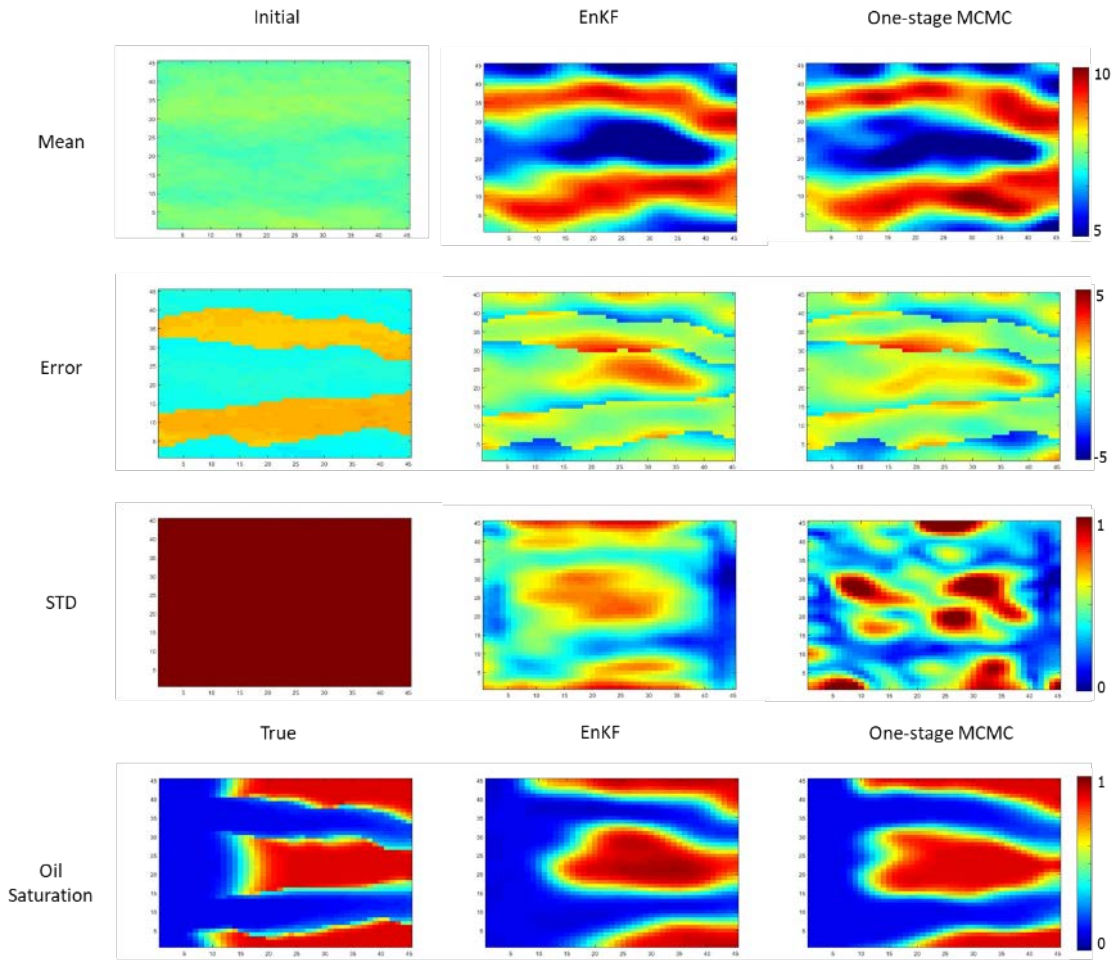

Fig. 36— The log-permeability (log-mD) field of the mean realization (1st row), the mean error estimates of the log-permeability (log-mD) field of the mean realization (2nd row) and the standard deviation of the log-permeability (log-mD) field (3rd row) among all realizations of the initial ensemble (1st column), EnKF realizations (2nd column) and the one-stage MCMC realizations (3rd column) after the 9th update (27 months). Oil saturation maps at 810 days (4th row) for the true realization (1st column), EnKF ensemble mean (2nd column) and the mean of one-stage MCMC (3rd column).

5.6.4 Posterior Results at 1080 Days

Fig. 37 compares the mean, error, standard deviation estimates and oil saturation maps at the end of the twelfth assimilation cycle (36 months). The mean estimates for both cases become even more defined and continuous. The error estimates look fairly similar, in general, although they appear to get larger in the middle of the field, in the unswept oil areas. This could be indicative of a spurious correlation effect produced by EnKF updating. Because the correlation between log-permeability values in the unswept oil zones and the observed measurements is weak, more noise accumulates with time and leads to deterioration of the estimates in these regions. The oil saturation maps show small changes from the maps obtained at 810 days, which suggests that no major changes occurred in the flow patterns of the field. This explains the small changes in the posterior estimates from the previous ones at 810 days.

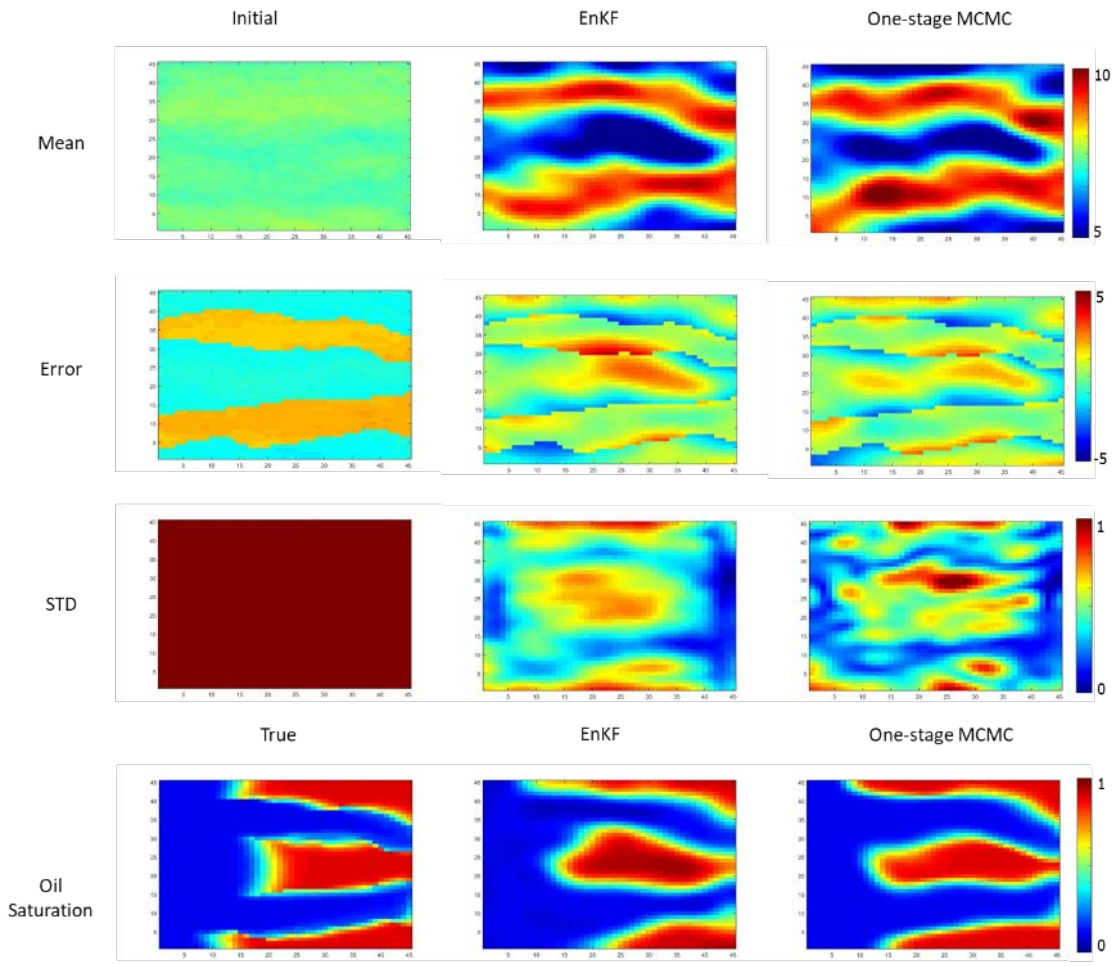

Fig. 37— The log-permeability (log-mD) field of the mean realization (1st row), the error in the log-permeability (log-mD) field of the mean realization (2nd row) and the standard deviation of the log-permeability (log-mD) field (3rd row) among all realizations of the initial ensemble (1st column), EnKF realizations (2nd column) and the one-stage MCMC realizations (3rd column) after the 12th update (36 months). Oil saturation maps at 1080 days (4th row) for the true realization (1st column), EnKF ensemble mean (2nd column) and the mean of one-stage MCMC (3rd column).

5.6.5 Convergence and Chain-Mixing Analysis

Fig. 38 shows the acceptance ratio curves for the four continuous multi-level EnKF/one-stage MCMC chains (run in series of 500 iterations per chain). The curves seem to converge to values in the range of 0.18 to 0.28. This is a desirable range for a chain mixing quality (see Sec. 2.4.2.2).

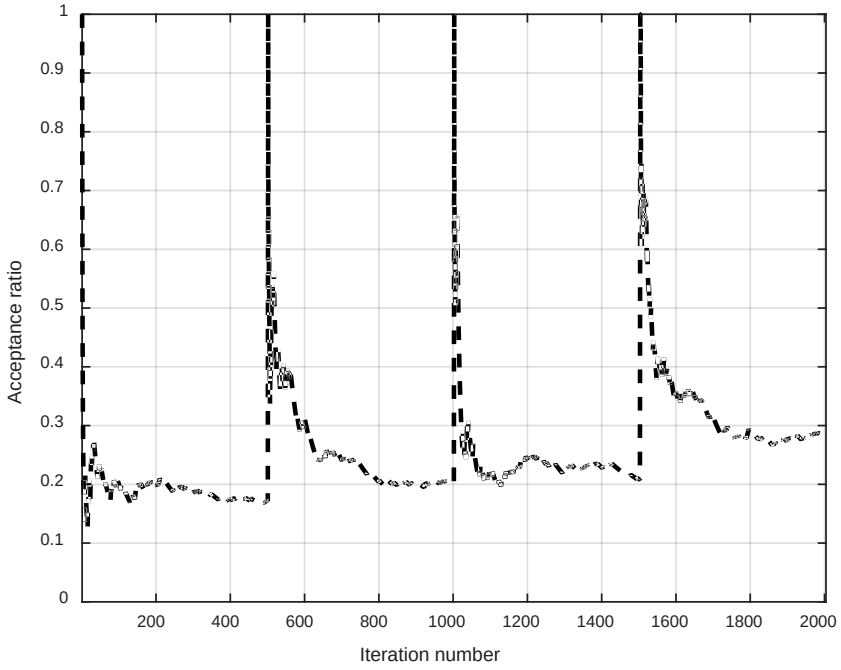

Fig. 38—Acceptance ratios for the four continuous multi-level EnKF/one-stage MCMC chains.

Fig. 39 shows the posterior objective function normalized by the number of measurement data points for the four continuous multi-level EnKF/one-stage MCMC chains (run in series of 500 iterations per chain). The values continue to decline, indicating better matches to the observed data and higher probability of posterior. However, the curves do not show stationary behavior—they continue to decline and do not settle around a constant value, suggesting more runs need to be generated to reach convergence. Also, this probably suggests that posterior estimates obtained by the MCMC chains, presented in the subsections above, show less than actual variability, and more runs are required to reach regions of higher posterior probability.

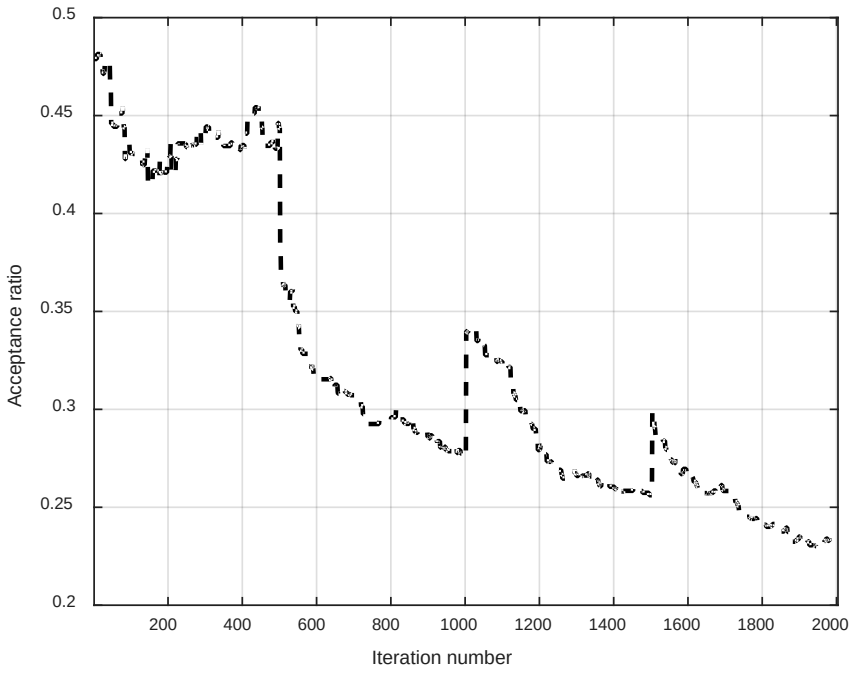

Fig. 39**—Normalized objective functions for the four multi-level EnKF/one-stage MCMC experiments.**

5.6.6 Comparison of Production Profiles

Fig. 40–42 compare production profiles of the MCMC with EnKF-based proposal runs to those for open loop (running the initial ensemble without model updating) and EnKF runs. The MCMC runs narrow the ranges obtained by EnKF updates even further. The mean of MCMC is slightly closer to the true case than the mean of EnKF.

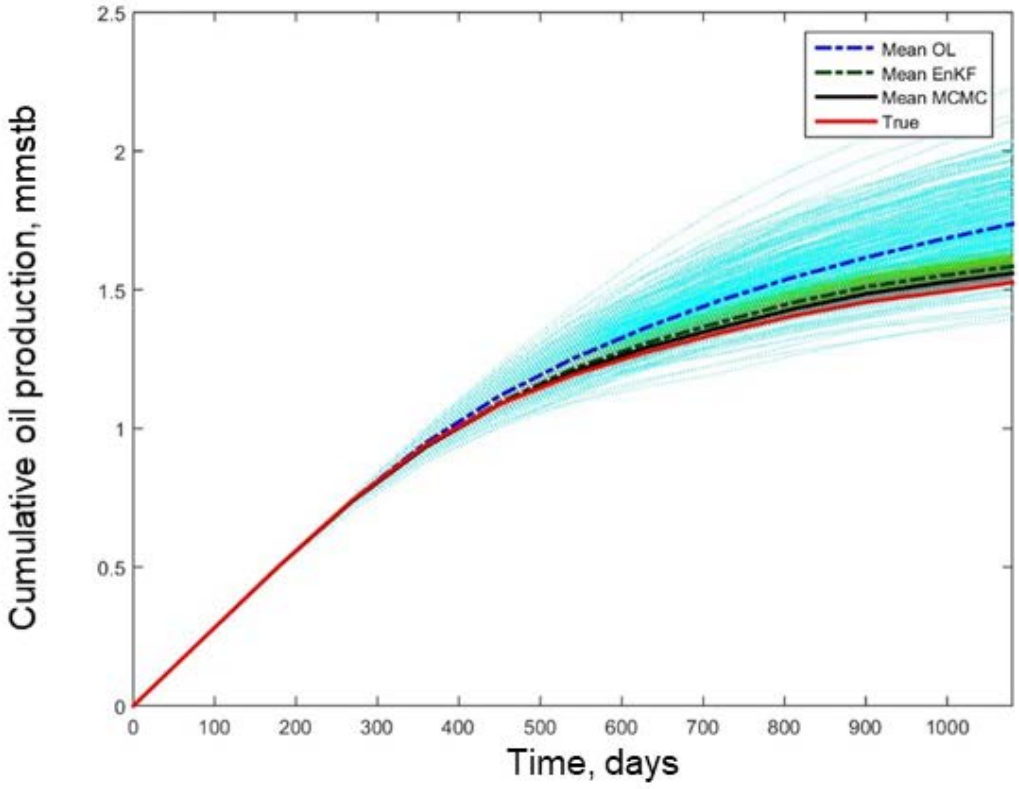

Fig. 40— Cumulative oil production showing the open loop runs (cyan), the mean of open loop runs (dashed blue), EnKF final updated ensemble (green), mean of EnKF final updated ensemble (dashed green), multi-level EnKF/one-stage MCMC realizations (grey), the mean of multi-level EnKF/one-stage MCMC (black) and the truth case (red).

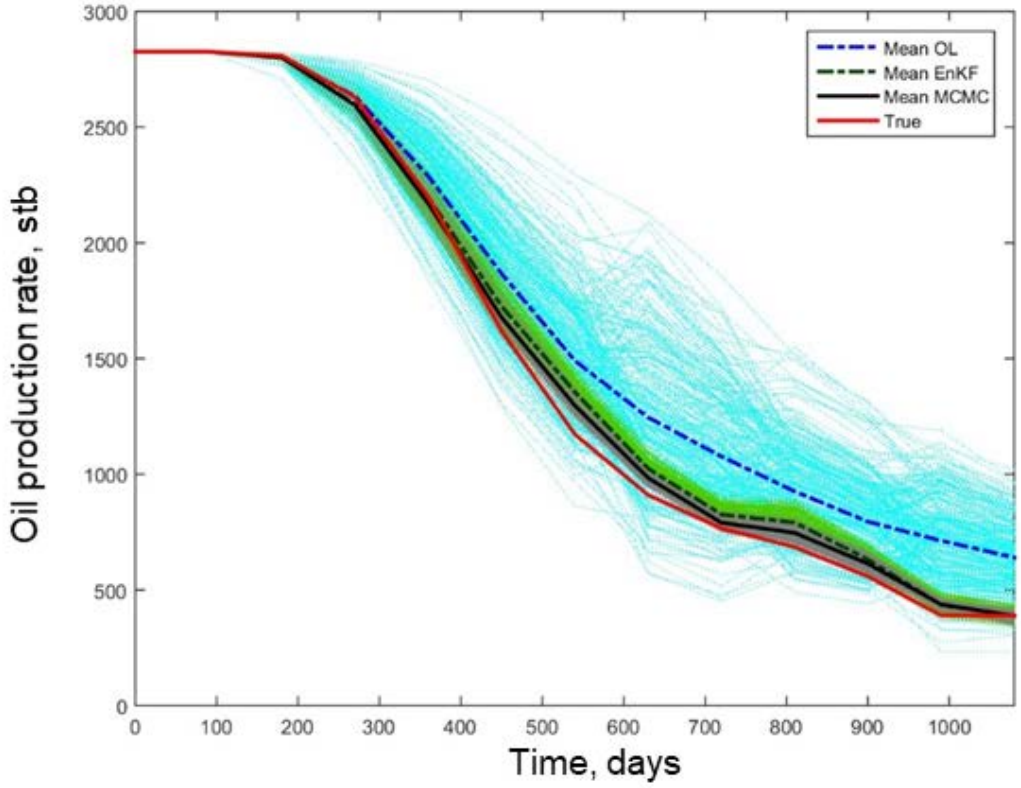

Fig. 41— Oil production rate showing the open loop runs (cyan), the mean of open loop runs (dashed blue), EnKF final updated ensemble (green), mean of EnKF final updated ensemble (dashed green), multi-level EnKF/one-stage MCMC realizations (grey), the mean of multi-level EnKF/one-stage MCMC (black) and the truth case (red).

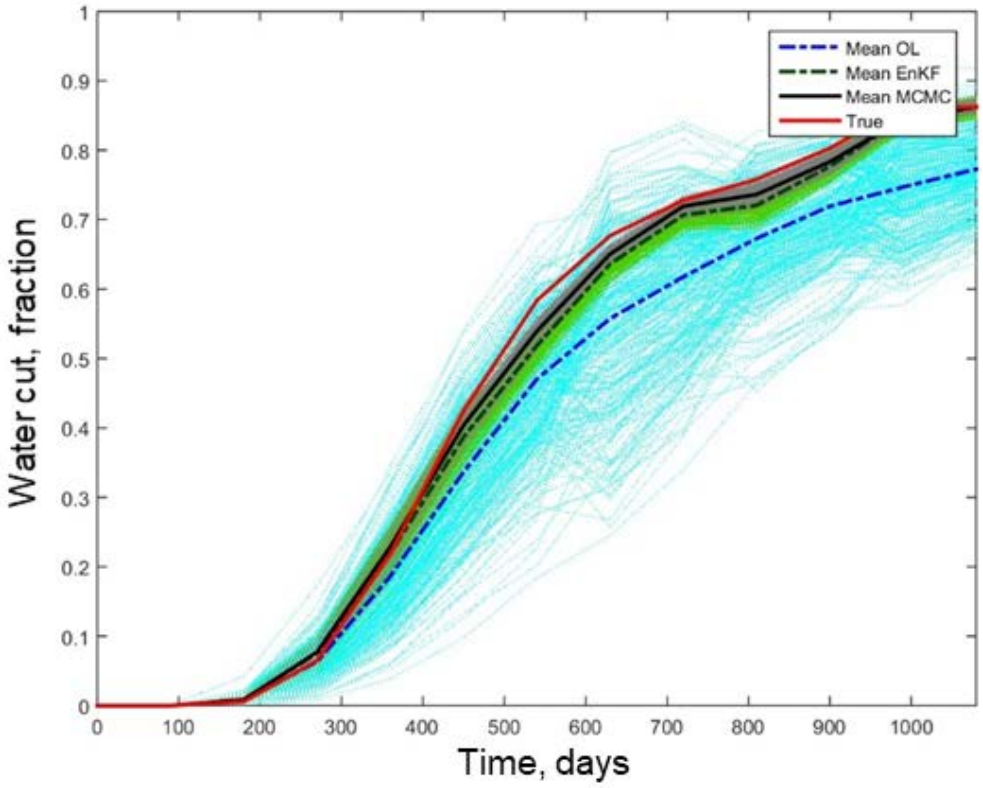

Fig. 42—Water cut showing the open loop runs (cyan), the mean of open loop runs (dashed blue), EnKF final updated ensemble (green), mean of EnKF final updated ensemble (dashed green), multi-level EnKF/one-stage MCMC realizations (grey), the mean of multi-level EnKF/one-stage MCMC (black) and the truth case (red).

5.6.7 Comparison to Standard Random-Walk Case

Fig. 43 and 44 compare acceptance ratio curves and objective function values, respectively, for a standard random-walk perturbation case and a multi-level EnKF/one-stage MCMC case. Both cases include all the observed measurements, up to 1080 days, in the evaluation of the likelihood function. The standard random-walk case appears to stabilize at very low acceptance ratio values, less than 0.05, with higher objective function values, indicating poor-mixing and sampling of low posterior probability models. The

multi-level EnKF/one-stage MCMC case appears to stabilize at acceptance ratio values around 0.19. This is close to the range suggested for a well-mixed chain (see Sec. 2.4.2.2).

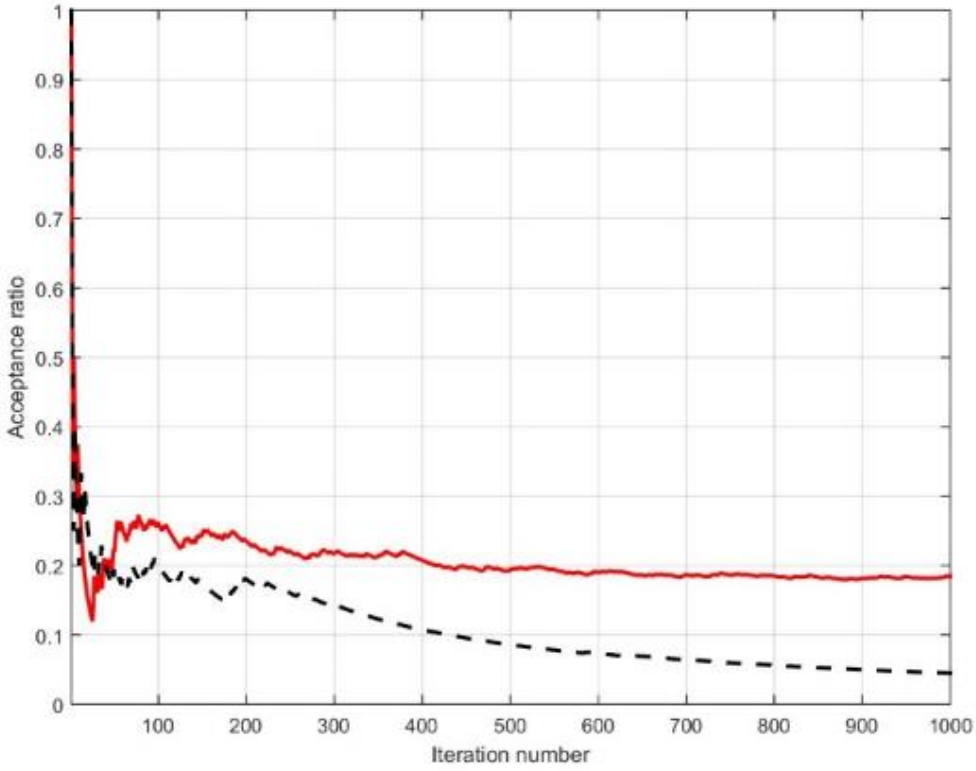

Fig. 43— Acceptance ratios for standard MCMC experiment (dashed black) and multi-level EnKF/one-stage MCMC (red).

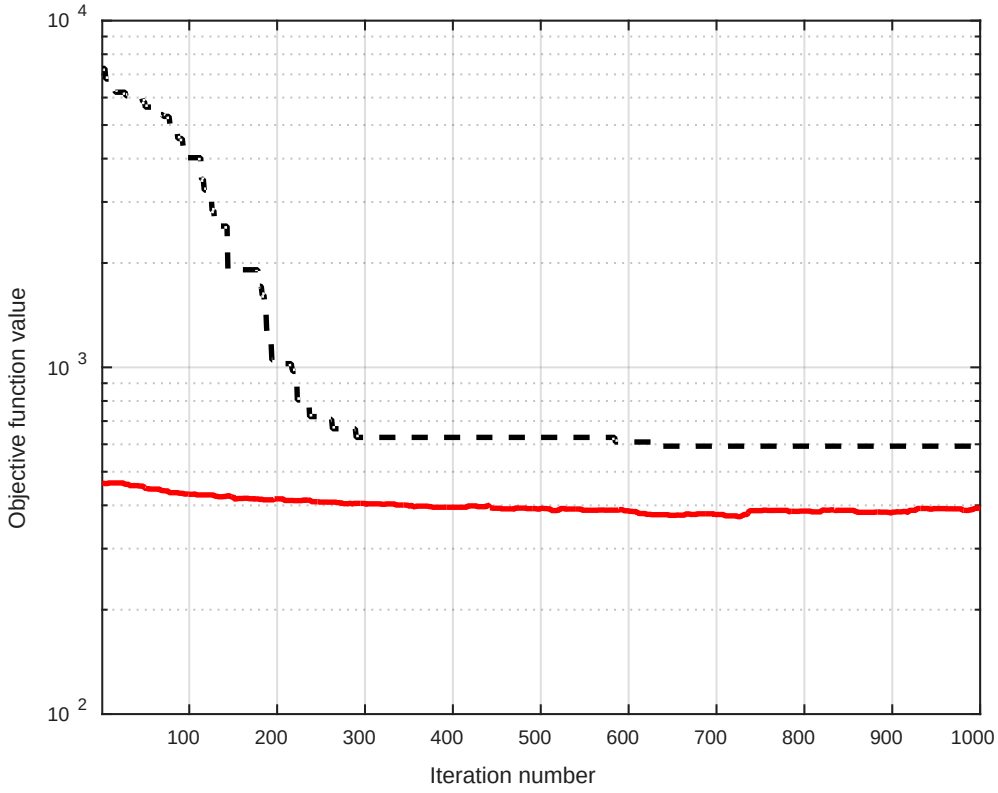

Fig. 44— Objective function for standard MCMC experiment (dashed black) and multi-level EnKF/one-stage MCMC (red).

5.7 Continuous Multi-Level Case Using EnKF/Two-Stage MCMC

In this subsection, the continuous multi-level model updating and uncertainty quantification algorithm using EnKF/two-stage MCMC (see Sec. 3.2 and Fig. 2–3) is tested on the 2-D channelized water flooding problem. The results of the experiment—estimates of the posterior log-permeability field and production forecast—are presented and compared to results obtained by EnKF and the multi-level EnKF/one-stage MCMC. Analysis of the results is provided, and an assessment of improvements in estimation and efficiency is presented.

In this experiment, the first level consists of assimilation cycles of 90 days. Each cycle is followed by EnKF update. After three first-level assimilation cycles (270 days), a two-stage MCMC chain is run using the cumulative covariance calculated at the end of the first level. This results in four MCMC chains at 270, 540, 810, and 1080 days.

The following subsections present the results generated by these four MCMC chains. For each of the four chains, posterior estimates are presented. Additionally, efficiency measures are provided and compared to the multi-level EnKF/one-stage MCMC case. This is followed by analysis of the forecasted production profiles generated by these chains. Finally, a discussion of the posterior estimates of the log-permeability field and the uncertainty quantification of the production forecast is provided.

5.7.1 Posterior Results at 270 Days

Fig. 45 compares acceptance ratio curves of the multi-level EnKF/one-stage MCMC and multi-level EnKF/two-stage MCMC. The comparison shows that at the same level of proposal variance, the two-stage approach results in acceptance ratios (0.5) that are more than double those for the one-stage process (0.2). This allows—for the same number of iterations—more accepted samples to be included in the chain without compromising chain mixing (i.e., the size of the jump in the proposal is maintained). Thus, the effective sample size increases.

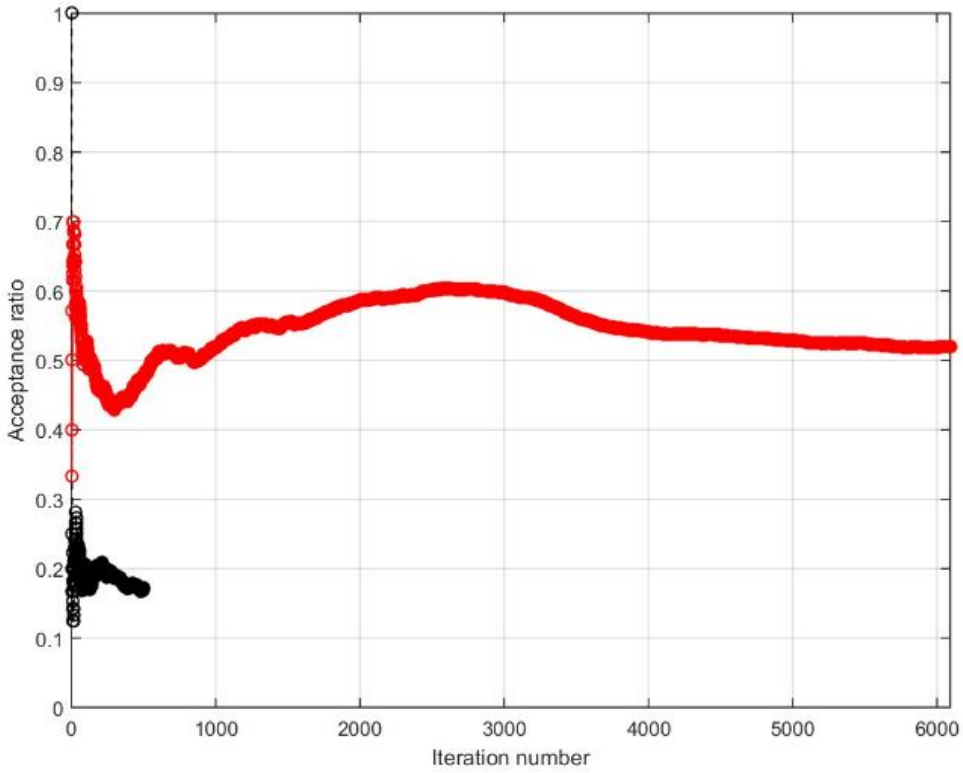

Fig. 45—Comparing the acceptance ratio curves for the multi-level EnKF and MCMC cases at the 3rd assimilation cycle (270 days): one-stage MCMC (black) and two-stage MCMC (red).

Fig. 46 compares the posterior objective function values for the members of the ensemble updated by EnKF at the end of the third assimilation cycle (270 days), the chain generated using the multi-level EnKF/one-stage MCMC method, and the chain generated using the multi-level EnKF/two-stage MCMC method. The comparison shows that both multi-level cases have lower values of the posterior objective function than the EnKF case (i.e., samples from regions of higher posterior probability).

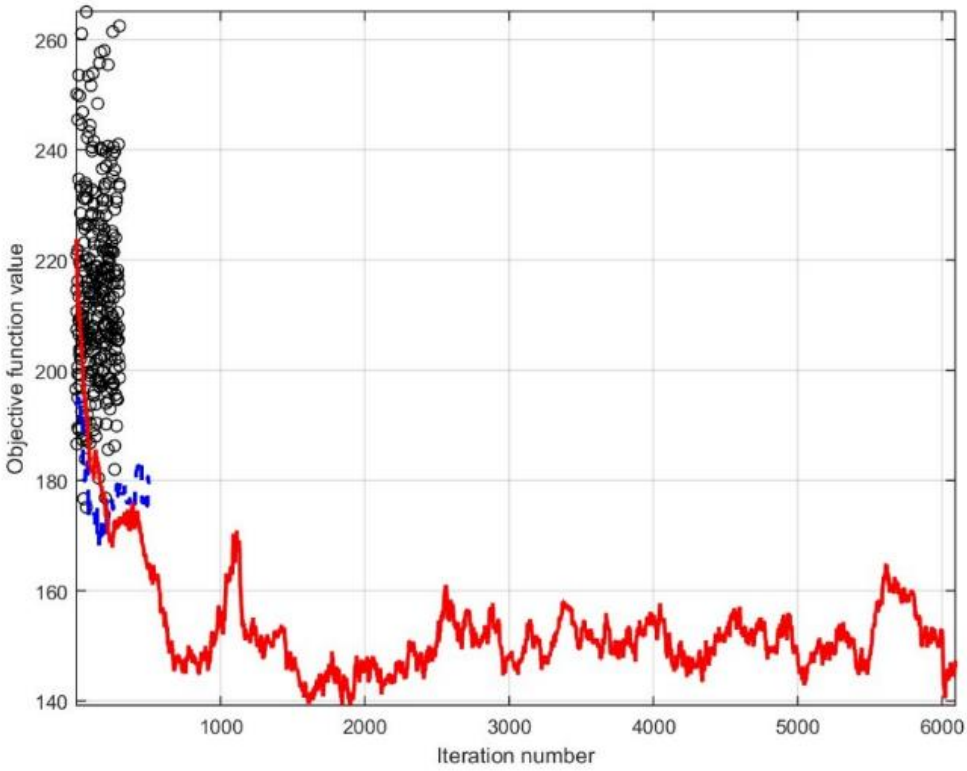

Fig. 46—Comparing the posterior objective function values at the 3rd assimilation cycle (270 days) for the EnKF case (black circles), multi-level EnKF/one-stage MCMC case (blue dashed line) and the multi-level EnKF/two-stage MCMC case (red solid line).

Fig. 47 shows the box plots for the objective function values generated by the two-stage MCMC chain at 270 days (first and second half of the chain), after discarding a burn-in size of 1,000 iterations. Because the two halves of the chain show similar values of the main quantiles, this could be an indication that the chain is stationary. As discussed previously (see Sec. 2.4.2.3), this does not guarantee that the chain is, in fact, stationary or well-mixed.

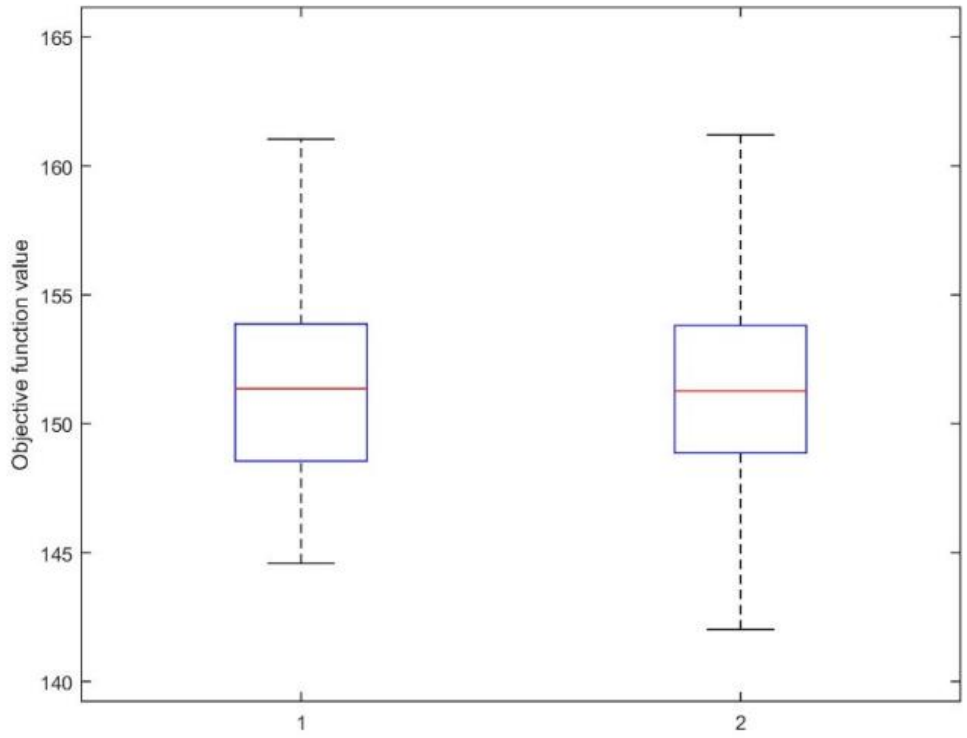

Fig. 47—Box plot for the objective function values for the 1st and the 2nd halves of the two-stage MCMC chain at 270 days (after discarding burn-in): the 50th percentile (red line), 25th and 75th percentiles (blue box), the minimum and maximum (black lines).

Fig. 48 and 49 compare oil production rate and water cut forecasts generated by running the reservoir simulator to the end of the total simulation time (1080 days) for the following cases: initial ensemble realizations (open-loop), ensemble generated by EnKF at the end of the third assimilation cycle, and realizations generated by the multi-level EnKF/two-stage MCMC sampling. The comparisons show that all cases bracket the true case during the history period. At the prediction period, the EnKF and the multi-level realizations seem to bracket the true case for a portion of the prediction period, up to 450

days. Both EnKF and the multi-level cases are shown to have similar mean realizations while the multi-level range seems to be slightly narrower than EnKF. Although the EnKF and multi-level forecasts do not bracket the true oil production rate at later times, the means of these realizations is closer to the truth case than the open-loop case. Because the true realization is bracketed by the prior realizations and is also favored by the observed measurement (i.e., maximizes the likelihood function), this indicates that both EnKF and multi-level EnKF/two-stage MCMC methods have not sampled all regions of the posterior distribution and, thus, are underestimating the posterior uncertainty.

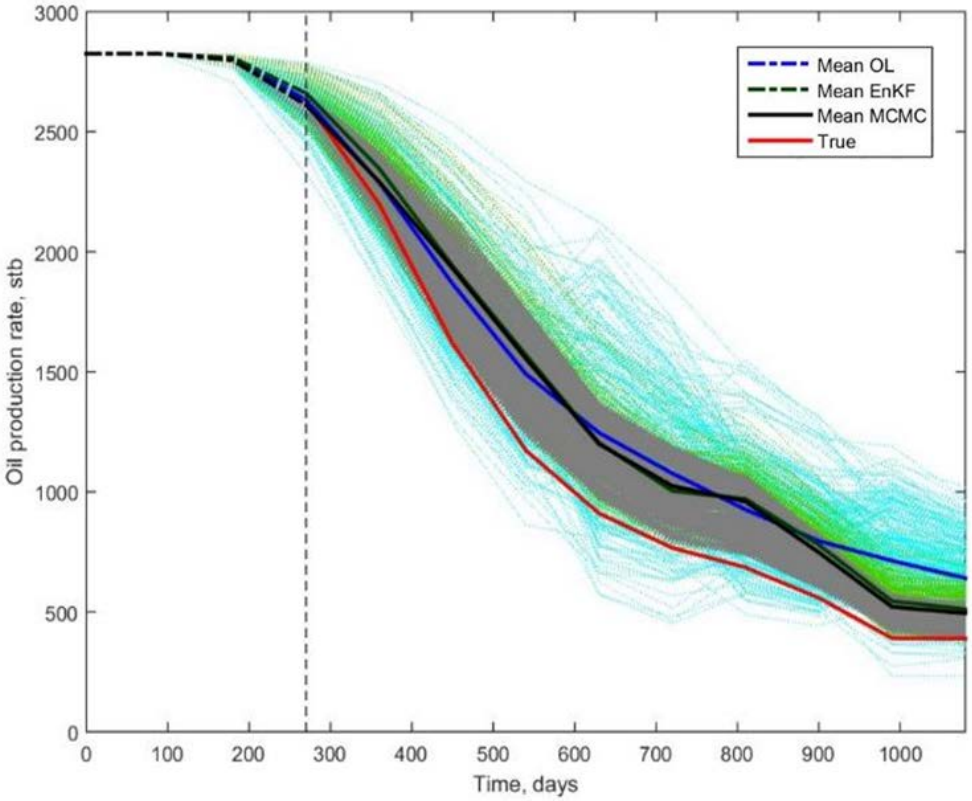

Fig. 48—Oil production rate prediction after the 3rd assimilation cycle: the open-loop prediction (cyan), prediction based on EnKF update (light green), prediction based on multi-level EnKF/two-stage MCMC sampling (grey), the mean of the open-loop predictions (blue), the mean of the EnKF predictions (green), the mean of the multi-level EnKF, two-stage MCMC (black) and the true realization (red). The history period is represented by dashed lines, and the prediction period is represented by solid lines, while the vertical dashed line represents the end of history period.

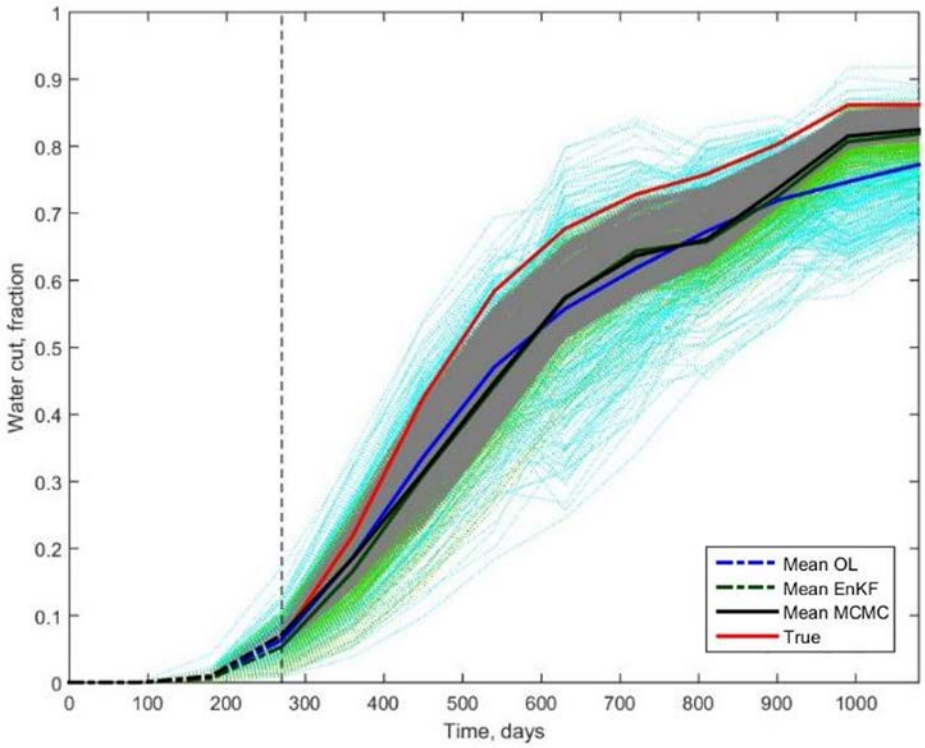

Fig. 49—Water cut prediction after the 3rd assimilation cycle: the open-loop prediction (cyan), prediction based on EnKF update (light green), prediction based on multi-level EnKF/two-stage MCMC sampling (grey), the mean of the open-loop predictions (blue), the mean of the EnKF predictions (green), the mean of the multi-level EnKF/two-stage MCMC (black), and the true realization (red). The history period represented by dashed lines and prediction period represented by solid lines and the vertical dashed line represents the end of history period.

Fig. 50 and 51 compare cumulative oil and cumulative water production forecasts for the same cases mentioned in the previous paragraph. The cumulative production forecasts share the same characteristics as oil-production-rate and water-cut forecasts described in the previous paragraph. Compared to the rate and water-cut plots, cumulative plots show that the range of the profiles increases as time advances. This is due to the

cumulative nature of the curves—differences add up over time and become more pronounced at later times.

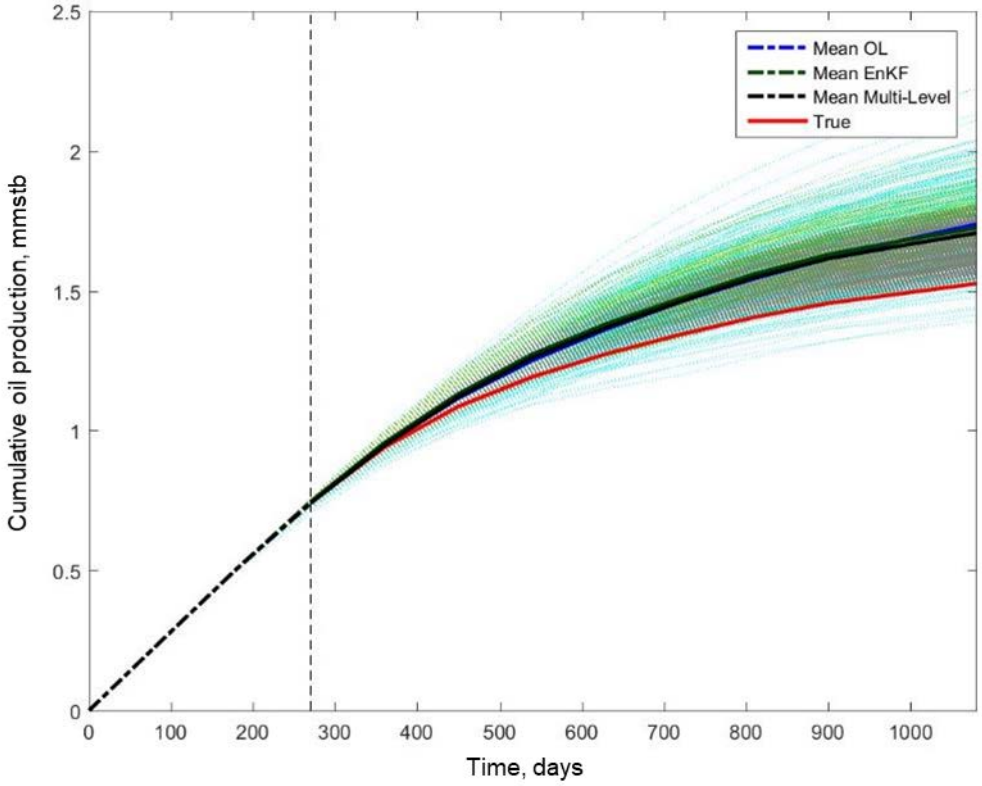

Fig. 50—Cumulative oil production prediction after the 3rd assimilation cycle: the open-loop prediction (cyan), prediction based on EnKF update (light green), prediction based on multi-level EnKF/two-stage MCMC sampling (grey), the mean of the open-loop predictions (blue), the mean of the EnKF predictions (green), the mean of the multi-level EnKF/two-stage MCMC (black), and the true realization (red). The history period represented by dashed lines and prediction period represented by solid lines and the vertical dashed line represents the end of history period.

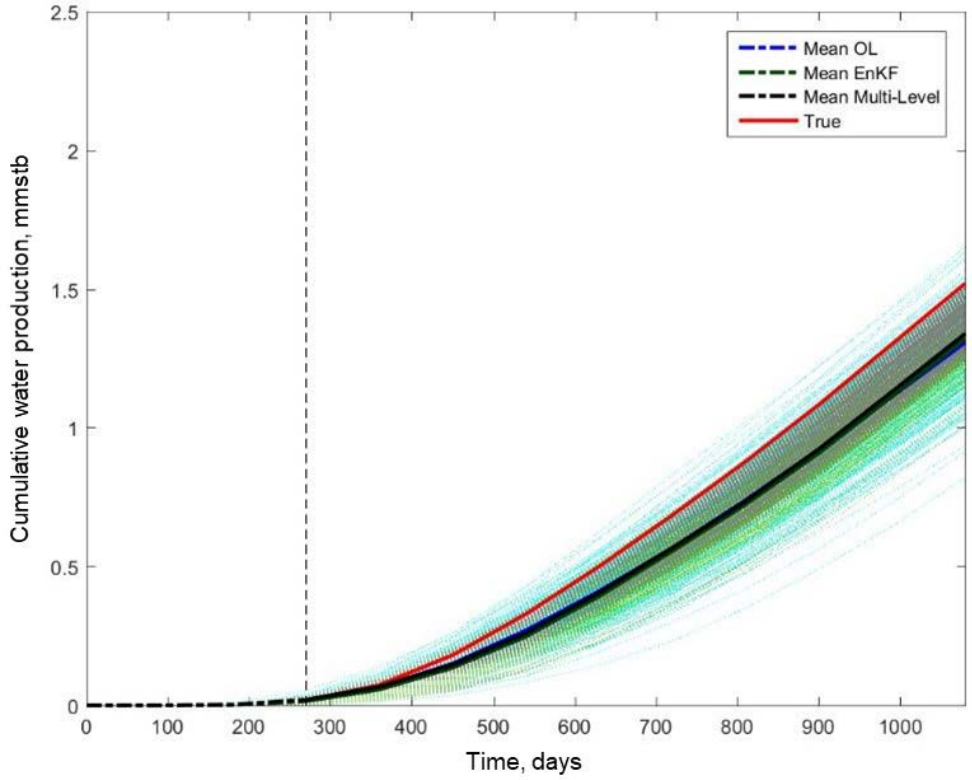

Fig. 51—Cumulative water production prediction after the 3rd assimilation cycle: the open-loop prediction (cyan), prediction based on EnKF update (light green), prediction based on multi-level EnKF/two-stage MCMC sampling (grey), the mean of the open-loop predictions (blue), the mean of the EnKF predictions (green), the mean of the multi-level EnKF/two-stage MCMC (black), and the true realization (red). The history period represented by dashed lines and prediction period represented by solid lines and the vertical dashed line represents the end of history period.

Fig. 52 and 53 compare cumulative oil production and cumulative water production, respectively, at the end of the total simulation time (1080 days) forecasted at the end of the third assimilation cycle (270 days) for the initial ensemble realizations (open-loop), EnKF updated realizations and the realizations generated by the multi-level EnKF/two-stage MCMC sampling. Although both EnKF and multi-level cases show

narrower 100% ranges than the open-loop case, they do not quite bracket the true solution. In this case, it is clear that the uncertainty of the posterior is underestimated. The number of iterations (6000) was apparently not sufficient to fully sample the posterior distribution at this updating, in the multi-level case. This is discussed further in Sec. 6.5.

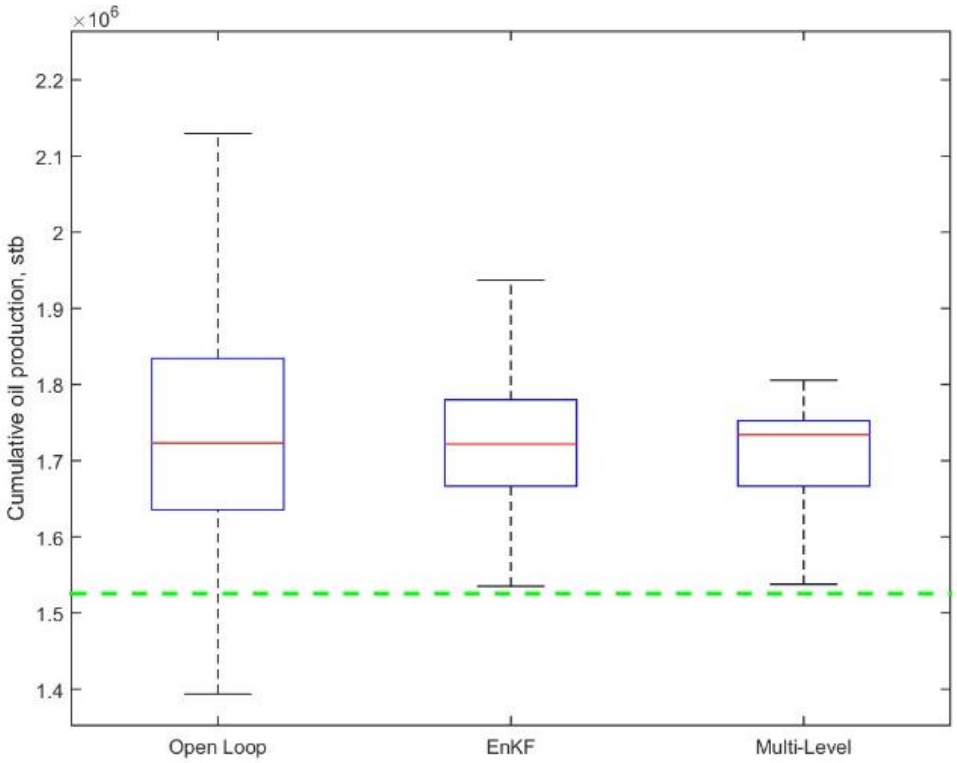

Fig. 52—Box plots for cumulative oil production at the end of the total simulation time (1080 days) forecasted at the end of the 3rd assimilation cycle (270 days): 50th percentile (red line), 25th and 75th percentiles (blue box), the minimum and maximum (black lines) and the true case (green dashed line).

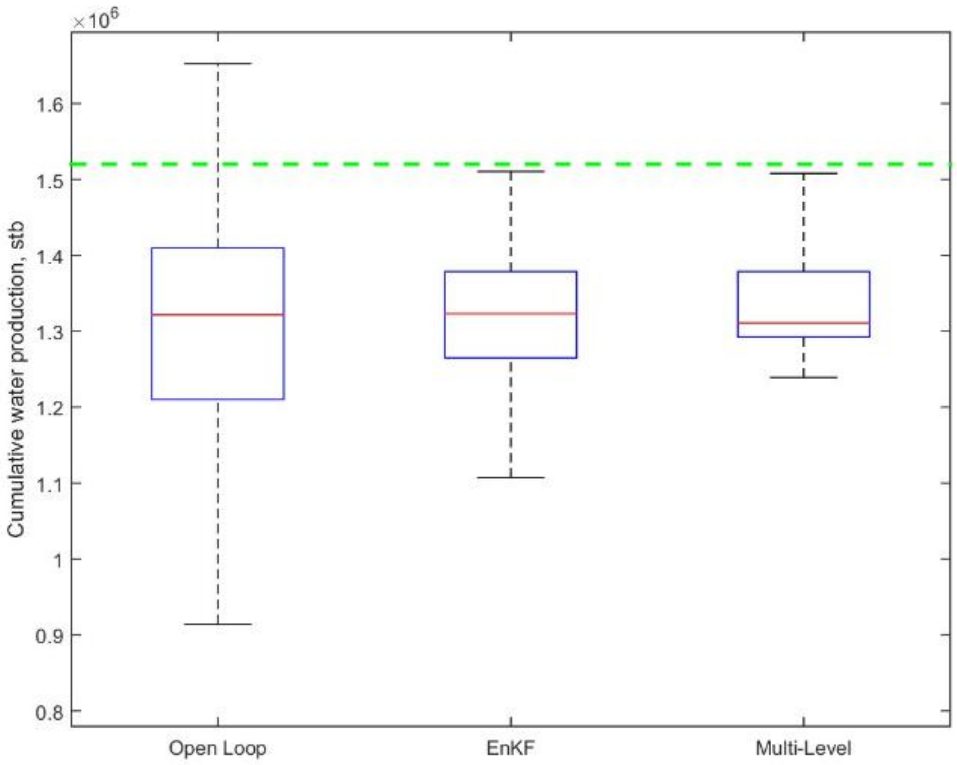

Fig. 53—Box plots for cumulative water production at the end of the total simulation time (1080 days) forecasted at the end of the 3rd assimilation cycle (270 days): 50th percentile (red line), 25th and 75th percentiles (blue box), the minimum and maximum (black lines) and the true case (green dashed line).

5.7.2 Posterior Results at 540 Days

Fig. 54 and 55 compare the acceptance ratio curves and objective function values of the multi-level EnKF/one-stage MCMC and multi-level EnKF/two-stage MCMC. The same conclusions made in the previous section seem to hold here, as well.

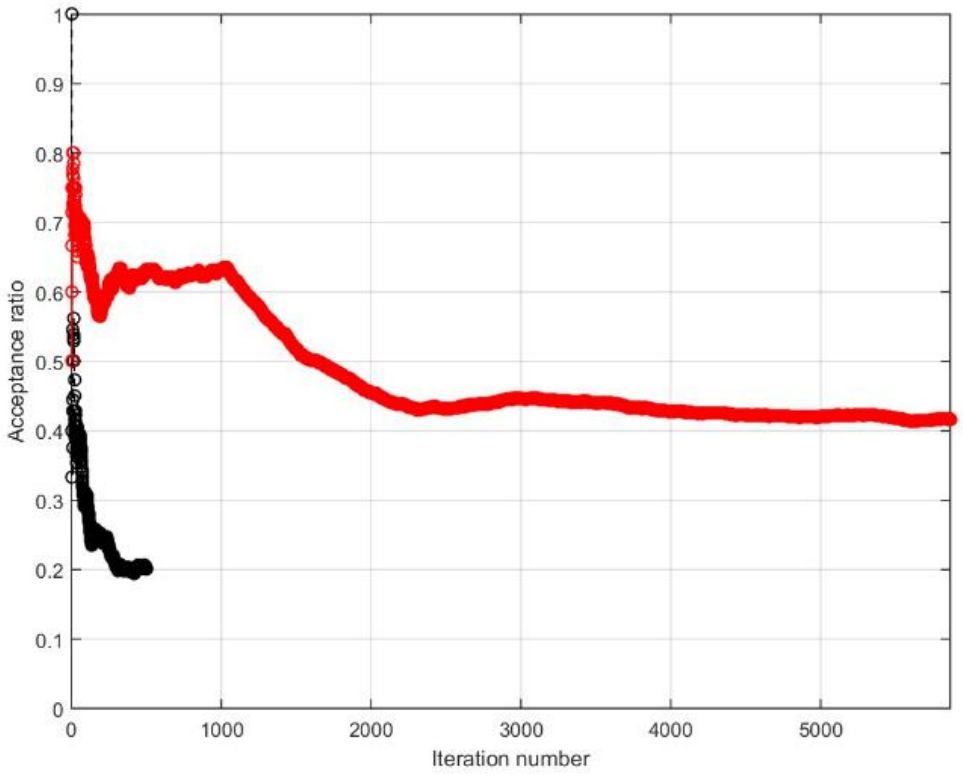

Fig. 54—Comparing the acceptance ratio curves for the multi-level EnKF/MCMC cases at the 6th assimilation cycle (540 days): one-stage MCMC (black) and two-stage MCMC (red).

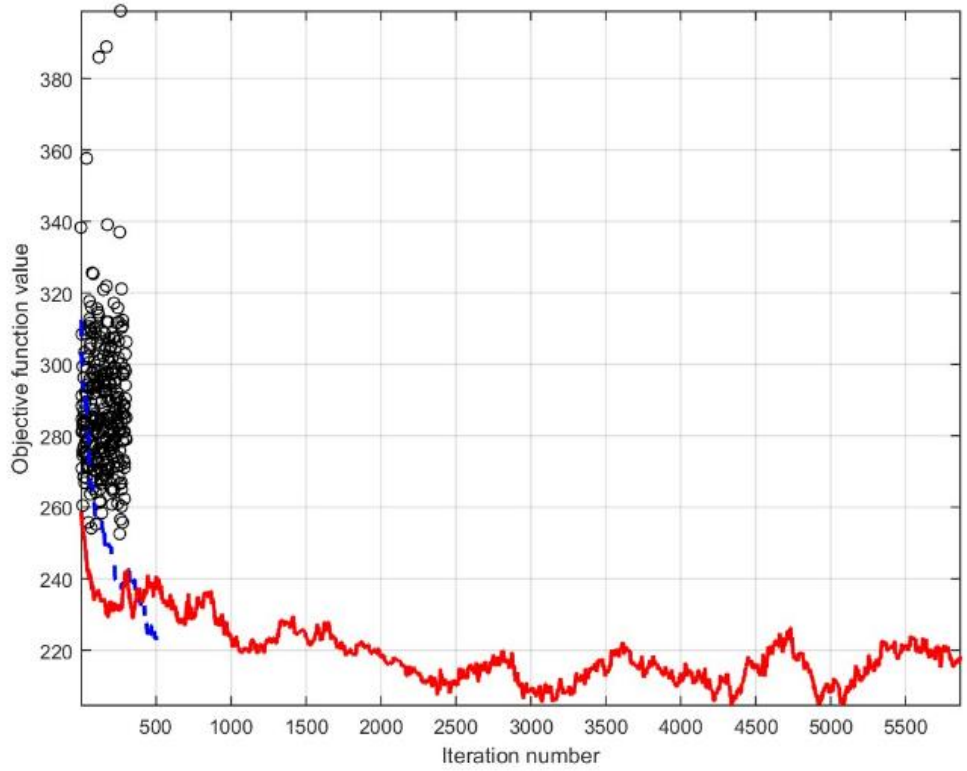

Fig. 55—Comparing the posterior objective function values at the 6th assimilation cycle (540 days) for the EnKF case (black circles), multi-level EnKF/one-stage MCMC case (blue dashed line), and the multi-level EnKF/two-stage MCMC case (red solid line).

As in the previous section, **Fig. 56** shows box plots for the objective function values of the two halves of the chain generated by the two-stage MCMC at 540 days, after discarding a burn-in size of 1,000 iterations. Here, the main quantiles do not look significantly different (less than 5% difference). Again, this does not guarantee stationarity, but could be used as an indication that the chain could be stationary.

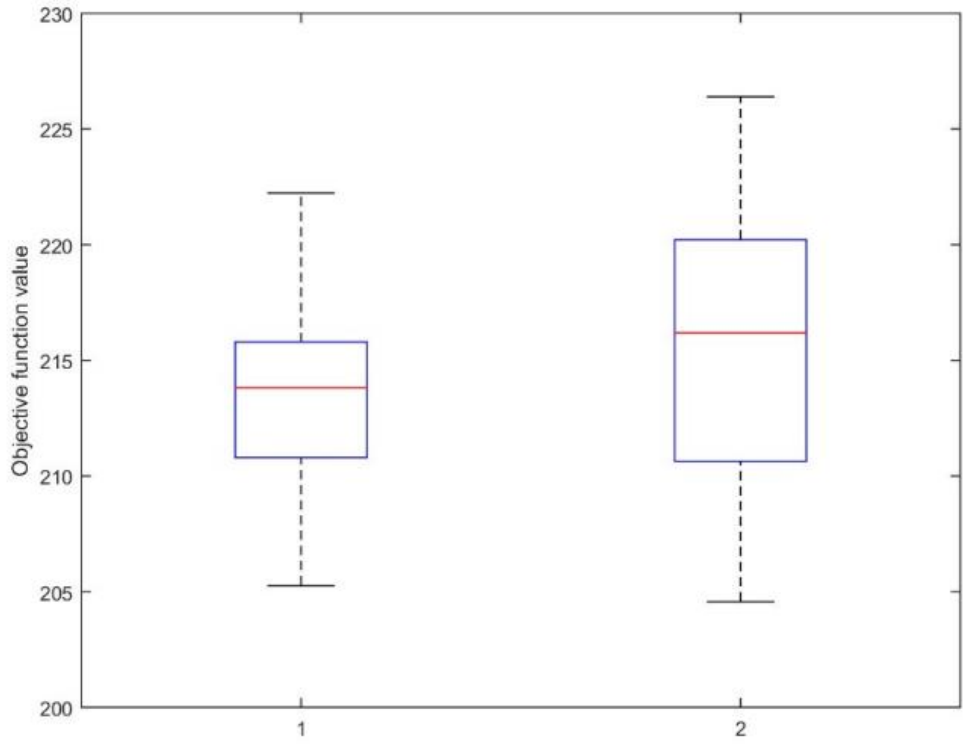

Fig. 56—Box plot for the objective function values for the 1st (1) and the 2nd (2) halves of the two-stage MCMC chain at 540 days: 50th percentile (red line), 25th and 75th percentiles (blue box), the minimum and maximum (black lines) and the true case (green dashed line).

As in the previous section, **Fig. 57-60** compares the oil production rate, water cut and cumulative production forecasts. Like the results in the previous section, while the results seem to indicate an underestimation of the posterior uncertainty, the means of both EnKF and the multi-level case appear to be similar, while the multi-level range seems to be slightly narrower than EnKF.

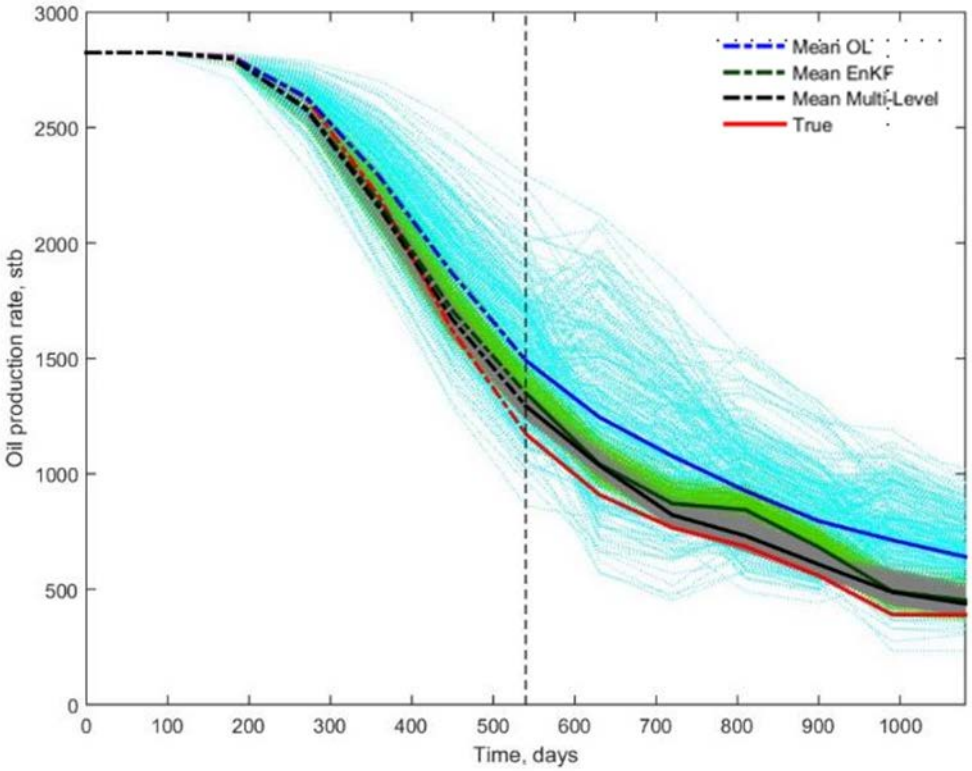

Fig. 57—Oil production rate prediction after the 6th assimilation cycle: the open-loop prediction (cyan), prediction based on EnKF update (light green), prediction based on multi-level EnKF/two-stage MCMC sampling (grey), the mean of the open-loop predictions (blue), the mean of the EnKF predictions (green), the mean of the multi-level EnKF/two-stage MCMC (black), true case (red), history period represented by dashed lines and prediction period represented by solid lines and the vertical dashed line represents the end of history period.

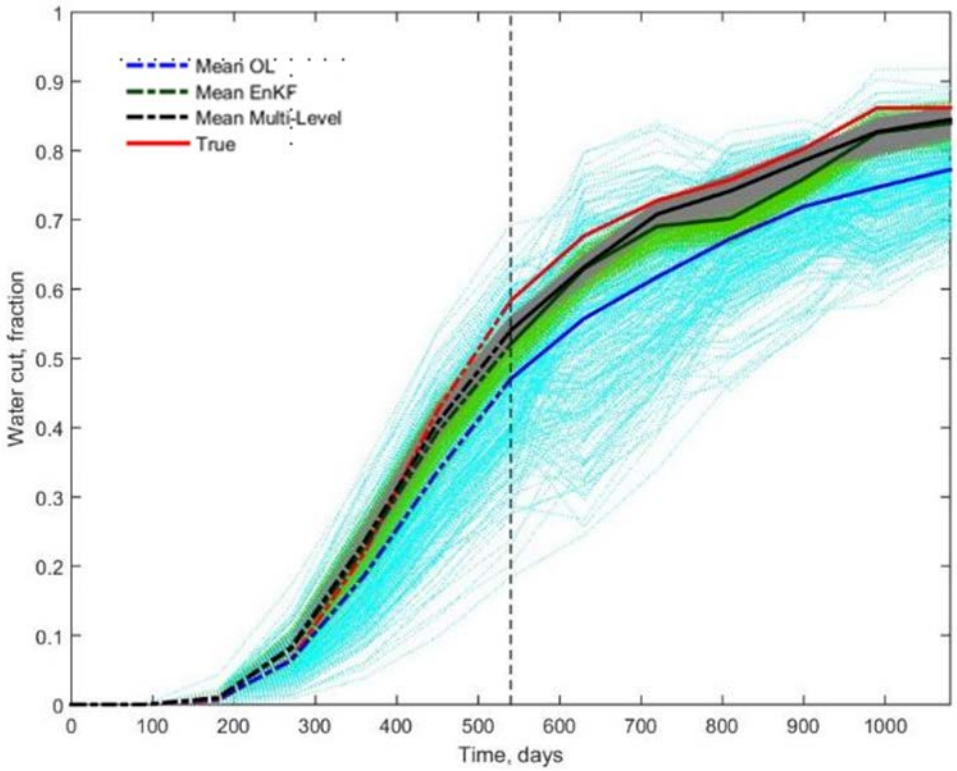

Fig. 58—Water cut prediction after the 6th assimilation cycle: the open-loop prediction (cyan), prediction based on EnKF update (light green), prediction based on multi-level EnKF/two-stage MCMC sampling (grey), the mean of the open-loop predictions (blue), the mean of the EnKF predictions (green), the mean of the multi-level EnKF/two-stage MCMC (black), true case (red), history period represented by dashed lines and prediction period represented by solid lines and the vertical dashed line represents the end of history period.

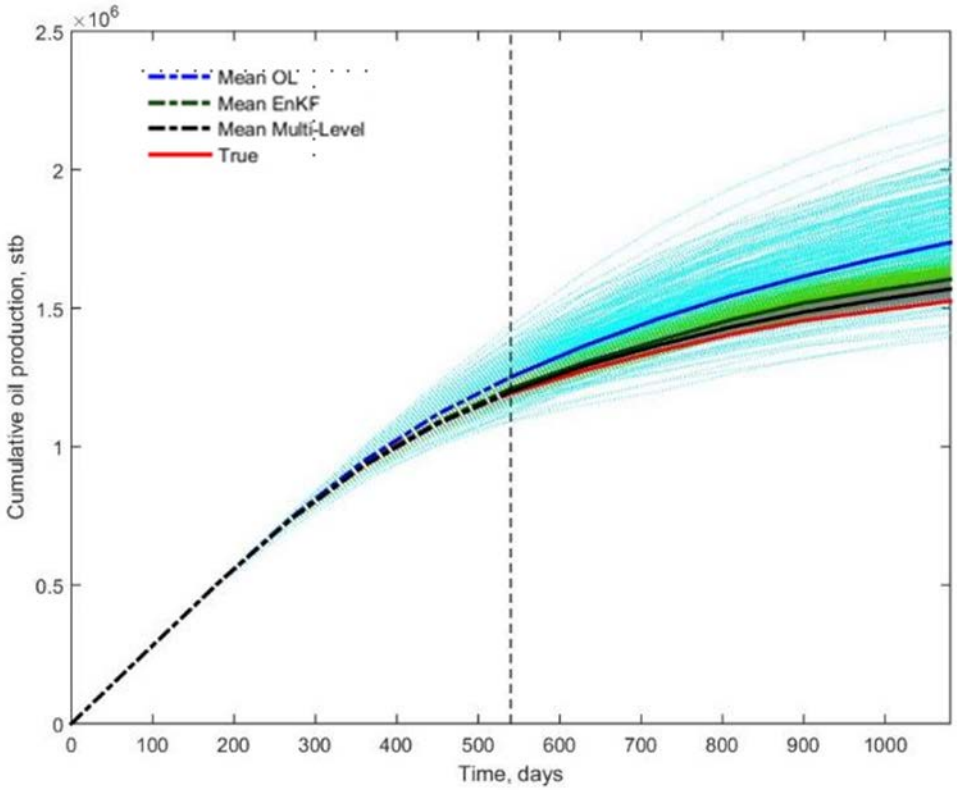

Fig. 59—Cumulative oil production prediction after the 6th assimilation cycle: the open-loop prediction (cyan), prediction based on EnKF update (light green), prediction based on multi-level EnKF/two-stage MCMC sampling (grey), the mean of the open-loop predictions (blue), the mean of the EnKF predictions (green), the mean of the multi-level EnKF/two-stage MCMC (black), true case (red), history period represented by dashed lines and prediction period represented by solid lines and the vertical dashed line represents the end of history period.

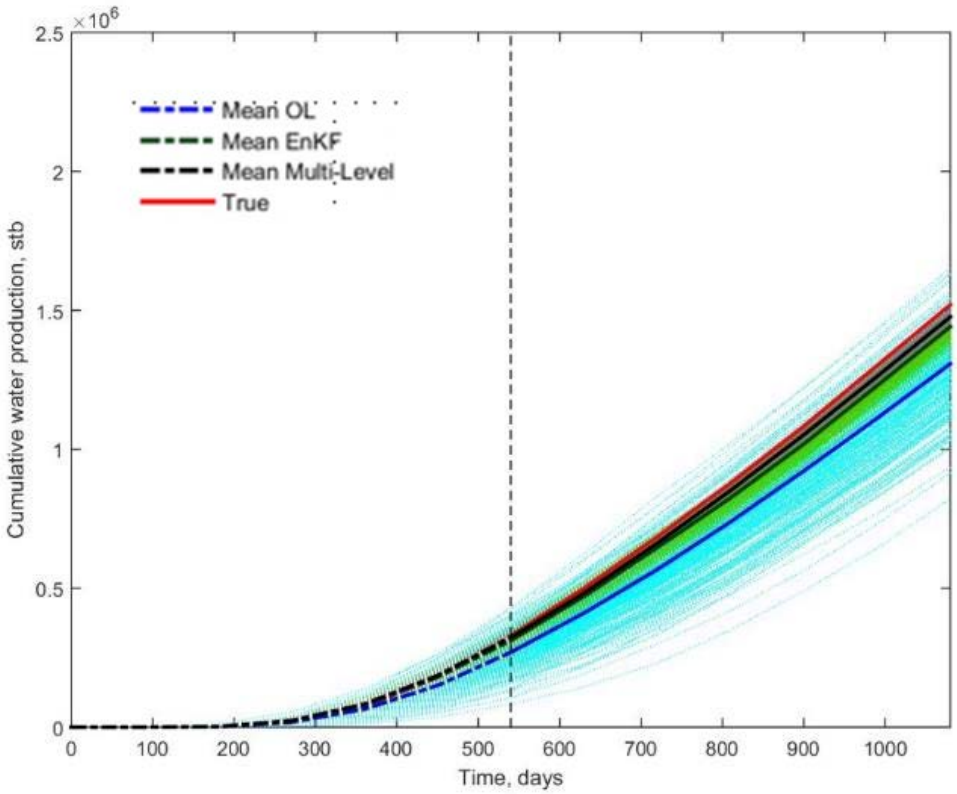

Fig. 60—Cumulative water production prediction after the 6th assimilation cycle: the open-loop prediction (cyan), prediction based on EnKF update (light green), prediction based on multi-level EnKF/two-stage MCMC sampling (grey), the mean of the open-loop predictions (blue), the mean of the EnKF predictions (green), the mean of the multi-level EnKF/two-stage MCMC (black), true case (red), history period represented by dashed lines and prediction period represented by solid lines and the vertical dashed line represents the end of history period.

A comparison of the cumulative production forecasts **(Fig. 61 and 62)** show that the posterior estimates by both EnKF and the multi-level case still mildly underestimate the uncertainty. The multi-level case still shows a narrower range than EnKF and with it main quartiles shifting more toward the true solution.

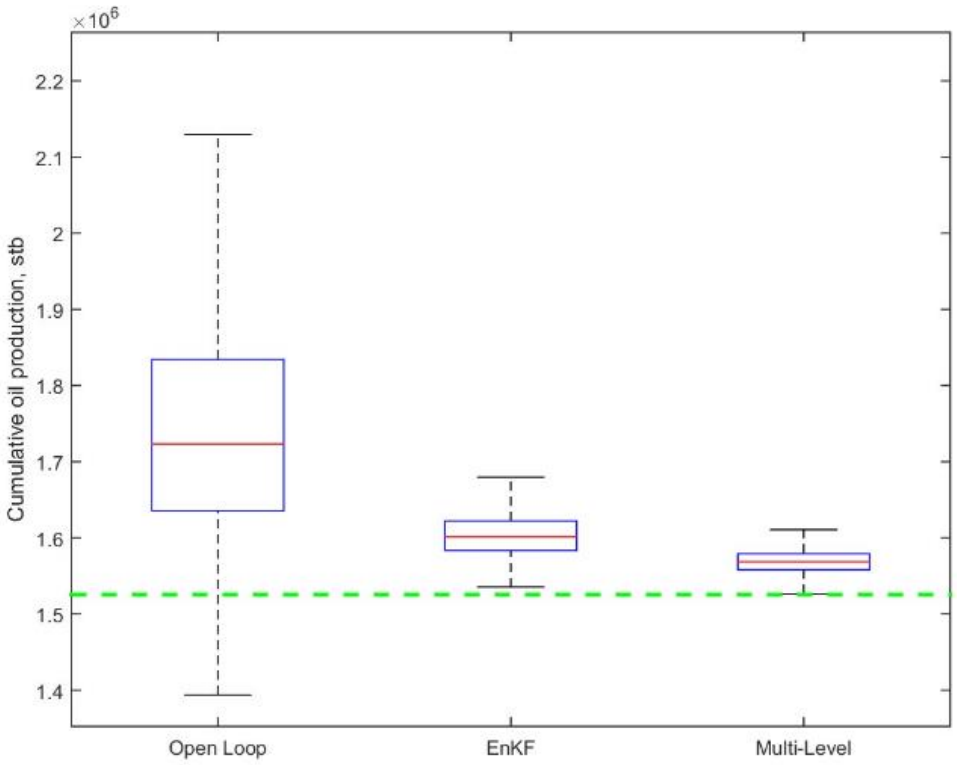

Fig. 61—Box plots for cumulative oil production at the end of the total simulation time (1080 days) forecasted at the end of the 6th assimilation cycle (540 days): 50th percentile (red line), 25th and 75th percentiles (blue box), the minimum and maximum (black lines) and the true case (green dashed line).

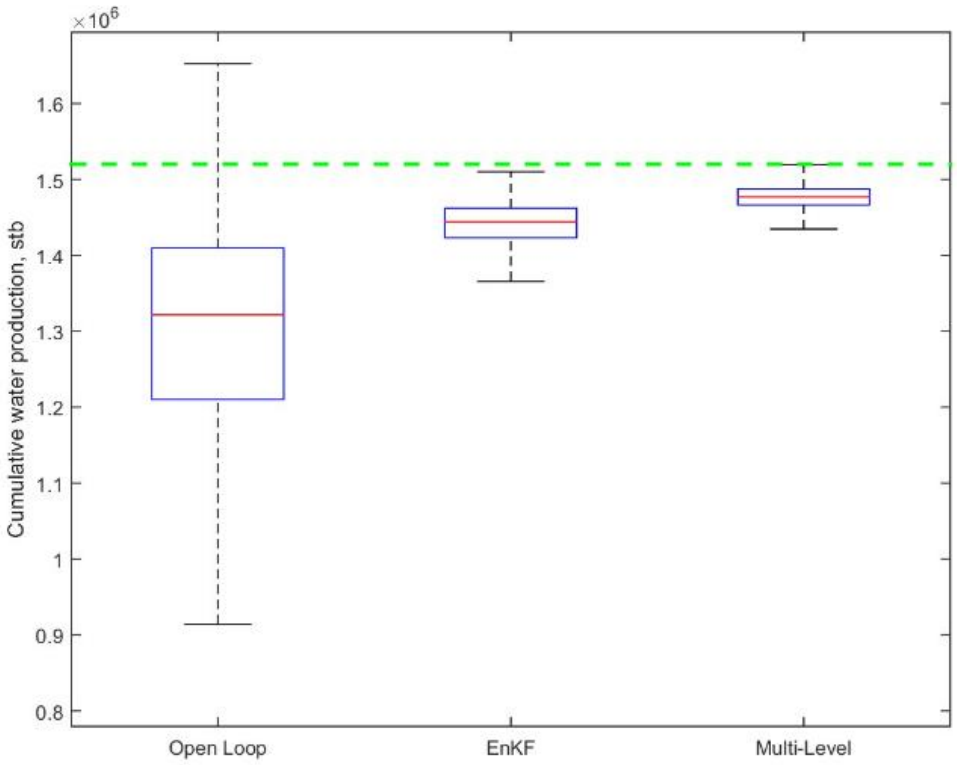

Fig. 62—Box plots for cumulative water production at the end of the total simulation time (1080 days) forecasted at the end of the 6th assimilation cycle (540 days): 50th percentile (red line), 25th and 75th percentiles (blue box), the minimum and maximum (black lines) and the true case (green dashed line).

5.7.3 Posterior Results at 810 Days

As in the previous sections, **Fig. 63** show higher acceptance ratios in the case of multi-level/two-stage MCMC. However, **Fig. 64** show clear signs of non-stationarity, suggesting more iterations should be generated or proposal variance should be increased to generate a better-mixed chain. This could also be indicative of deteriorating EnKF posterior covariance due to spurious correlation as discussed in Sec. 5.6.3. **Fig. 65** supports the fact that the chain is not stationary.

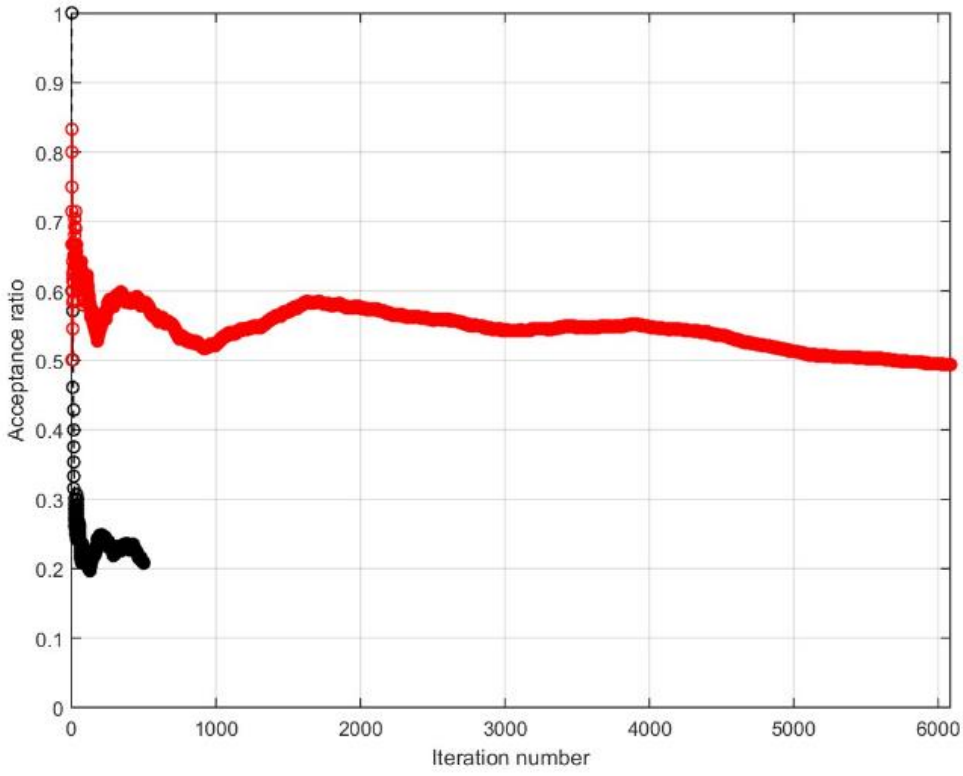

Fig. 63—Comparing the acceptance ratio curves for the multi-level EnKF and MCMC cases at the 9th assimilation cycle (810 days): one-stage MCMC (black) and two-stage MCMC (red).

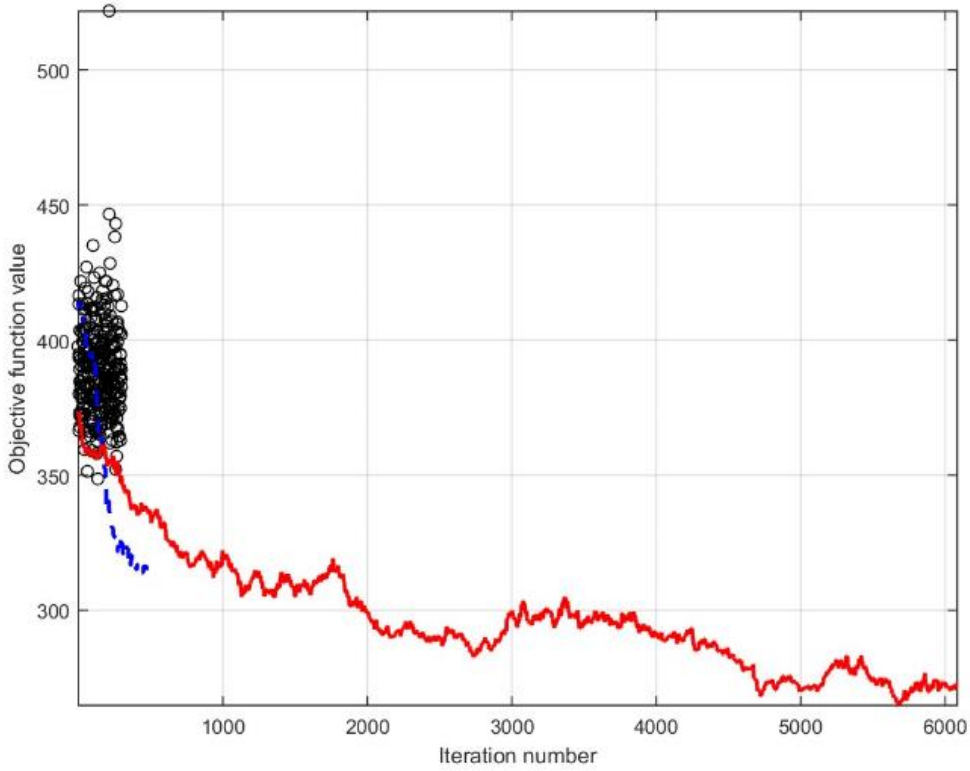

Fig. 64—Comparing the posterior objective function values at the 9th assimilation cycle (810 days) for the EnKF case (black circles), multi-level EnKF/one-stage MCMC case (blue dashed line) and the multi-level EnKF/two-stage MCMC case (red solid line).

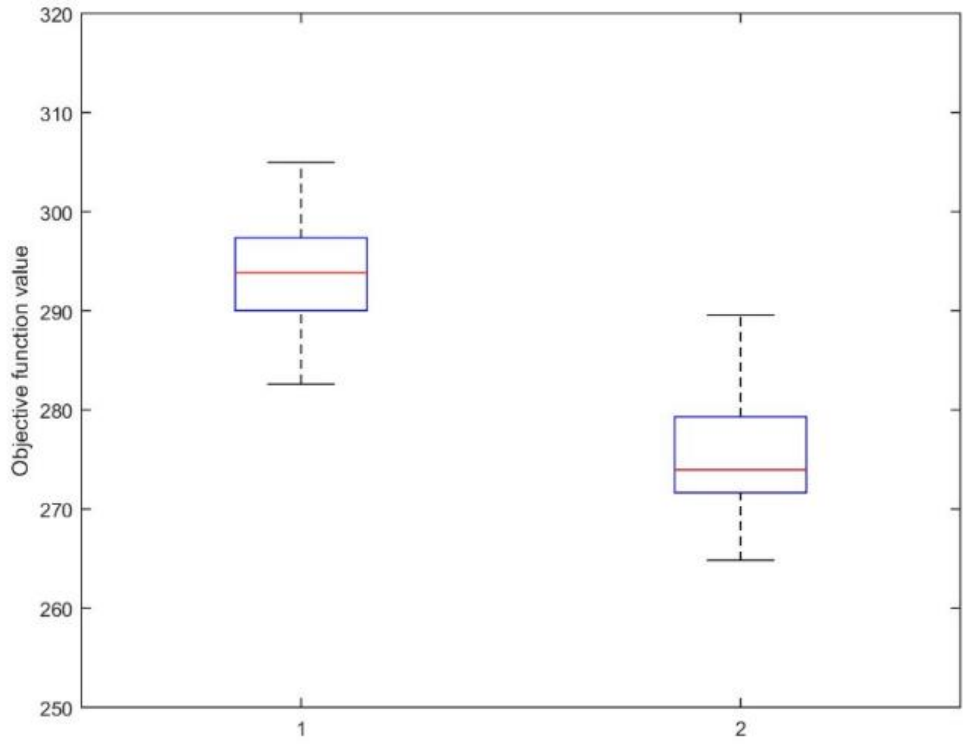

Fig. 65—Box plot for the objective function values for the 1st and the 2nd halves of the two-stage MCMC chain at 810 days): 50th percentile (red line), 25th and 75th percentiles (blue box), the minimum and maximum (black lines) and the true case (green dashed line).

Fig. 66-69 show that the production forecasts at 810 days appear similar to those in the previous sections. The ranges appear even narrower and the means are further closer to the truth case.

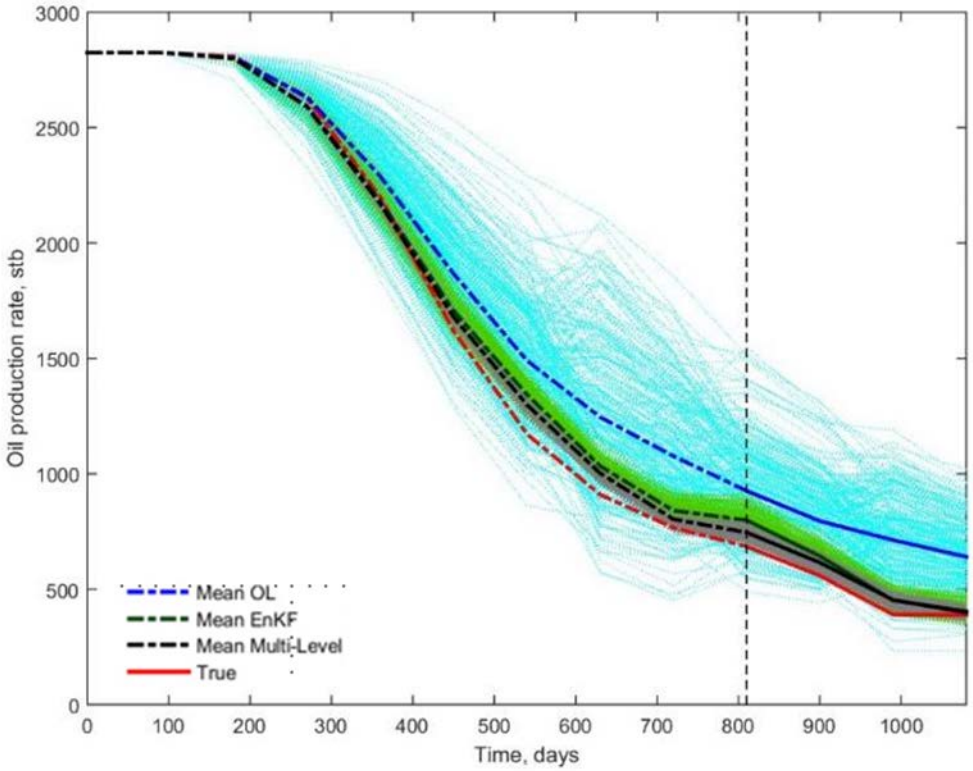

Fig. 66—Oil production rate prediction after the 9th assimilation cycle: the open-loop prediction (cyan), prediction based on EnKF update (light green), prediction based on multi-level EnKF/two-stage MCMC sampling (grey), the mean of the open-loop predictions (blue), the mean of the EnKF predictions (green), the mean of the multi-level EnKF/two-stage MCMC (black), true case (red), history period represented by dashed lines and prediction period represented by solid lines and the vertical dashed line represents the end of history period.

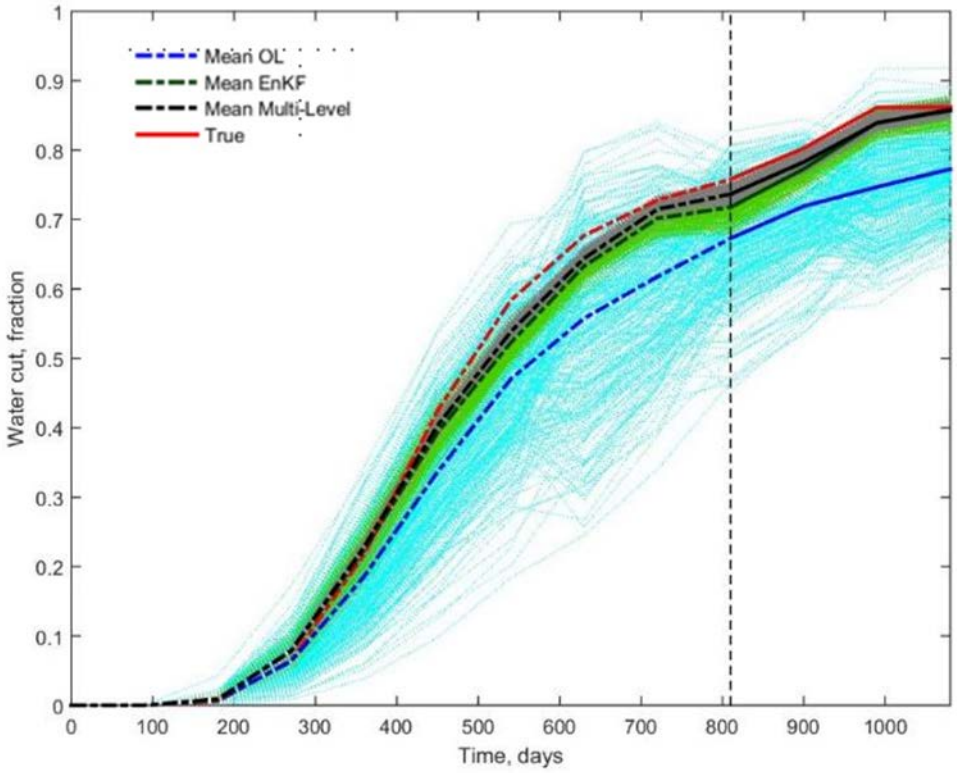

Fig. 67—Water cut prediction after the 9th assimilation cycle: the open-loop prediction (cyan), prediction based on EnKF update (light green), prediction based on multi-level EnKF/two-stage MCMC sampling (grey), the mean of the open-loop predictions (blue), the mean of the EnKF predictions (green), the mean of the multi-level EnKF/two-stage MCMC (black), true case (red), history period represented by dashed lines and prediction period represented by solid lines and the vertical dashed line represents the end of history period.

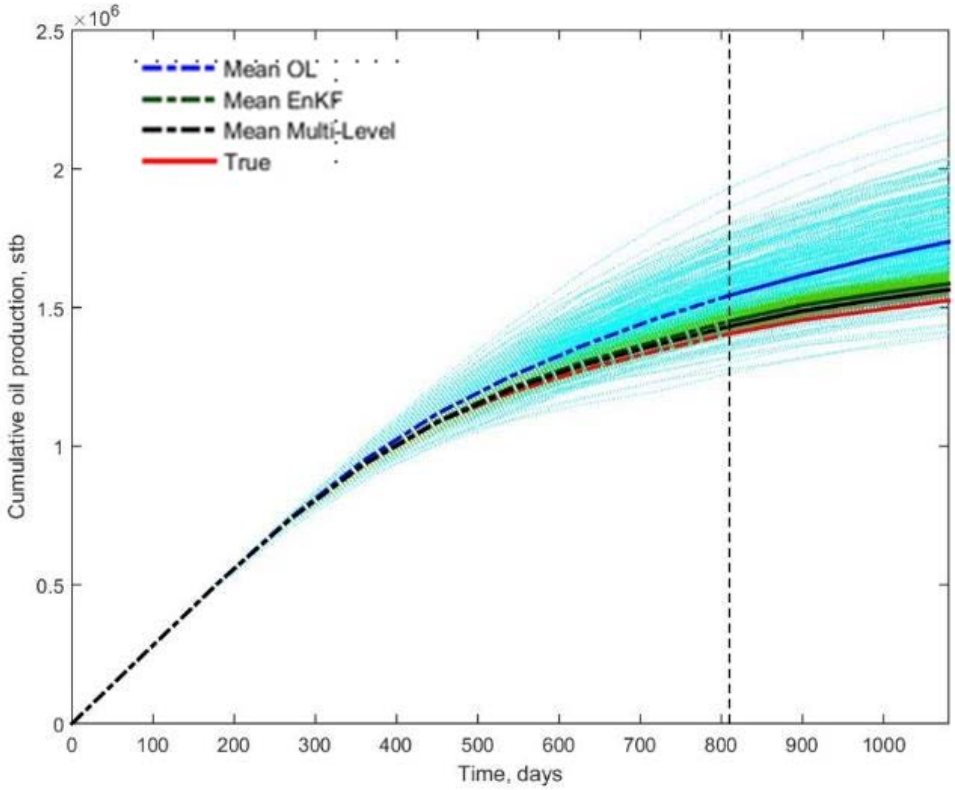

Fig. 68—Cumulative oil production prediction after the 9th assimilation cycle: the open-loop prediction (cyan), prediction based on EnKF update (light green), prediction based on multi-level EnKF/two-stage MCMC sampling (grey), the mean of the open-loop predictions (blue), the mean of the EnKF predictions (green), the mean of the multi-level EnKF/two-stage MCMC (black), true case (red), history period represented by dashed lines and prediction period represented by solid lines and the vertical dashed line represents the end of history period.

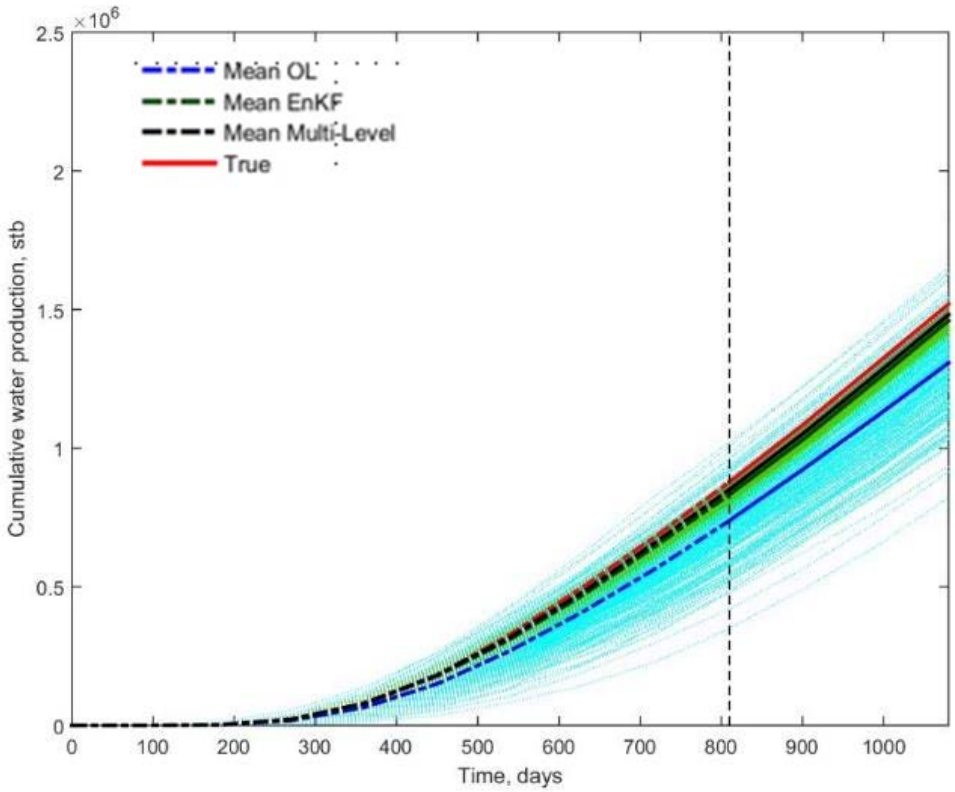

Fig. 69--Cumulative oil production prediction after the 9th assimilation cycle: the open-loop prediction (cyan), prediction based on EnKF update (light green), prediction based on multi-level EnKF/two-stage MCMC sampling (grey), the mean of the open-loop predictions (blue), the mean of the EnKF predictions (green), the mean of the multi-level EnKF/two-stage MCMC (black), true case (red), history period represented by dashed lines and prediction period represented by solid lines and the vertical dashed line represents the end of history period.

At 810 days, the box plots of the cumulative production forecasts **(Fig. 70 and 71)** comparing the prior realizations, EnKF and the multi-level case show that the multi-level case is bracketing the true solution while the EnKF is not. While this does not necessarily mean that there is no underestimation of the forecasted production uncertainty, it shows improvement in the estimation as more observed measurements are assimilated.

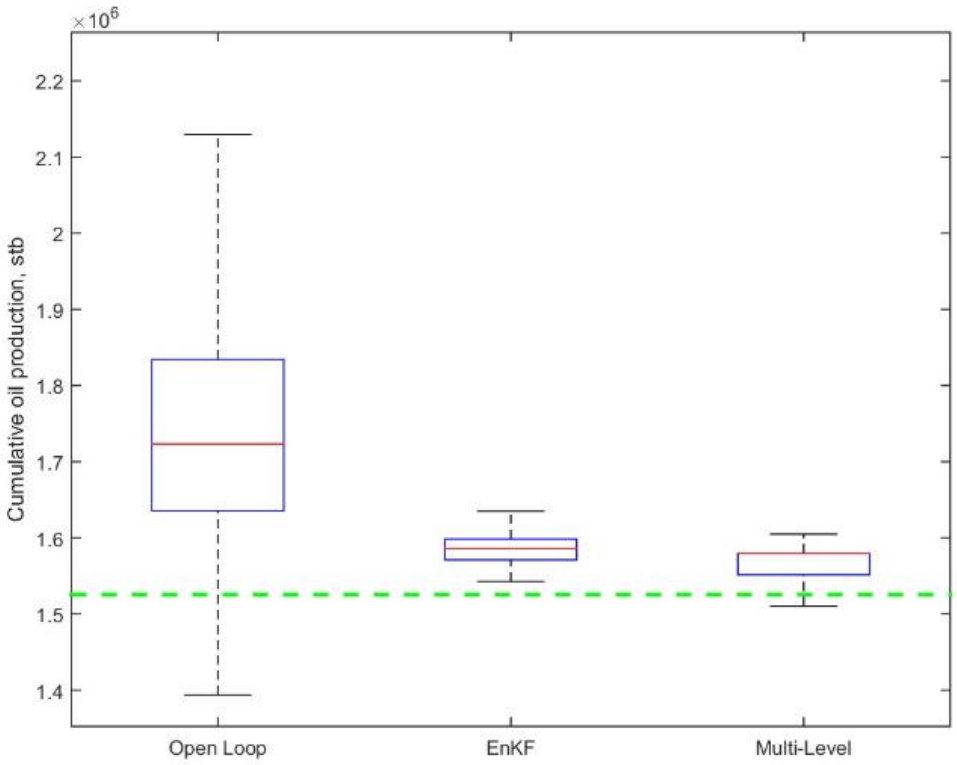

Fig. 70—Box plots for cumulative oil production at the end of the total simulation time (1080 days) forecasted at the end of the 9th assimilation cycle (810 days): 50th percentile (red line), 25th and 75th percentiles (blue box), the minimum and maximum percentiles (black lines) and the true case (green dashed line).

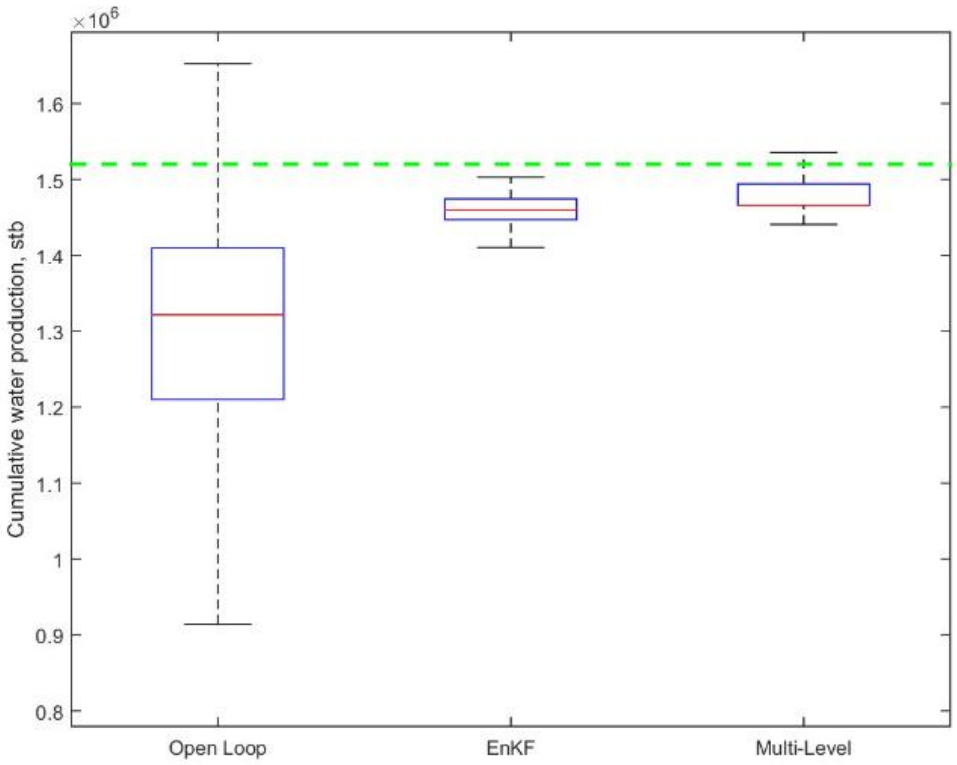

Fig. 71—Box plots for cumulative oil production at the end of the total simulation time (1080 days) forecasted at the end of the 9th assimilation cycle (810 days): 50th percentile (red line), 25th and 75th percentiles (blue box), the minimum and maximum percentiles (black lines) and the true case (green dashed line).

5.7.4 Posterior Results at 1080 Days

At this point of the experiment, all observed measurements are assimilated and no further production forecasts are made. As in the previous section, **(Fig. 72-74)** show that while acceptance ratio is increased, the chain does not appear to be stationary. As discussed, this could be indicative of deteriorating EnKF posterior covariance.

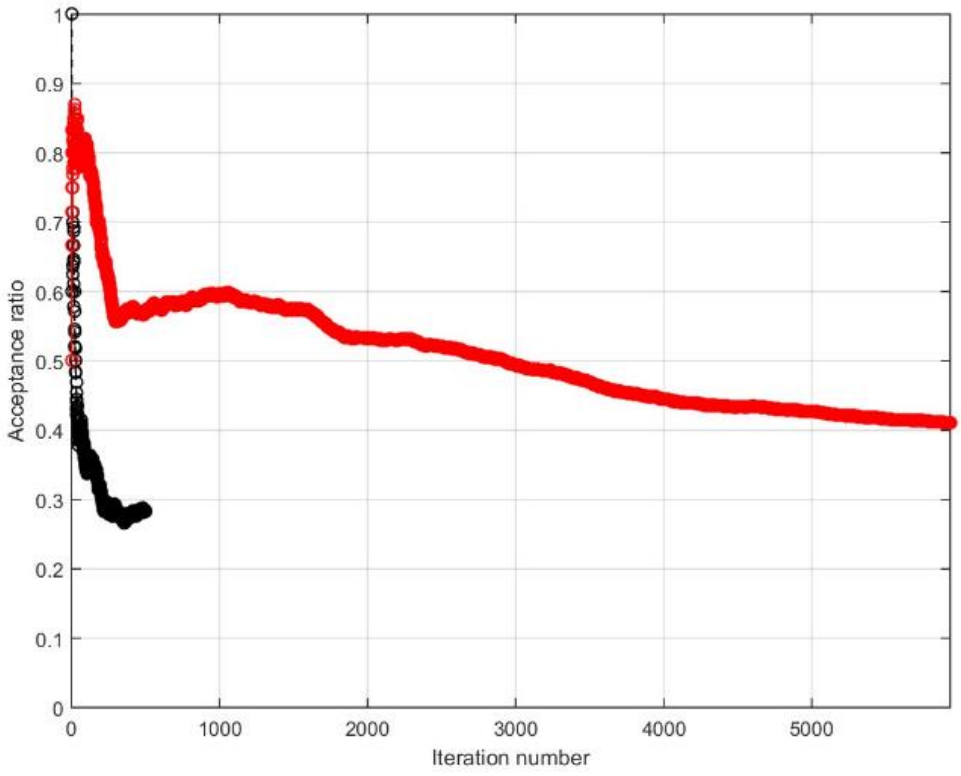

Fig. 72—Comparing the acceptance ratio curves for the multi-level EnKF and MCMC cases at the 12th assimilation cycle (1080 days): one-stage MCMC (black) and two-stage MCMC (red).

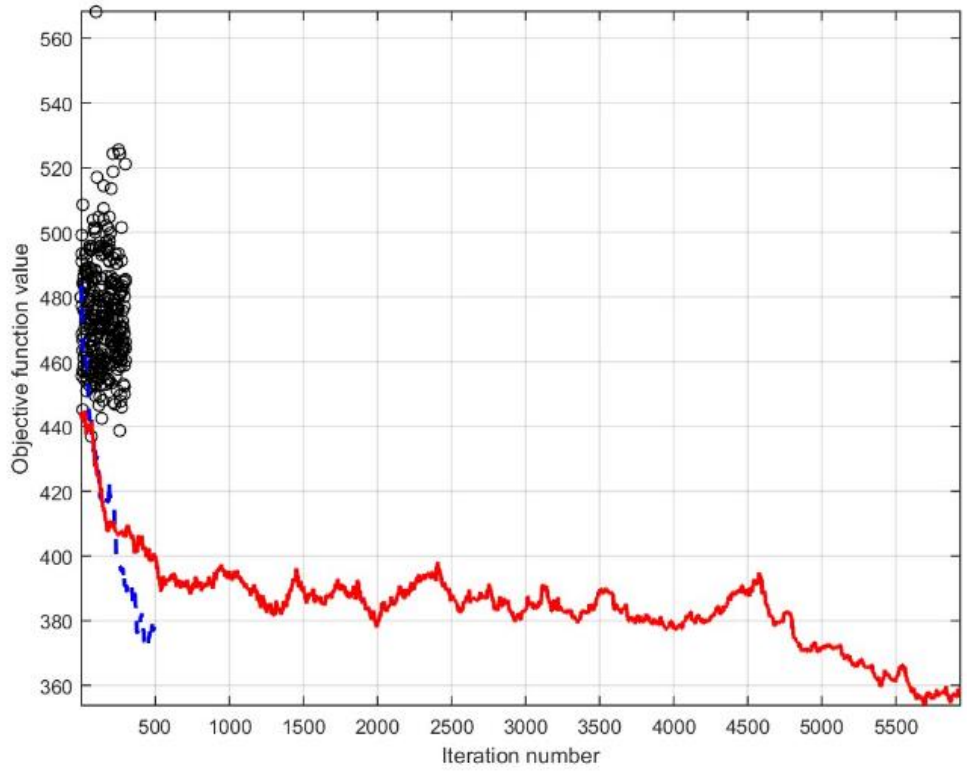

Fig. 73—Comparing the posterior objective function values at the 12th assimilation cycle (1080 days) for the EnKF case (black circles), multi-level EnKF/one-stage MCMC case (blue dashed line), and the multi-level EnKF/two-stage MCMC case (red solid line).

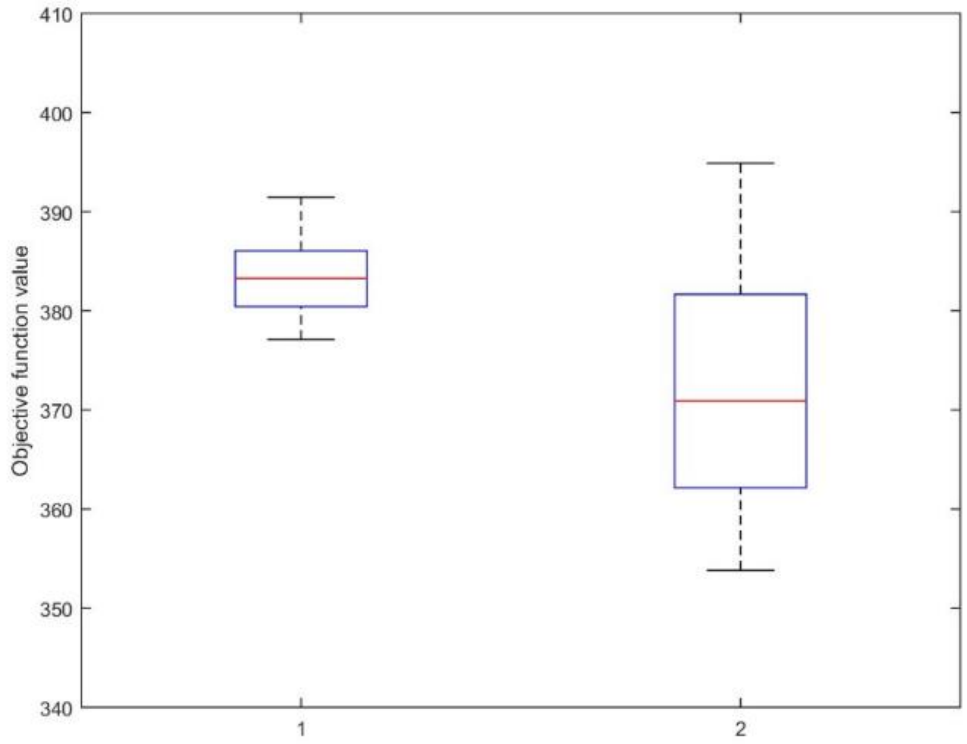

Fig. 74—Box plot for the objective function values for the 1st and the 2nd halves of the two-stage MCMC chain at 1080 days: 50th percentile (red line), 25th and 75th percentiles (blue box), the minimum and maximum percentiles (black lines) and the true case (green dashed line).

The estimated production profiles at 1080 days **(Fig. 75-78)** provides similar conclusions as in the previous section. The ranges are becoming narrower as more observed measurements are assimilated and the means are getting closer to the true solution.

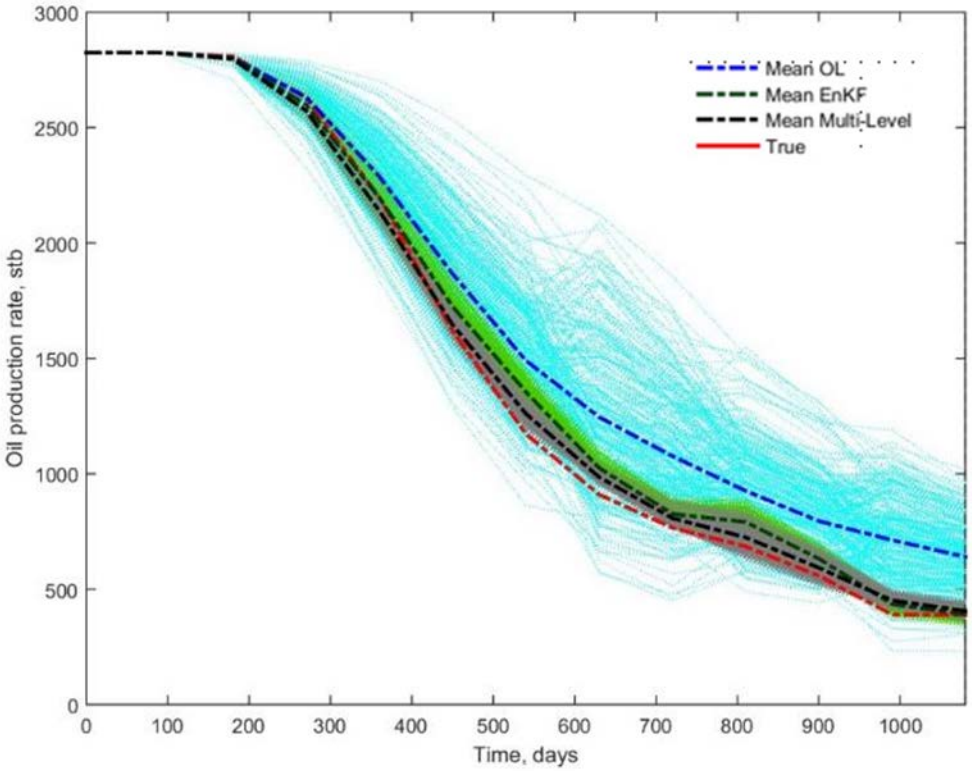

Fig. 75—Oil production rate estimates after the 12th assimilation cycle: the open-loop estimates (cyan), estimates based on EnKF update (light green), estimates based on multi-level EnKF/two-stage MCMC sampling (grey), the mean of the open-loop distribution (blue), the mean of the EnKF distribution (green), the mean of the multi-level EnKF/two-stage MCMC (black) and the true case (red).

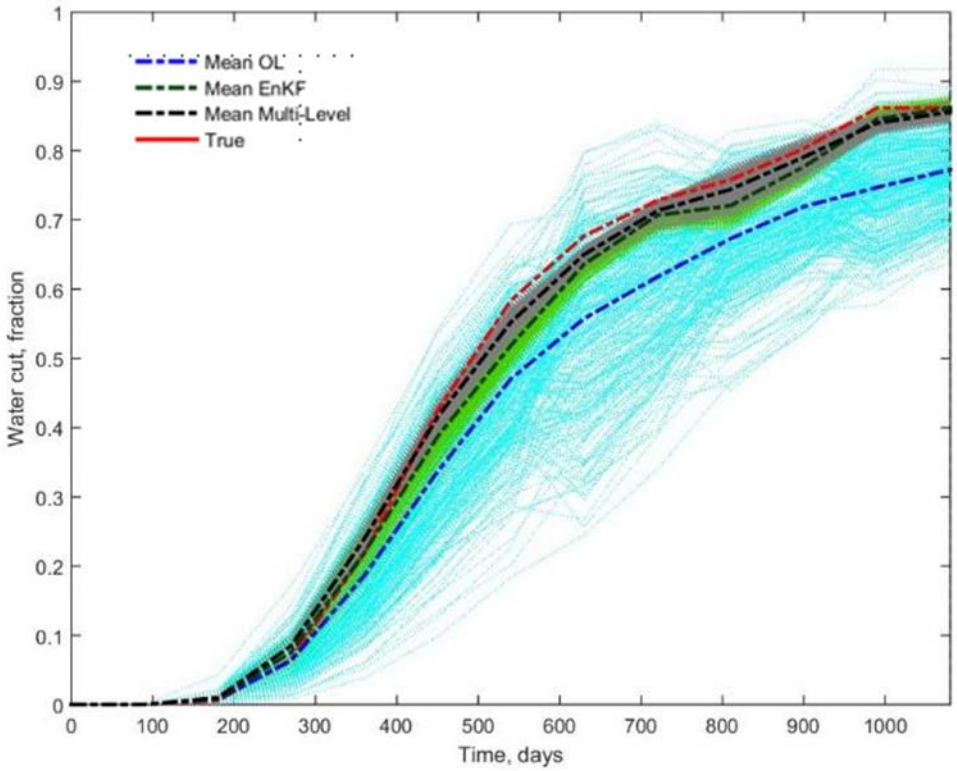

Fig. 76—Water cut estimates after the 12th assimilation cycle: the open-loop estimates (cyan), estimates based on EnKF update (light green), estimates based on multi-level EnKF/two-stage MCMC sampling (grey), the mean of the open-loop distribution (blue), the mean of the EnKF distribution (green), the mean of the multi-level EnKF/two-stage MCMC (black) and the true case (red).

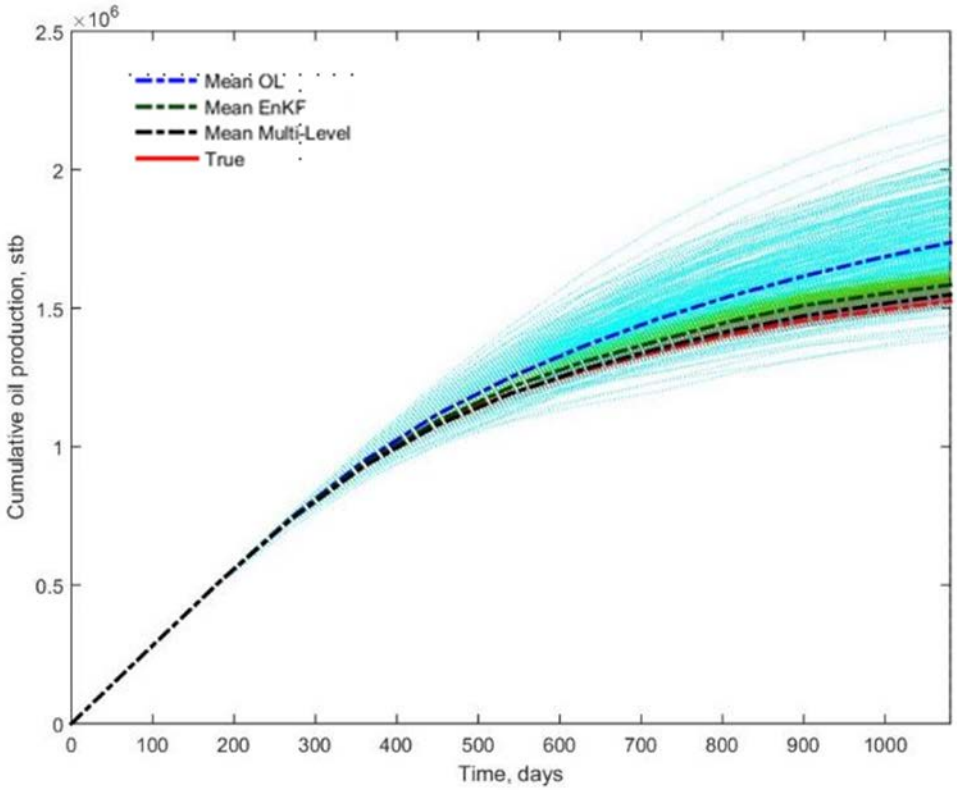

Fig. 77—Cumulative oil production estimates after the 12th assimilation cycle: the open-loop estimates (cyan), estimates based on EnKF update (light green), estimates based on multi-level EnKF/two-stage MCMC sampling (grey), the mean of the open-loop distribution (blue), the mean of the EnKF distribution (green), the mean of the multi-level EnKF/two-stage MCMC (black) and the true case (red).

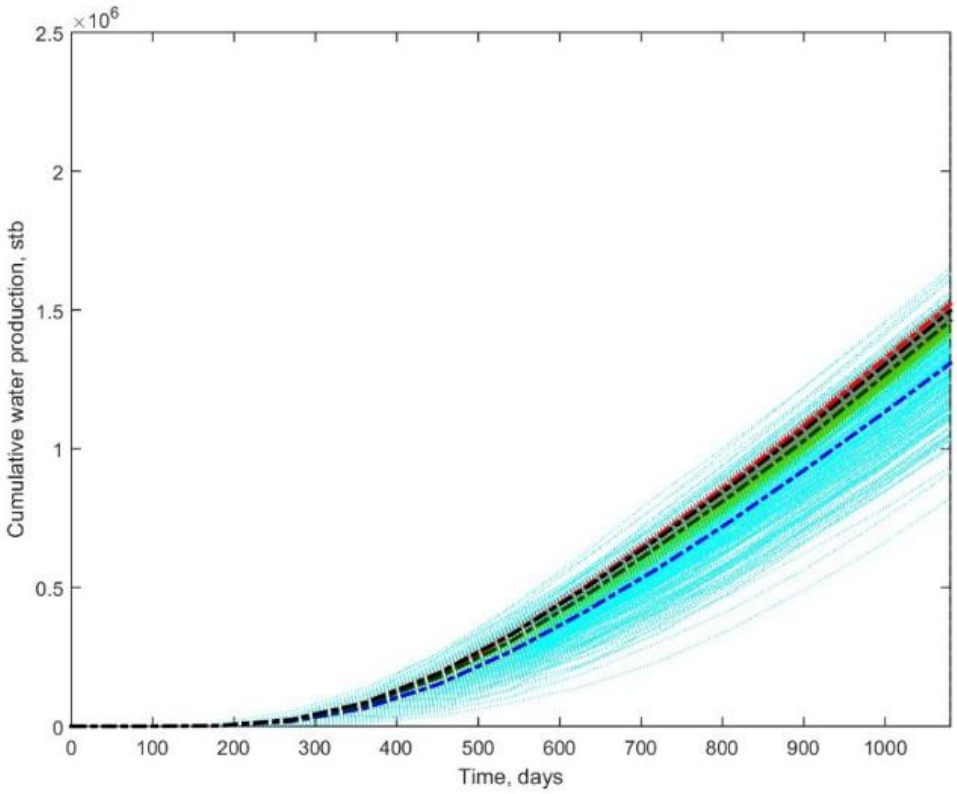

Fig. 78—Cumulative water production estimates after the 12th assimilation cycle: the open-loop estimates (cyan), estimates based on EnKF update (light green), estimates based on multi-level EnKF/two-stage MCMC sampling (grey), the mean of the open-loop distribution (blue), the mean of the EnKF (green), the mean of the multi-level EnKF/two-stage MCMC (black) and the true case (red).

As in the previous section, the estimated cumulative production **(Fig. 79 and 80)** show the multi-level case to bracket the true solution while the EnKF does not. Although the experiment has reached its end and there are no more forecasts, these results show an improvement in the estimation of the uncertainty of production profiles as more data are assimilated. It also suggests that the multi-level algorithm is improving the estimation of EnKF.

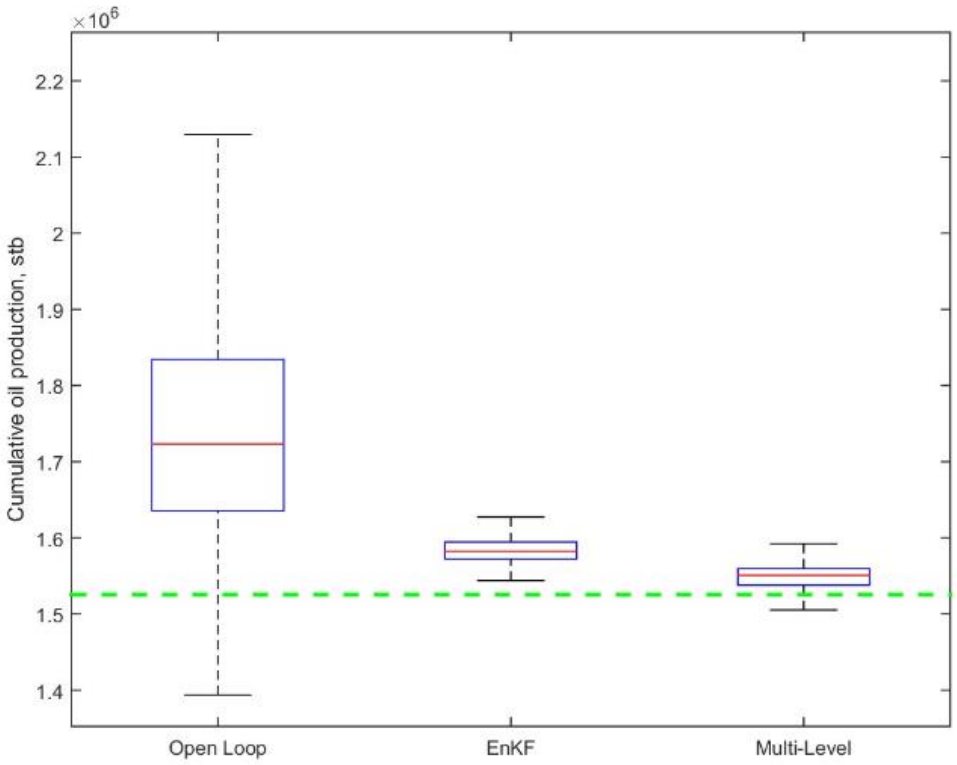

Fig. 79—Box plots for cumulative oil production at the end of the total simulation time (1080 days) estimated at the end of the 12th assimilation cycle (1080 days): 50th percentile (red line), 25th and 75th percentiles (blue box), the minimum and maximum percentiles (black lines) and the true case (green dashed line).

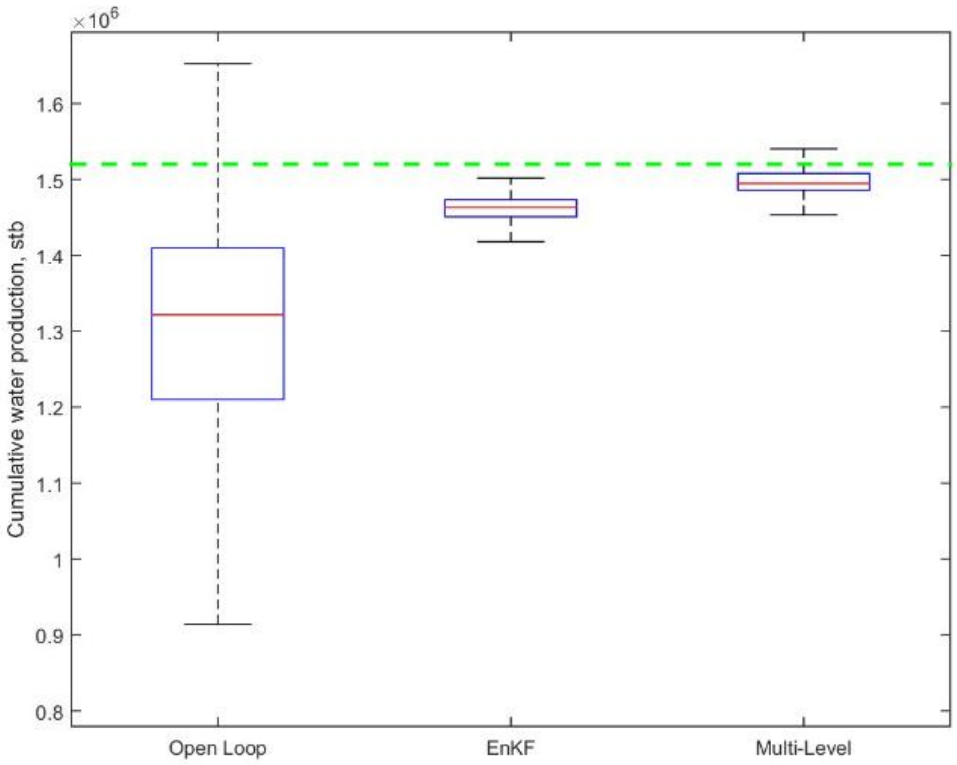

Fig. 80—Box plots for cumulative water production at the end of the total simulation time (1080 days) estimated at the end of the 12th assimilation cycle (1080 days): 50th percentile (red line), 25th and 75th percentiles (blue box), the minimum and maximum percentiles (black lines) and the true case (green dashed line).

5.7.5 Comparison of Results

In this section, results of the four EnKF/two-stage MCMC chains presented earlier are compared to EnKF in terms of estimates of the posterior permeability field and estimates of the production forecasts.

5.7.5.1 Permeability Field Posterior Estimates

Fig. 81 and 82 show the mean estimates and the mean error estimates after the third, sixth, ninth and twelfth assimilation cycles for EnKF updating and multi-level

EnKF/two-stage MCMC sampling. As mentioned earlier, the mean estimates capture the general trend and orientation of the two channels as early as the first update. The rates of change in the mean estimates drop quickly with time. In fact, the last two updates of EnKF and EnKF/two-stage MCMC show very close mean estimates.

The mean error estimates (Fig. 82) show reduction in error initially when compared with the initial ensemble (Fig. 34), particularly around the main two channels. The most noticeable difference in the mean error estimation between the EnKF case and the MCMC cases is found in the middle of the log-permeability field (i.e., the unswept region of the field). Because there is no strong correlation between the gridblock permeability values in this region and observed measurements, the effect of spurious correlations accumulates and the EnKF estimate errors become more pronounced. The use of MCMC at the second level seems to improve the estimation in this area. This suggests that using MCMC sampling can help remedy the effects of spurious correlations that might be observed when EnKF updating is used.

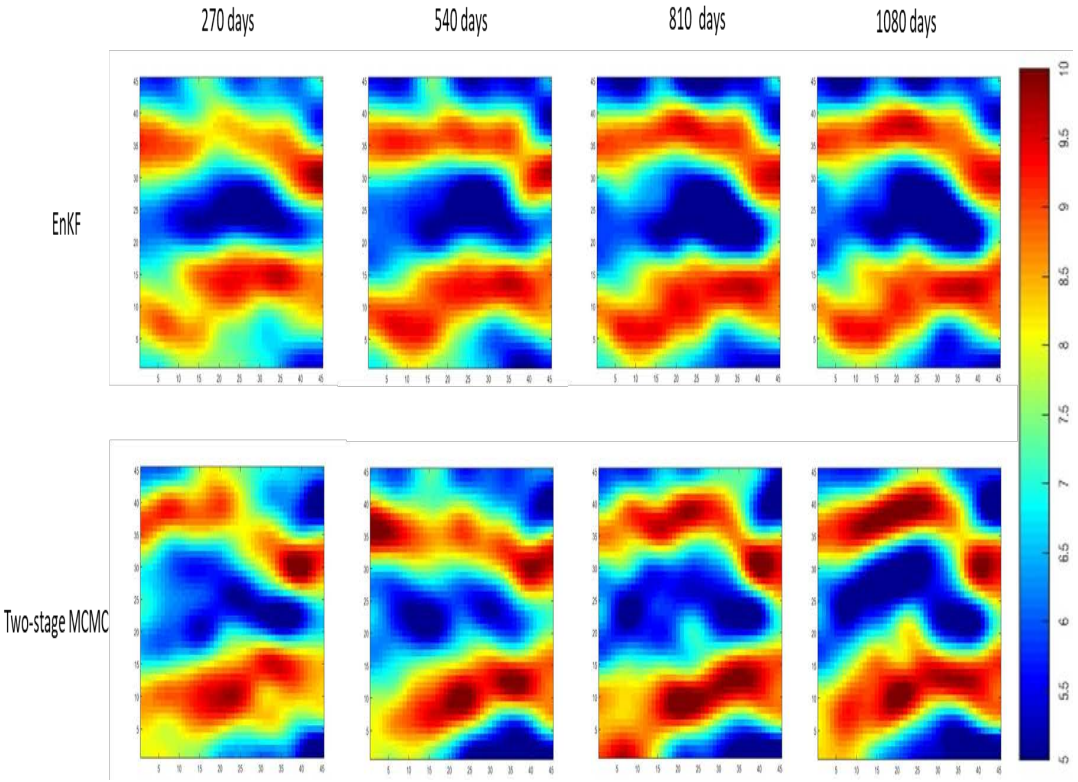

Fig. 81—The posterior mean estimates for the log-permeability field (log-mD) for the EnKF updates (top row) and the multi-level EnKF/two-stage MCMC (bottom row) at the end of the 3rd (1st column), 6th (2nd column), 9th (3rd column) and 12th (4th column) assimilation cycles.

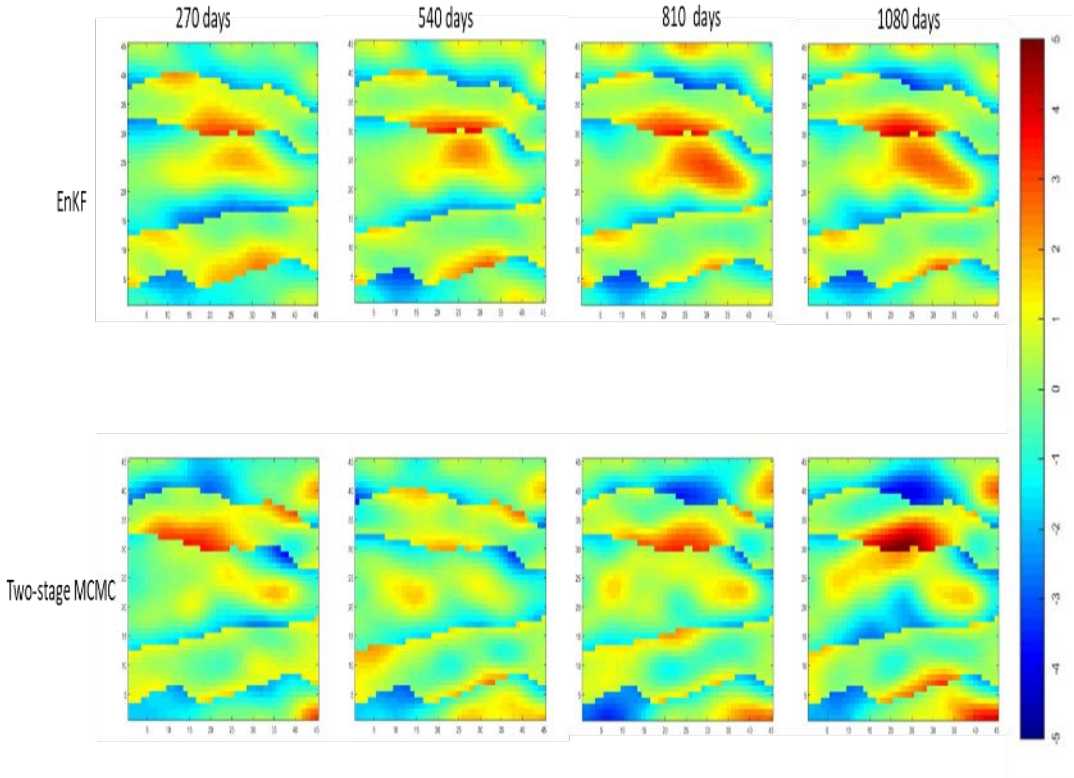

Fig. 82—The posterior mean error estimates for the log-permeability field (log-mD) for the EnKF updates (1st row) and the multi-level EnKF/two-stage MCMC (bottom row) at the end of the 3rd (1st column), 6th (2nd column), 9th (3rd column) and 12th (4th column) assimilation cycles.

Fig. 83 presents the standard deviation estimates for the gridblock log-permeability values at the end of the third, sixth, ninth and twelfth assimilation cycles for EnKF updating and multi-level/two-stage MCMC sampling. The maps show continuous reduction in uncertainty as more data are assimilated. The locations where most of the uncertainty reduction occurs correlates with where the data are located (i.e., horizontal wells along the left and right edges of the field) and along the flow paths of the field (i.e., along the channels). Also, the standard deviations at the right edge (i.e., along the producer

well) are less than the left edge. This is because the amount of the data collected from the producer is twice that collected from the injector. The MCMC cases show more reduction in uncertainty compared to the EnKF cases, particularly in the middle, unswept region of the model.

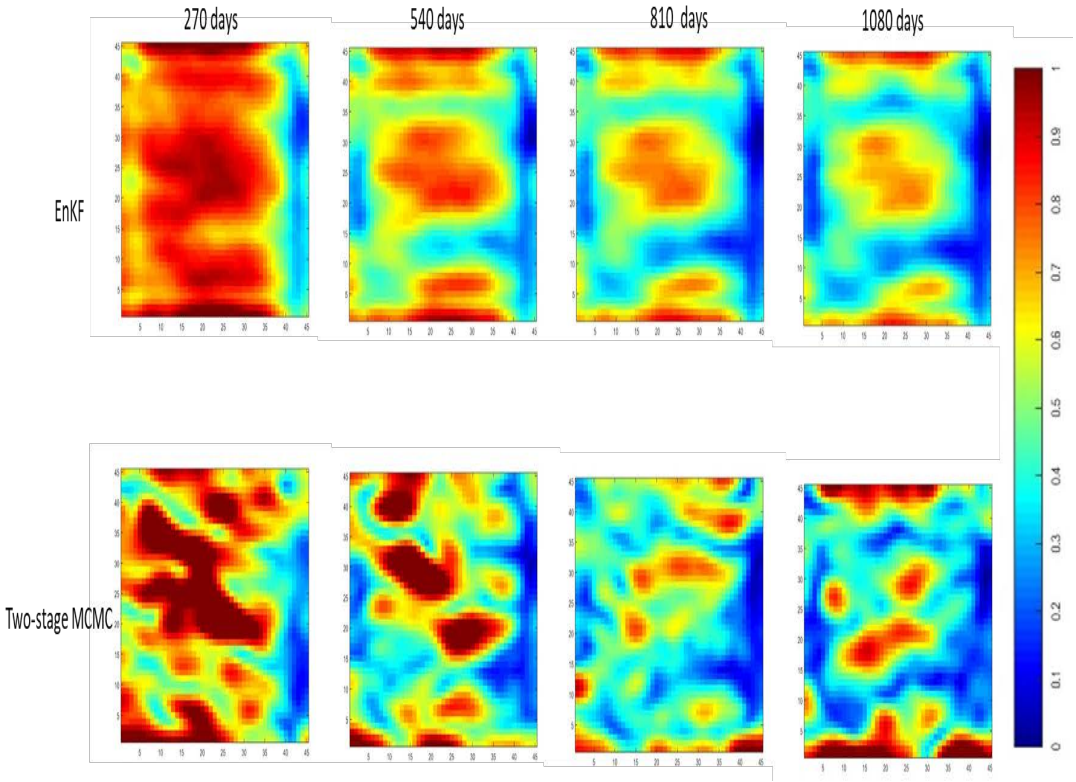

Fig. 83—The posterior standard deviation estimates for the log-permeability field (log-mD) for the EnKF updates (1st row), multi-level EnKF/one-stage MCMC (middle row), and the multi-level EnKF/two-stage MCMC (bottom row) at the end of the 3rd (1st column), 6th (2nd column), 9th (3rd column) and 12th (4th column) assimilation cycles

5.7.5.2 Production Forecast Estimates

Fig. 84 and 85 compares the distribution of cumulative oil and water production generated by the initial ensemble (open-loop), updated models after the third assimilation cycle (270 days of production), updated models after the sixth assimilation cycle (540 days of production), updated models after the ninth assimilation cycle (810 days of production), and updated models after the twelfth assimilation cycle (1080 days). The figures show that the true solution is bracketed by the initial ensemble (open-loop case) of cumulative oil and water production, although the uncertainty is large. The distribution range decreases significantly at the third and sixth assimilation cycles. Then, it does not appear to change significantly after that. Although the true solution is not bracketed at the third assimilation cycle, the distribution keeps shifting toward the direction of the true solution as more data are assimilated. As mentioned in previous sections, the fact that the true solution is not bracketed by the distribution is indicative of underestimation of uncertainty. This indicates that number of samples generated was not large enough to cover the entire space of the posterior density function. This is a result of the large dimensionality of the posterior function and the complex nature of the inverse problem in reservoir simulation (i.e., involves solving a system of highly non-linear flow equations). Also, bracketing the true solution at later times does not necessarily mean absence of bias or overconfidence in the estimation. Nevertheless, it indicates that uncertainty estimation improves as more data are assimilated.

It is also worth noting here that one should not make conclusions regarding the quality of posterior estimation in the inverse problem in reservoir simulation solely by

comparing production forecasts. The solution of the inverse problem lies in the parameter space (e.g., the permeability field in this experiment). Production forecasts are also strongly influenced by the control input of the problem. For example, the comparison of production forecasts could change significantly (although all methods are using the same prior and likelihood definitions) if a new well is simulated in the unswept oil zones (middle of the field) in the example provided in this section due to differences in the estimated permeability field in this region (Figs. 81-83).

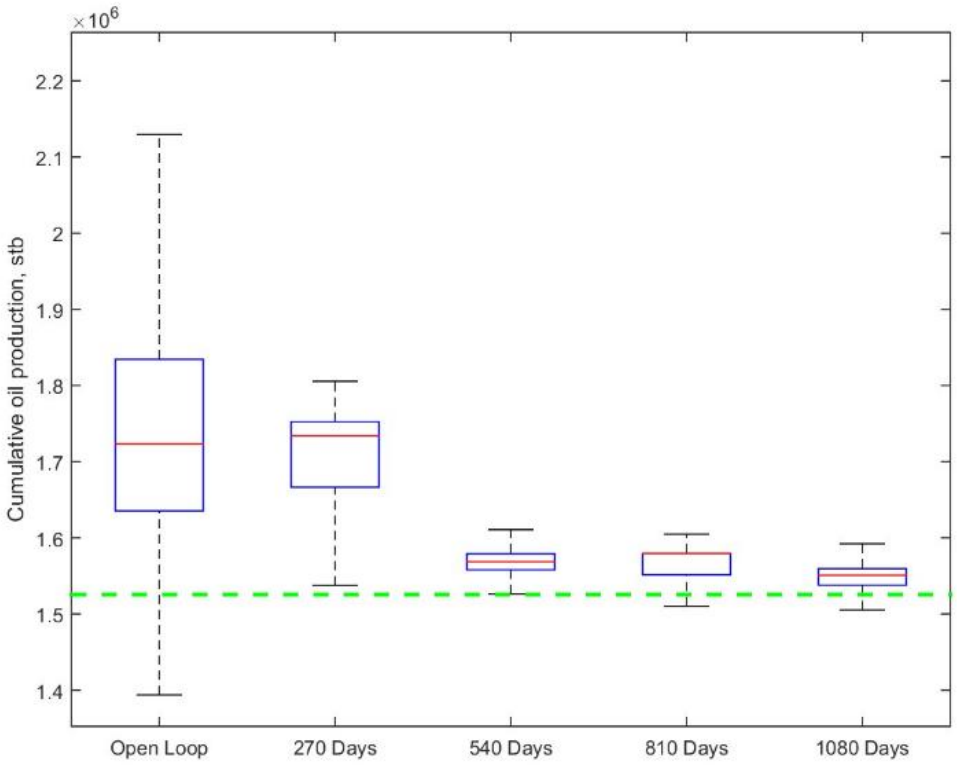

Fig. 84—Forecasted cumulative oil production at the end of the total simulation time using multi-level EnKF/two-stage MCMC sampling at different assimilation cycles: 50th percentile (red line), 25th and 75th percentiles (blue box), the minimum and maximum percentiles (black lines) and the true case (green dashed line).

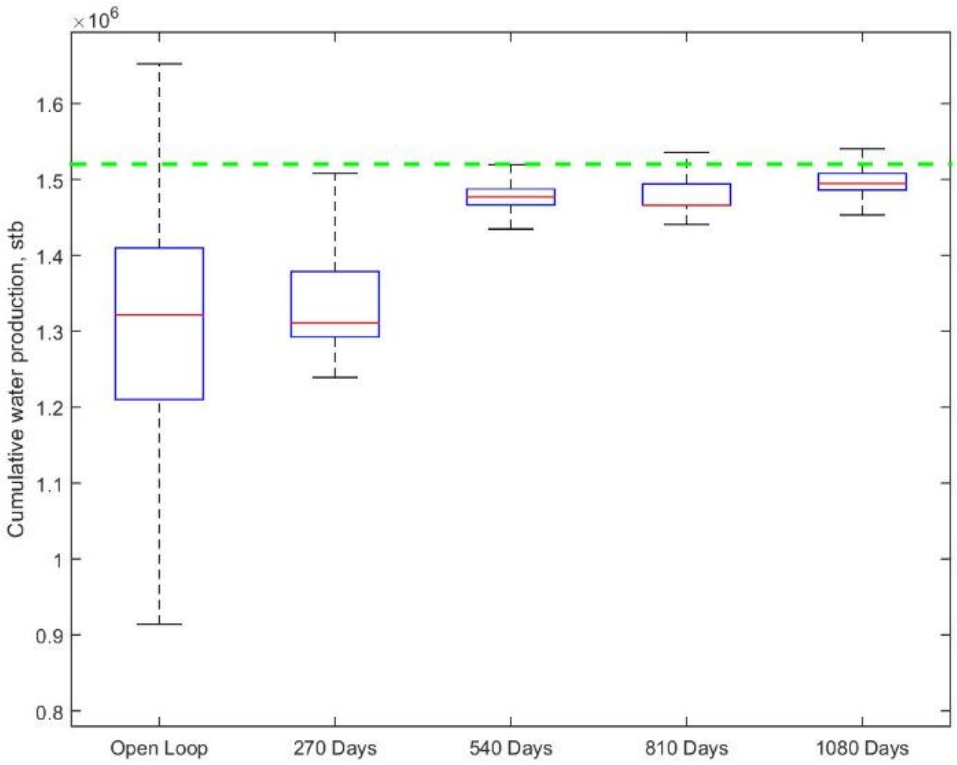

Fig. 85—Forecasted cumulative water production at the end of the total simulation time using multi-level EnKF/two-stage MCMC sampling at different assimilation cycles: 50th percentile (red line), 25th and 75th percentiles (blue box), the minimum and maximum percentiles (black lines) and the true case (green dashed line).

6. DISCUSSION OF RESULTS

It is well established (Sec. 1.1.3) that CLRM approach is a better fit to the problem of maximizing the overall value of a petroleum asset than a reactive or periodic approach. Research suggests that utilizing a closed-loop approach can achieve better recoveries and increase NPVs of petroleum assets. A major requirement to any CLRM strategy is a continuous-model-updating-and-uncertainty-quantification procedure that can provide reliable estimates of the model parameters. It is equally important that this procedure is computationally feasible and can be adapted to the operations and decision cycles. These requirements are addressed well by combining elements of EnKF for computational efficiency and MCMC methods for sampling robustness.

In this section, issues related to the implementation of this method are discussed. The following subsections address the capability of EnKF to handle channelized reservoir characterization, underestimation of EnKF posterior covariance, the differences between the combined EnKF-MCMC approach (Emerick and Reynolds 2011) and the new multi-level EnKF-MCMC approach introduced in this dissertation, the benefits of utilizing the continuous modeling approach, and implementation of the proposed procedure as part of a CLRM strategy.

6.1 EnKF Posterior Estimates for Channelized Reservoir Characterization

Some of the previous work that implemented EnKF in a channelized reservoir characterization (two-facies system) were capable of capturing the major trends in permeability fairly quickly (Brouwer et al. 2004; Jafarpour and McLaughlin 2009b). Emerick and Reynolds (2011) showed that even when EnKF estimates appear reasonable, history matches obtained with EnKF are worse than those obtained by gradient methods or MCMC. In this work, results are consistent with these conclusions (refer to Figs. 46, 55, 64 and 73 for objective-function comparison and Fig. 82 for mean-error-estimate comparison).

Fig. 86 shows the initial and final (after EnKF updating) log-permeability field for a random initial realization (R10). The maps show that EnKF changed the log-permeability field and reoriented the channels in the true direction, thus indicating that EnKF is capable of handling complex geological descriptions, as in this case of channelized reservoir characterization.

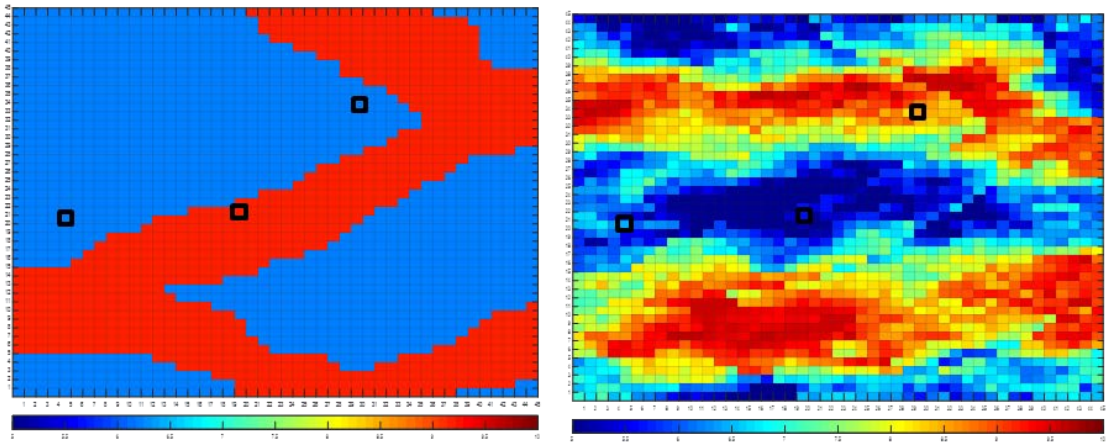

Fig. 86—Initial (left) and final (right) log-permeability field (log-mD) for a random initial realization (R10) with gridblock A (left on the map), gridblock B (center of the map), and gridblock C (upper right on the map) outlined (bold black square).

The histograms in **Fig. 87** quantify distributions of log-permeability fields for the R10 prior realization after the first, second, fourth, sixth, eighth, tenth, and twelfth updates. The histograms show that, initially, 60% of the permeability field for this realization is in the non-channel facies (6 log-mD) while 40% is in the channel facies (9 log-mD). It is worth noting that the true distribution is also composed of 60% non-channel facies and 40% channel facies while the initial ensemble is, on average, 70% non-channel facies and 30% channel facies. After the parameterization and during the EnKF updating process, the permeability values for the R10 prior realization get more dispersed. Although the later distributions do not honor the bi-modal 60%-non-channel/40%-channel true distribution, on the other hand, the histograms do not follow a Gaussian trend that averages out channel and non-channel facies either.

Fig. 88 shows the changes in the log-permeability values for gridblocks A, B, and C, outlined in Fig. 86. In the initial ensemble, the permeability field is composed of two discrete values: 6 log-mD for the no-channel facies and 9 log-mD for the channel facies. Gridblock A starts in the no-channel facies at a value of approximately 6 log-mD and during updating continues to be in the no-channel facies, ending with a value slightly less than 6 log-mD (true value is 6 log-mD). Gridblock B starts in the channel facies at a value of approximately 9 log-mD and during updating gradually changes to the no-channel facies at a value slightly larger than 6 log-mD (true value is 6 log-mD). Gridblock C starts in the no-channel facies at a value of approximately 6 log-mD and during updating changes to the channel facies, ending with a value of approximately 8 log-mD (true value is 9 log-mD). The values obtained by EnKF updating for these three gridblocks reasonably agree with the values at their respective locations on the true permeability field (Fig. 23).

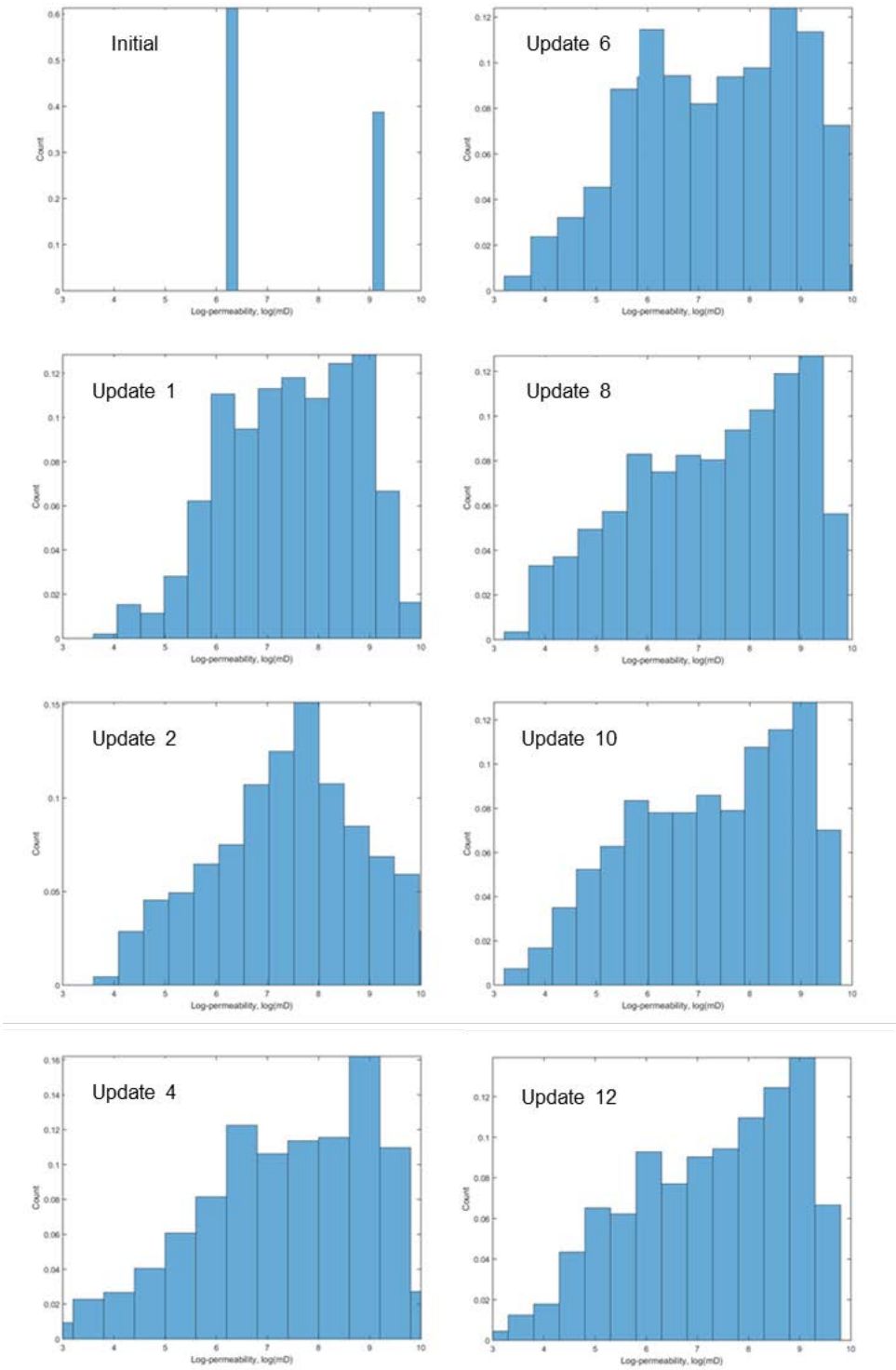

Fig. 87—Histograms showing the distribution of the log-permeability field for the R10 realization at the initial, 1st update, 2nd update, 4th update, 6th update, 8th update, 10th update and 12th update.

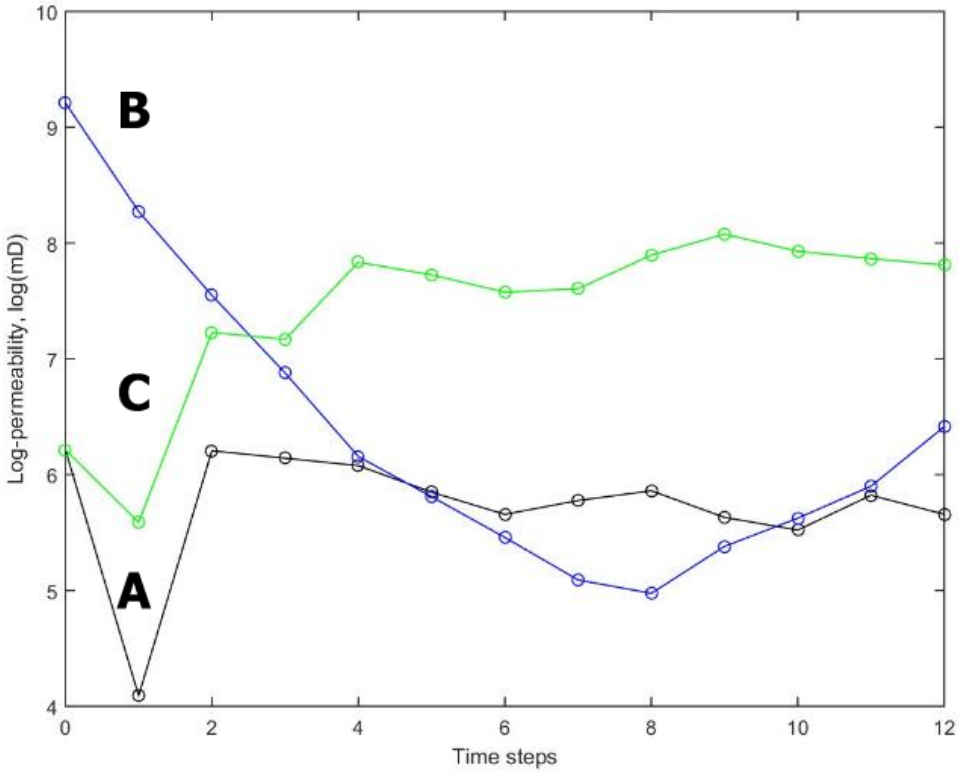

Fig. 88—Log-permeability updates for gridblock A (black), gridblock B (blue), and gridblock C (green) of realization R10.

Fig. 89 presents the log-permeability histograms for the three gridblocks (A, B, and C) outlined in Fig. 86 across all realizations for the initial ensemble, the ensemble after the first update, and the ensemble after the last update. All the histograms show, initially, a distribution that approximately matches the distribution of the facies at the training image—30% channel and 70% no-channel facies. At the first update, the distribution is more spread with a peak close to the no-channel value. Later on, the distribution narrows down and shifts toward one of the two main facies' values. The

distribution of the last update for these gridblocks is in accordance with their locations on or off the channels in reference to the true permeability field.

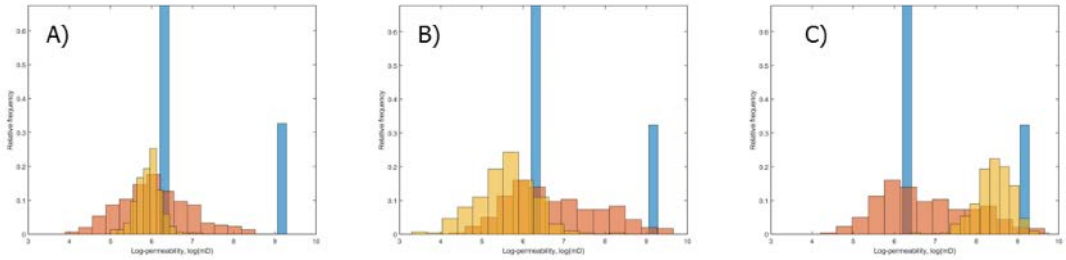

Fig. 89—Histograms for the log-permeability field of gridblocks A, B, and C across all realizations for the initial ensemble (blue), 1st update (brown) and final update (yellow).

6.2 Underestimation of EnKF Posterior Covariance

In the multi-level EnKF-MCMC approach, the covariance of the EnKF posterior is used to propose new realizations. This means that any proposed sample for MCMC lies in the space spanned by the EnKF posterior covariance or, in other words, any proposed realization is a linear combination of the EnKF updated ensemble. This implies that if the variability in the ensemble realizations updated through EnKF is less than the actual variability (i.e., the covariance matrix is underestimating the uncertainty), this would negatively impact the posterior distribution of the multi-level method. This also highlights the dependency of this process on the initial ensemble.

The MCMC M-H algorithm is known, theoretically, to sample the posterior correctly as the number of iterations approaches infinity. In our application, it is not

feasible to perform such a test and compare to MCMC sampling using EnKF posterior covariance. In this work, using EnKF posterior covariance at the MCMC level has shown an improvement in the sampling quality over EnKF and standard MCMC random-walk perturbation methods. This is illustrated by the reduction in the posterior objective function values (Figs. 15, 16, 44, 46, 55, 64 and 73) and reduction in the mean error estimates of the posterior relative to the truth case (Figs. 19, 34, 35, 36, 37 and 82).

This is not to suggest that the multi-level EnKF-MCMC approach samples the posterior exactly and produces variability that represents the actual posterior variability. Clearly, the requirements to estimate the posterior exactly using MCMC (i.e., generating a chain with the number of iterations approaching infinity) cannot be satisfied in practical applications. In fact, Fig. 84 shows that, even after 6000 iterations, the uncertainty of the sampled distribution at 270 days is underestimated (i.e., the true solution is not bracketed). However, as mentioned above, the results show only that the multi-level EnKF-MCMC approach used here improves the posterior estimation relative to EnKF and standard MCMC random-walk perturbation methods with a fewer number of iterations.

6.3 Combined EnKF-MCMC vs. Multi-Level EnKF-MCMC Approach

In the combined EnKF-MCMC approach proposed by Emerick and Reynolds (2010,2011), MCMC posterior sampling is based on an approximated likelihood function. The approximation uses estimated model parameters and states (e.g., gridblock pressures and saturations) to calculate observed measurements rather than actual reservoir simulation output. The estimation of model parameters and states are produced by

sampling a joint Gaussian distribution. By doing so, it is implicitly assumed that the relationship between model parameters and states is approximately linear. This is a strong assumption to maintain when dealing with reservoir simulation models. Although the sampled realizations are later re-run using reservoir simulation to generate accurate well profiles, the fact remains that these realizations were sampled using an approximated evaluation of the likelihood function. This approximation impacts the quality of the estimated posterior and may introduce biases and underestimation of uncertainty in the sampling process.

In the multi-level approach proposed here, EnKF is used to define the proposal distribution of MCMC rather than using a proposal distribution that is based on random-walk perturbation methods. Also, the approximated evaluation of the likelihood function is used only in the first stage of MCMC (i.e., filtering stage), while an exact calculation of the likelihood function is used in the second stage. Both measures (i.e., using EnKF-generated posterior for the proposal distribution and approximating the likelihood function at the first stage of MCMC) do not violate any of the assumptions required to accurately sample the posterior distribution. In fact, it can be shown that the two-stage Metropolis-Hasting algorithm used in this research does not violate the reversibility condition required for MCMC to generate accurate sampling (Appendix A.2).

It is worth noting that this method of approximating the likelihood function at the first stage of MCMC, although theoretically sound, can greatly affect the proposal distribution. Effectively, if the approximation of the likelihood function is not accurate enough, the resulting two-stage proposal distribution will be negatively affected and might

significantly increase burn-in size, slow down convergence rate and result in a poorly-mixed chain. On the contrary, if the approximation is reasonably accurate, the resulting two-stage proposal distribution improves and can lead to smaller burn-in size, better chain-mixing and higher acceptance rates.

It is difficult to tell beforehand if such an approximation would be accurate enough or result in a better choice of proposal. Multi-level one-stage and two-stage chains can be compared, and if the approximation is shown to produce better results, then the two-stage approach can be used.

6.4 Benefits of Using the Continuous Approach

As been previously stated, solving the inverse problem in a continuous manner, as opposed to one-time studies, allocates more computing time to investigating the parameter space and can lead to improved sampling of the posterior. One main challenge to this concept, however, is that the definition of the posterior changes every time new measurements are observed. Theoretically, the posterior distribution from an update can be used as the new prior distribution for the subsequent update. Because of the high dimensionality and non-linearity of the inverse problem in reservoir simulation, the form of the posterior distribution is not known and the number of samples collected are not sufficient to fully characterize the distribution. As mentioned earlier, Fig. 84 clearly shows that the posterior is underestimated at 270 days—it is not bracketing the true solution (i.e., the true solution is outside the P0-P100 ranges). This means that this posterior effectively associates a probability of zero to the true solution. Now, if this posterior was used to

define the prior for the next assimilation cycle, the resulting posterior will be guaranteed to not bracket the true solution because the prior distribution assigns a probability of zero to the truth case. Consequently, using a posterior distribution estimated in this way to define the prior for the succeeding update can lead to invalid posterior sampling, major biases and underestimation of uncertainty.

To fully realize the benefits of the continuous approach, a way must be found to combine samples associated with different posteriors and still produce sound statistical inference. Although the issue of changing posterior definitions was not addressed, this research utilized and benefited from the continuous approach in the following ways:

- The EnKF posterior covariance, which is being updated continuously and incorporates all the information contained in the observed measurements, is used to guide the search within the parameter space.
- Because of the multi-level approach implemented here, the MCMC sampling can be spread over a longer period of time (i.e., while EnKF is used on to perform updates on high frequency cycles). Consequently, more iterations can be performed, and improved estimates can be realized.

6.5 Estimated Production Forecast

The production forecast distributions generated by this approach continue to narrow and shift toward the true solution as more observations are assimilated. Although this is an indication that estimates of production forecasts are improving, it does not

guarantee unbiasedness nor full estimation of uncertainty. In fact, Figs. 84 and 85 show clearly that the update at 270 days is underestimating the uncertainty of the posterior because the truth case is not bracketed by the estimated forecast distributions (i.e., P0-P100 ranges). This suggests that at this earlier stage of the model updating process, 6000 iterations did not produce a chain that is mixed enough to fully estimate the posterior distribution. The estimation can be improved by running the chain longer or improving the EnKF covariance estimation (i.e., proposal distribution).

Because using this approach generates multiple distributions of production forecasts over time, the relationship between these forecasts and actual field production can be examined. Biases and underestimation of uncertainty in production forecasts can then be measured (Alarfaj and McVay 2016). Further, external calibration methods can be used to improve these estimates (McVay et al. 2005).

6.6 Multi-Level EnKF-MCMC Operational Advantage

The advantage of this multi-level EnKF-MCMC approach over most other methods in the literature is that it provides two levels of updating and uncertainty quantification. The first level is more frequent but less rigorous, and the second level is less frequent but more robust. Models produced by the EnKF first-level updating can be used to optimize oil production rate, maintain production schedule, or reduce water cut in the short-term by investigating BHP configuration or water injection allocation. The MCMC second-level updates can be used to optimize overall recovery or increase NPV by investigating drive mechanisms or infill drilling

7. CONCLUSIONS AND RECOMMENDATIONS

7.1 Summary of Conclusions

- Using an EnKF posterior covariance in the proposal selection of MCMC significantly reduced the burn-in size, increased the convergence rate and improved chain mixing, in comparison to the standard MCMC random-walk perturbation method. Consequently, this allows for sampling from regions of higher probability and covers more of the posterior distribution (i.e., improves posterior sampling) at a lower computational cost.
- Using a two-stage approach to multi-level EnKF-MCMC sampling leads to significant increase of the acceptance rate at the same level of proposal variance. This leads to increased efficiency of the process and enlarges the effective sample size, as wider regions of the posterior are visited at the same number of iterations, without compromising chain mixing.
- Although both EnKF and multi-level EnKF-MCMC methods generated forecast distributions that narrow and shift toward the true solution as more data are assimilated, the multi-level approach produced narrower distributions and improved the production forecast estimation, relative to EnKF (i.e., shifted more toward the true solution and in some instances bracketed the true solution when EnKF did not).
- The Multi-Level EnKF/Two-Stage MCMC approach proposed in this dissertation is not guaranteed to fully sample the posterior distribution. In fact, it

underestimated the uncertainty in some cases. Results suggest, however, that as more data are assimilated, the posterior estimation improves and brackets the true solution.

7.2 Recommendations for Future Work

Additional areas for improvement to this work should focus on utilizing the Multi-Level EnKF/Two-Stage MCMC procedure in the CLRM approach and testing the application of this method in real-time applications. Some of these areas for improvement include:

1. Integrating this procedure with multi-level optimization algorithms to produce a full CLRM approach.
2. Testing this procedure in real-field applications.
3. Investigating ways to improve posterior estimation and reduce or eliminate underestimation of uncertainty. Examples of possible areas to improve posterior estimation are:
    - Improving the EnKF covariance estimation and creation of the initial ensemble (i.e., proposal distribution).
    - Optimizing proposal tuning parameters (e.g., covariance scaling factor) to speed up convergence and reduce burn-in size.
    - Testing this algorithm with alternative ways of approximating the likelihood function at the first stage of MCMC. In particular,

approximations based on streamlines sensitivity calculation or reduced-order methods seem to be promising to investigate.

4. Testing this procedure on different reservoir characterization problems.
5. Assessing the biases and quantification of the uncertainty in production forecasts, and using external calibration methods to improve estimates of production forecasts.

NOMENCLATURE

A	Transition matrix
AM	Adaptive Metropolis
AP	Adaptive Proposal
BFGS	Broyden-Fletcher-Goldfarb-Shanno
bpd	Barrel per day
BHP	Bottom hole pressure
C	Covariance
d_{obs}	Observed measurements vector
CLRM	Closed-loop reservoir management
DCT	Discrete cosine transform
EnKF	Ensemble Kalman-filter
erf	Error function
$f_\theta(y)$	Likelihood function
$f(y,\theta)$	Joint probability function for the data and uncertainty parameter
GA	Genetic algorithms
$g(\theta)$	Reservoir response
I	Identity matrix
k	Number of reduced dimensions
K	Kalman gain
$H(\cdot)$	Hessian matrix

$L(\cdot)$	Likelihood function
LBFGS	Low-memory Broyden-Fletcher-Goldfarb-Shanno
m	Model parameters
$m(y)$	Marginal distribution of the data
MAP	Maximum a posteriori
MCMC	Markov chain Monte Carlo
M-H	Metropolis-Hasting algorithm
N	Full number of dimensions
N_{d}	Number of data points
NPV	Net present value
$O(\cdot)$	Objective function value
psi	pounds per square inch
PSO	Particle Swarm Optimization
PV	Pore volume
$P(X,Y)$	Transition probability from X to Y
$q(.,.)$	Proposal density
$r(.)$	Marginal distribution
RML	Randomized maximum likelihood
SNESIM	Single normal equation algorithm
stb	Stock tank barrel
S_w	Water saturation
S_w^*	Transformed water saturation

U	Uniform distribution
v	Measurement error
w	Model error
y	Augmented parameter-state vector
X	State
$\hat{z}$	Random Gaussian variable
$\alpha(.,.)$	Acceptance ratio
θ	Uncertainty parameter vector
θ^*	Proposed sample vector
$\pi(\cdot)$	Probability density function
σ^2	Scaling factor
Φ	Transformation matrix
$\nabla g(\cdot)$	Sensitivity coefficients
$\nabla O(\cdot)$	Gradient of the objective function
δ	Delta function

Subscripts

D	Observed measurement
n	Assimilation cycle number
M	Model parameters
t	Time step
x	State
ϵ	Model error

Superscripts

f	Forecast step
j	Ensemble member
u	Update step
ℓ	Optimization iteration

REFERENCES

Aanonsen, S.I., Naevdal, G., Oliver, D.S. et al. 2009. The Ensemble Kalman Filter in Reservoir Engineering—a Review. *SPE Journal* **14** (3): pp. 393–412. DOI: 10.2118/117274-pa.

Alarfaj, M. K. and McVay, D. A. 2016. Improved Framework for Measuring the Magnitude and Impact of Biases in Project Evaluation. Paper presented at the SPE Annual Technical Conference and Exhibition, Dubai, UAE. Society of Petroleum Engineers 181430. DOI:10.2118/181430-ms.

Almohammadi, H.H.S. 2013. Continuous Model Updating and Forecasting for a Naturally Fractured Reservoir, Texas A&M University.

Backus, G.E. and Gilbert, J.F. 1967. Numerical Applications of a Formalism for Geophysical Inverse Problems. *Geophysical Journal of the Royal Astronomical Society* **13** (1–3): 247–276. DOI: 10.1111/j.1365-246X.1967.tb02159.x.

Bissell, R. 1994. Calculating Optimal Parameters for History Matching. Paper presented at the ECMOR IV - 4th European Conference on the Mathematcs of Oil Recovery, Roros, Norway.

Brashear, J.P., Becker, A.B., and Faulder, D.D. 2001. Where Have All the Profits Gone? *Journal of Petroleum Technology* **53** (6): 20–23, 70–73. DOI: 10.2118/73141-ms.

Brouwer, D.R., Naevdal, G., Jansen, J.D. et al. 2004. Improved Reservoir Management through Optimal Control and Continuous Model Updating. Paper presented at the SPE Annual Technical Conference and Exhibition, Houston, Texas. Society of Petroleum Engineers 90149. DOI: 10.2118/90149-ms.

Capen, E.C. 1976. The Difficulty of Assessing Uncertainty (Includes Associated Papers 6422 and 6423 and 6424 and 6425). *Journal of Petroleum Technology* **28** (8): 843–850. DOI: 10.2118/5579-pa.

Chen, C., Li, G., and Reynolds, A.C. 2011. Robust Constrained Optimization of Short and Long-Term Npv for Closed-Loop Reservoir Management. Paper presented at the SPE Reservoir Simulation Symposium, The Woodlands, Texas, USA. Society of Petroleum Engineers 141314. DOI: 10.2118/141314-ms.

Chen, Y., Oliver, D.S., and Zhang, D. 2009. Efficient Ensemble-Based Closed-Loop Production Optimization. *SPE Journal* **14** (4): pp. 634–645. DOI: 10.2118/112873-pa.

Chib, S. and Greenberg, E. 1995. Understanding the Metropolis-Hastings Algorithm. *The American Statistician* **49** (4): 327–335.

Eclipse Indusrty Reference Reservoir Simulator. 2014. Schlumberger, https://www.software.slb.com/products/eclipse/eclipse-2014

Efendiev, Y., Datta-Gupta, A., Ginting, V. et al. 2005. An Efficient Two-Stage Markov Chain Monte Carlo Method for Dynamic Data Integration. *Water Resources Research* **41** (12). DOI: 10.1029/2004WR003764.

Elrafie, E.A., White, J.P., Al-Awami, F.H. et al. 2007. The Event Solution—a New Approach for Fully Integrated Studies Covering Uncertainty Analysis and Risk Assessment. Paper presented at the SPE Middle East Oil and Gas Show and Conference, Kingdom of Bahrain. Society of Petroleum Engineers SPE-105276-MS. DOI: 10.2118/105276-ms.

Emerick, A. and Reynolds, A. 2010. Enkf-Mcmc. In *SPE EUROPEC/EAGE Annual Conference and Exhibition*.

Emerick, A.A. and Reynolds, A.C. 2011. Combining the Ensemble Kalman Filter with Markov Chain Monte Carlo for Improved History Matching and Uncertainty Characterization. Paper presented at the SPE Reservoir Simulation Symposium, The Woodlands, Texas, USA. Society of Petroleum Engineers SPE-141336-MS. DOI: 10.2118/141336-ms.

Evensen, G. 1994. Sequential Data Assimilation with a Nonlinear Quasi-Geostrophic Model Using Monte Carlo Methods to Forecast Error Statistics. *Journal of Geophysical Research: Oceans* **99** (C5): 10143–10162.

Evensen, G. 2009. *Data Assimilation: The Ensemble Kalman Filter*. Berlin: Springer Verlag. Original edition. ISBN 978-3-642-03710-8.

Floris, F.J.T., Bush, M.D., Cuypers, M. et al. 2001. Methods for Quantifying the Uncertainty of Production Forecasts: A Comparative Study. *Petroleum Geoscience* **7**: S87–S96.

Foss, B.A. and Jensen, J.P. 2011. Performance Analysis for Closed-Loop Reservoir Management. *SPE Journal* **16** (1): pp. 183–190. DOI: 10.2118/138891-pa.

Gelman, A., Carlin, J.B., Stern, H.S. et al. 2013. *Bayesian Data Analysis, Third Edition*: Taylor & Francis. Original edition. ISBN 9781439840955.

Gelman, A. and Rubin, D.B. 1992. Inference from Iterative Simulation Using Multiple Sequences. *Statistical Science* **7** (4): 457–511.

Geweke, J. 1992. Evaluating the Accuracy of Sampling-Based Approaches to the Calculation of Posterior Moments. In *Bayesian Statistics 4*, eds. Bernardo, J.M., Berger, J.O., Dawid, A.P. et al.: Oxford University Press.

Geyer, C.J. 1992. Practical Markov Chain Monte Carlo. *Statistical Science* **7** (4): 473–483.

Gringarten, A.C. 1998. Evolution of Reservoir Management Techniques: From Independent Methods to an Integrated Methodology. Impact on Petroleum Engineering Curriculum, Graduate Teaching and Competitive Advantage of Oil Companies. Paper presented at the SPE Asia Pacific Conference on Integrated Modelling for Asset Management, Kuala Lumpur, Malaysia. Society of Petroleum Engineers 00039713. DOI: 10.2118/39713-ms.

Gu, Y. and Oliver, D.S. 2005. The Ensemble Kalman Filter for Continuous Updating of Reservoir Simulation Models. *Journal of Energy Resources Technology* **128** (1): 79–87. DOI: 10.1115/1.2134735.

Gu, Y. and Oliver, D.S. 2007. An Iterative Ensemble Kalman Filter for Multiphase Fluid Flow Data Assimilation. DOI: 10.2118/108438-PA.

Haario, H., Saksman, E., and Tamminen, J. 1999. Adaptive Proposal Distribution for Random Walk Metropolis Algorithm. *Computational Statistics* **14** (3): 375–395. DOI: 10.1007/s001800050022.

Haario, H., Saksman, E., and Tamminen, J. 2001. An Adaptive Metropolis Algorithm. *Bernoulli* **7** (2): 223–242.

Halbouty, M.T. 1977. Synergy Is Essential to Maximum Recovery Michel T. Calls for Full Coordination of Petroleum Engineers and Explorationists. *Journal of Petroleum Technology* **29** (7): 750–754. DOI: 10.2118/6990-pa.

Hastings, W.K. 1970. Monte Carlo Sampling Methods Using Markov Chains and Their Applications. *Biometrika* **57** (1): 97–109. DOI: 10.2307/2334940.

Holden, L. 1998. *Adaptive Chains*. Norwegian Computing Center.

Holmes, J., McVay, D.A., and Senel, O. 2007. A System for Continuous Reservoir Simulation Model Updating and Forecasting. Paper presented at the Digital Energy Conference and Exhibition, Houston, Texas, U.S.A. Society of Petroleum Engineers SPE-107566-MS. DOI: 10.2118/107566-ms.

Hu, L.Y. 2000. Gradual Deformation and Iterative Calibration of Gaussian-Related Stochastic Models. *Mathematical Geology* **32** (1): 87–108. DOI: 10.1023/a:1007506918588.

Jackman, S. 2009a. Markov Chain Monte Carlo. In *Bayesian Analysis for the Social Sciences*: John Wiley & Sons, Ltd.

Jackman, S. 2009b. Markov Chains. In *Bayesian Analysis for the Social Sciences*: John Wiley & Sons, Ltd.

Jafarpour, B. and McLaughlin, D.B. 2009a. Estimating Channelized-Reservoir Permeabilities with the Ensemble Kalman Filter: The Importance of Ensemble Design. DOI: 10.2118/108941-PA.

Jafarpour, B. and McLaughlin, D.B. 2009b. Reservoir Characterization with the Discrete Cosine Transform. DOI: 10.2118/106453-PA.

Jain, A.K. 1989. *Fundamentals of Digital Image Processing*: Prentice Hall. Original edition. ISBN 9780133361650.

Jansen, J.-D., Bosgra, O.H., and Van den Hof, P.M.J. 2008. Model-Based Control of Multiphase Flow in Subsurface Oil Reservoirs *Journal of Process Control* **18** (9): 846–855.

Jansen, J.D., Douma, S.D., Brouwer, D.R. et al. 2009. Closed Loop Reservoir Management. Paper presented at the SPE Reservoir Simulation Symposium, The Woodlands, Texas.

Kalman, R.E. 1960. A New Approach to Linear Filtering and Prediction Problems. *Journal of Basic Engineering* **82** (1): 35–45. DOI: 10.1115/1.3662552.

Li, G. and Reynolds, A.C. 2007. An Iterative Ensemble Kalman Filter for Data Assimilation. Society of Petroleum Engineers. DOI: 10.2118/109808-MS.

Liu, N. and Oliver, D.S. 2003. Evaluation of Monte Carlo Methods for Assessing Uncertainty. *SPE Journal* **8** (2): 188–195. DOI: 10.2118/84936-pa.

Lorentzen, R.J. and Naevdal, G. 2011. An Iterative Ensemble Kalman Filter. *IEEE Transactions on Automatic Control* **56** (8): 1990–1995.

Lorentzen, R.J., Shafieirad, A., and Naevdal, G. 2009. Closed Loop Reservoir Management Using the Ensemble Kalman Filter and Sequential Quadratic Programming. Paper presented at the SPE Reservoir Simulation Symposium, The

Woodlands, Texas. Society of Petroleum Engineers SPE-119101-MS. DOI: 10.2118/119101-ms.

Ma, X., Al-Harbi, M., Datta-Gupta, A. et al. 2008. An Efficient Two-Stage Sampling Method for Uncertainty Quantification in History Matching Geological Models. *SPE Journal* **13** (1): pp. 77–87. DOI: 10.2118/102476-pa.

McVay, D.A. and Dossary, M. 2012. The Value of Assessing Uncertainty. Paper presented at the SPE Annual Technical Conference and Exhibition, San Antonio, Texas, USA. Society of Petroleum Engineers SPE-160189-MS. DOI: 10.2118/160189-ms.

McVay, D.A., Lee, W.J., and Alvarado, M.G. 2005. Calibration Improves Uncertainty Quantification in Production Forecasting. *Petroleum Geoscience* **11** (3): 195–202.

Metropolis, N., Rosenbluth, A.W., Rosenbluth, M.N. et al. 1953. Equation of State Calculations by Fast Computing Machines. *The journal of chemical physics* **21** (6): 1087–1092.

Naevdal, G., Johnsen, L.M., Aanonsen, S.I. et al. 2005. Reservoir Monitoring and Continuous Model Updating Using Ensemble Kalman Filter. *SPE Journal* **10** (1): pp. 66–74. DOI: 10.2118/84372-pa.

Naevdal, G., Mannseth, T., and Vefring, E.H. 2002. Near-Well Reservoir Monitoring through Ensemble Kalman Filter. Paper presented at the SPE/DOE Improved Oil Recovery Symposium, Tulsa, Oklahoma. Copyright 2002, Society of Petroleum Engineers Inc. 00075235. DOI: 10.2118/75235-ms.

Oliver, D.S., Chuna, L.B., and Reynolds, A.C. 1997. Markov Chain Monte Carlo Methods for Conditioning a Permeability Field to Pressure Data. *Mathmatical Geology* **29** (1): 61–91.

Oliver, D.S., He, N., and Reynolds, A.C. 1996. Conditioning Permeability Fields to Pressure Data. In *ECMOR V-5th European Conference on the Mathematics of Oil Recovery*. ISBN 2214-4609.

Oliver, D.S., Reynolds, A.C., and Liu, N. 2008. *Inverse Theory for Petroleum Reservoir Characterization and History Matching*: Cambridge University Press. Original edition. ISBN 9781139472616.

Peaceman, D.W. 1978. Interpretation of Well-Block Pressures in Numerical Reservoir Simulation (Includes Associated Paper 6988). *Society of Petroleum Engineers Journal* **18** (3): 183–194. DOI: 10.2118/6893-pa.

Raftery, A.E. and Lewis, S. 1992. How Many Iterations in the Gibbs Sampler? In *Bayesian Statistics*, eds. Bernardo, J.M., Berger, J.O., Dawid, A.P. et al.: Oxford University Press.

Reynolds, A., Zafari, M., and Li, G. 2006. Iterative Forms of the Ensemble Kalman Filter. In *10th European Conference on the Mathmatics of Oil Recovery*. Amsterdam.

Saputelli, L., Nikolaou, M., and Economides, M.J. 2005. Self-Learning Reservoir Management. *SPE Reservoir Evaluation & Engineering* **8** (6): pp. 534–547. DOI: 10.2118/84064-pa.

Sarma, P., Durlofsky, L.J., and Aziz, K. 2005. Efficient Closed-Loop Production Optimization under Uncertainty. Paper presented at the SPE Europec/EAGE Annual Conference, Madrid, Spain. Society of Petroleum Engineers SPE-94241-MS. DOI: 10.2118/94241-ms.

Strebelle, S. 2002. Conditional Simulation of Complex Geological Structures Using Multiple-Point Statistics. *Mathematical Geology* **34** (1): 1–21.

Strebelle, S.B. and Journel, A.G. 2001. Reservoir Modeling Using Multiple-Point Statistics. Society of Petroleum Engineers. DOI: 10.2118/71324-MS.

Walsh, B. 2004. Markov Chain Monte Carlo and Gibbs Sampling.

Wang, C., Li, G., and Reynolds, A.C. 2009. Production Optimization in Closed-Loop Reservoir Management. *SPE Journal* **14** (3): pp. 506–523. DOI: 10.2118/109805-pa.

APPENDIX A

A.1 Metropolis-Hasting Transition Kernel Satisfying Reversibility Condition

The M-H acceptance probability is defined by **Eq. 62.**

$$\alpha(x,y) = \min\left(1, \frac{p(y)q(y,x)}{p(x)q(x,y)}\right) \tag{62}$$

There are three cases to consider, **Eqs. 63–65.**

$$q(x,y)p(x) = q(y,x)p(y) \tag{63}$$

$$q(x,y)p(x) > q(y,x)p(y) \tag{64}$$

$$q(x,y)p(x) < q(y,x)p(y) \tag{65}$$

If the equality in Eq. 63 holds, then:

$$\alpha(x,y) = \alpha(y,x) = 1 \tag{66}$$

$$P(x,y)p(x) = q(x,y)\alpha(x,y)p(x) \tag{67}$$

$$P(y,x)p(y) = q(y,x)\alpha(y,x)p(y) \tag{68}$$

$$P(x,y)p(x) = P(y,x)p(y) \tag{69}$$

If the inequality in Eq. 64 holds, then:

$$q(x,y)p(x) \ > q(y,x)p(y) \tag{70}$$

$$\alpha(x,y) = \frac{p(y)q(y,x)}{p(x)q(x,y)} \tag{71}$$

$$\alpha(y,x) = 1 \tag{72}$$

$$P(x,y)p(x) = q(x,y)\frac{p(y)q(y,x)}{p(x)q(x,y)}p(x) = q(y,x)p(y) \tag{73}$$

$$P(y,x)p(y) = q(y,x)p(y) \tag{74}$$

$$P(x,y)p(x) = P(y,x)p(y) \tag{75}$$

If the inequality in Eq. 65 holds, then:

$$q(x,y)p(x) < q(y,x)p(y) \tag{76}$$

$$\alpha(x,y) = 1 \tag{77}$$

$$\alpha(y,x) = \frac{p(x)q(x,y)}{p(y)q(y,x)} \tag{78}$$

$$P(x,y)p(x) = q(x,y)p(x) \tag{79}$$

$$P(y,x)p(y) = q(y,x)\frac{p(x)q(x,y)}{p(y)q(y,x)}\ p(y) = p(x)q(x,y) \tag{80}$$

$$P(x,y)p(x) = P(y,x)p(y) \tag{81}$$

Eqs. 69, 75, and 81 prove that for all cases, the M-H acceptance ratio satisfies the reversibility condition.

A.2 Derivation for Two-Stage Metropolis-Hasting Acceptance Ratio

$$Q(y,x) = \alpha(y,x)q(y,x) \tag{82}$$

$$Q(y,x) = \min\left(1, \frac{\pi^*(x)q(x,y)}{\pi^*(y)q(y,x)}\right) q(y,x) \tag{83}$$

$$Q(y,x) = \min\left(q(y,x), \frac{\pi^*(x)q(x,y)}{\pi^*(y)}\right) \tag{84}$$

$$Q(y,x) = \frac{1}{\pi^*(y)}\min\left(\pi^*(y)q(y,x), \pi^*(x)q(x,y)\right) \tag{85}$$

$$Q(y,x) = \frac{\pi^*(x)q(x,y)}{\pi^*(y)}\min\left(\frac{\pi^*(y)q(y,x)}{\pi^*(x)q(x,y)},\ 1\right) \tag{86}$$

$$Q(y,x) = \frac{\pi^*(x)}{\pi^*(y)}q(x,y)\alpha(x,y) = \frac{\pi^*(x)}{\pi^*(y)}Q(x,y) \tag{87}$$

$$Q(y,x) = \frac{\pi^*(x)}{\pi^*(y)}Q(x,y) \tag{88}$$

$$\frac{Q(y,x)}{Q(x,y)} = \frac{\pi^*(x)}{\pi^*(y)} \tag{89}$$

$$\rho(x,y) = \min\left(1, \frac{\pi(y)\pi^*(x)}{\pi(x)\pi^*(y)}\right) \tag{90}$$